

# Tailoring the Electronic Properties of Epitaxial Oxide Films via Strain for SAW and Neuromorphic Applications

Yang Dai

Schlüsseltechnologien / Key Technologies

Band / Volume 169

ISBN 978-3-95806-319-8





Forschungszentrum Jülich GmbH  
Institute of Complex Systems  
Bioelectronics (ICS-8)

# **Tailoring the Electronic Properties of Epitaxial Oxide Films via Strain for SAW and Neuromorphic Applications**

Yang Dai

Schriften des Forschungszentrums Jülich  
Reihe Schlüsseltechnologien / Key Technologies

Band / Volume 169

---

ISSN 1866-1807

ISBN 978-3-95806-319-8

Bibliografische Information der Deutschen Nationalbibliothek.  
Die Deutsche Nationalbibliothek verzeichnet diese Publikation in der  
Deutschen Nationalbibliografie; detaillierte Bibliografische Daten  
sind im Internet über <http://dnb.d-nb.de> abrufbar.

Herausgeber und Vertrieb: Forschungszentrum Jülich GmbH  
Zentralbibliothek, Verlag  
52425 Jülich  
Tel.: +49 2461 61-5368  
Fax: +49 2461 61-6103  
[zb-publikation@fz-juelich.de](mailto:zb-publikation@fz-juelich.de)  
[www.fz-juelich.de/zb](http://www.fz-juelich.de/zb)

Umschlaggestaltung: Grafische Medien, Forschungszentrum Jülich GmbH

Druck: Grafische Medien, Forschungszentrum Jülich GmbH

Copyright: Forschungszentrum Jülich 2018

Schriften des Forschungszentrums Jülich  
Reihe Schlüsseltechnologien / Key Technologies, Band / Volume 169

D 38 (Diss., Köln, Univ., 2017)

ISSN 1866-1807  
ISBN 978-3-95806-319-8

Vollständig frei verfügbar über das Publikationsportal des Forschungszentrums Jülich (JuSER)  
unter [www.fz-juelich.de/zb/openaccess](http://www.fz-juelich.de/zb/openaccess).



This is an Open Access publication distributed under the terms of the [Creative Commons Attribution License 4.0](https://creativecommons.org/licenses/by/4.0/), which permits unrestricted use, distribution, and reproduction in any medium, provided the original work is properly cited.

## Zusammenfassung

In dieser Arbeit wird der Einfluss von biaxialer Verspannung auf die elektronischen Eigenschaften epitaktisch gewachsener Oxydschichten am Beispiel von zwei Perowskitsystemen,  $(\text{Ba}_x\text{Sr}_{1-x})\text{TiO}_3$  und  $(\text{K}_x\text{Na}_{1-x})\text{NbO}_3$ , analysiert und diskutiert. Wir zeigen, dass die Phasenübergangstemperatur der oxydischen Schichten mittels der oberflächenorientierten biaxialen Spannung eingestellt werden kann. Kompressive Verspannung führt hierbei zu einer Reduktion der Übergangstemperatur, während Zugspannung zu einer Erhöhung der Übergangstemperatur führt. Mit der Veränderung der Übergangstemperaturen lassen sich dann die elektronischen Eigenschaften (u.a. Dielektrizität, Piezoelektrizität und sogar Leitfähigkeit) der Schichten gezielt modifizieren. Mögliche Anwendungen dieses ‚Engineering‘ der elektronischen Schichteigenschaften werden in der Arbeit demonstriert.

Verspannungen von bis zu  $\pm 1.7\%$  werden in den Perowskitschichten mit Hilfe der Gitterfehl-anpassung zwischen dem Film und dem Substrat generiert.  $(\text{Ba}_x\text{Sr}_{1-x})\text{TiO}_3$  ( $x = 0, 0.125, 0.37, 1$ ) und  $\text{K}_{0.7}\text{Na}_{0.3}\text{NbO}_3$  Schichten mit einer Dicke von 5 nm bis 200 nm werden hierzu auf unterschiedlichen Scandaten ((110) orientiertes  $\text{DyScO}_3$ ,  $\text{TbScO}_3$ ,  $\text{GdScO}_3$ , and  $\text{SmScO}_3$ ) mittels Laserdeposition bzw. metallorganischer chemischer Dampfphasendeposition epitaktisch abgeschieden. Für die Charakterisierung werden metallische Elektroden (Pt oder Ti/Pt) auf der Schichte mittels Elektrodenstrahlithographie und Lift-off-Technologie angebracht. Die strukturellen Eigenschaften der verspannten Schichten werden dann eingehend mittels Röntgen-diffraktometrie, Rutherford-Rückstreuung, time-of-flight Sekundärionenmassenspektroskopie und Rasterelektronenmikroskopie analysiert. Kryoelektronische Messungen im Temperaturbereich von 5 bis 500K zeigen dann die elektronischen Eigenschaften der Schichten.

Die Hauptresultate dieser Arbeit sind:

- (i) Sowohl kompressive Spannung als auch Zugspannung führt zu einer spannungs- und materialabhängigen Verschiebung der Übergangstemperatur von bis zu einigen 100 K. So bewirken z.B. 1.2 % Zugspannung eine Erhöhung der Übergangstemperatur von  $\sim 300$  K in  $\text{SrTiO}_3$ , während schon -0.6 % kompressive Spannung eine Reduktion der Übergangstemperatur von  $\sim 300$  K in  $\text{K}_{0.7}\text{Na}_{0.3}\text{NbO}_3$  bewirken.
- (ii) Die dielektrische Konstante kann durch die Modifizierung der Übergangstemperature gezielt verändert werden. So kann sie z.B. für  $\text{SrTiO}_3$  bei Raumtemperatur von ca. 300 (unverspanntes  $\text{SrTiO}_3$ ) auf ca. 8000 erhöht werden, indem die Übergangstemperatur auf Raumtemperatur angehoben wird.
- (iii) Die piezoelektrischen Eigenschaften der Oxydschichten lassen sich ebenfalls mittels Verspannung verändern. Dies zeigt sich z.B. an Oberflächenwellen, die in verspannten extrem dünnen (z.B. 27 nm)  $\text{K}_{0.7}\text{Na}_{0.3}\text{NbO}_3$  Filmen beobachtet werden. Die Signalstärke der Oberflächenwellen korreliert ebenfalls mit der Übergangstemperatur und kann potentiell für extrem empfindliche Sensorsysteme verwandt werden.

- (iv) Schließlich wird auch die Leitfähigkeit von verspannten SrTiO<sub>3</sub> Schichten durch die Erhöhung der Mobilität der Elektronen und auch Sauerstofffehlstellen stark erhöht. Unter Verwendung geeigneter Elektrodendesigns, die das elektrische Feld und dadurch die Temperaturverteilung in der Oxydschicht beeinflussen, kann hiermit ein Memristorverhalten und sogar eine Plastizität des Widerstandsverhaltens eingestellt werden. Beides kann z.B. für Anwendungen von der Simulation biologischer Synapsen bis hin zu neuromorphem 'Engineering' eingesetzt werden.

## Abstract

In this work the impact of biaxial strain on the electronic properties of epitaxial grown oxide thin films is analyzed and discussed using two perovskite systems,  $(\text{Ba}_x\text{Sr}_{1-x})\text{TiO}_3$  and  $(\text{K}_x\text{Na}_{1-x})\text{NbO}_3$ . We show that the phase transition temperature of the oxide films can be tuned via in-plane biaxial strain. Compressive strain leads to a reduction of the transition temperature, tensile strain increases the transition temperature. As a result, the electronic properties (i.e. dielectric constant, piezoelectric effect, and even conductivity) are modified. Possible applications of this “engineering” of the electronic properties of oxide films are demonstrated.

Strain of  $\pm 1.7\%$  in perovskites thin films is generated by the mismatch of the lattice parameters of film and substrate.  $(\text{Ba}_x\text{Sr}_{1-x})\text{TiO}_3$  ( $x = 0, 0.125, 0.37, 1$ ) and  $\text{K}_{0.7}\text{Na}_{0.3}\text{NbO}_3$  films with a thickness ranging between 5 nm and 200 nm are deposited on various scandites ((110) oriented  $\text{DyScO}_3$ ,  $\text{TbScO}_3$ ,  $\text{GdScO}_3$ , and  $\text{SmScO}_3$ ) using either pulse laser deposition or metal-organic chemical vapor deposition. For the characterization metallic electrodes (Pt or Ti/Pt) are prepared on the oxide film using e-beam lithography and lift-off technology. The structural properties of the biaxial strained thin films are carefully examined via X-ray diffraction, Rutherford backscattering spectrometry, time-of-flight secondary ion mass spectroscopy, and scanning electron microscopy. Cryoelectronic measurements are used to analyze the electronic properties in a temperature range of 5 K to 500 K.

The major results are:

- (i) In oxide ferroelectric thin films, both compressive and tensile biaxial strain result in a material and strain dependent shift of the phase transition temperature of up to several 100 K. For instance, 1.2 % tensile strain shifts the transition temperature by  $\sim 300$  K in  $\text{SrTiO}_3$  while -0.6 % compressive stress leads to a reduction of the phase transition temperature by  $\sim 300$  K in  $\text{K}_{0.7}\text{Na}_{0.3}\text{NbO}_3$ .
- (ii) The dielectric constant can be modified at a desired temperature (typically room temperature) via the shift of the phase transition towards this temperature. For instance in case of  $\text{SrTiO}_3$  the permittivity is enhanced from  $\sim 300$  (unstrained bulk  $\text{SrTiO}_3$ ) to  $\sim 8000$  by moving the phase transition temperature to room temperature.
- (iii) The piezoelectric properties of the oxide films are also tailored via strain. As a result surface acoustic waves can be generated in strained thin (e.g. 27 nm)  $\text{K}_{0.7}\text{Na}_{0.3}\text{NbO}_3$  films. The strength of the surface acoustic wave signal correlates to the phase transition of the films and might be used for extremely sensitive sensor systems.
- (iv) Finally, the conductivity of strained  $\text{SrTiO}_3$  films is enhanced due to the increased mobility of electrons and oxygen vacancies. Using an adequate electrode design which affects the electric field and thus temperature distribution in the film, memristor behavior and even a plasticity of the resistive behavior can be obtained. The latter can

be used for applications ranging from the simulation of a biological synapsis to neuro-morphic engineering.

# Contents

1. Introduction.....	1
2. Theoretical background .....	4
2.1 Perovskites .....	4
2.1.1 (Ba <sub>x</sub> Sr <sub>1-x</sub> )TiO <sub>3</sub> .....	4
2.1.2 (K <sub>x</sub> Na <sub>1-x</sub> )NbO <sub>3</sub> .....	6
2.2 Ferroelectricity .....	8
2.3 Ferroelectric phase transition .....	10
2.3.1 Curie-Weiss law.....	11
2.3.2 Landau theory .....	11
2.4 Engineering the phase transition .....	13
2.4.1 Doping.....	13
2.4.2 Strain.....	15
2.5 Piezoelectricity.....	17
2.6 Conductivity.....	19
2.6.1 Oxygen vacancy in SrTiO <sub>3</sub> .....	19
2.6.2 Resistance switching behavior.....	20
3. Sample preparation and experimental techniques.....	24
3.1 Thin film deposition.....	24
3.1.1 Pulsed laser deposition.....	24
3.1.2 Metal-organic chemical vapor deposition.....	26
3.2 Film characterization.....	26
3.2.1 X-ray diffraction .....	27
3.2.2 Rutherford backscattering spectrometry .....	33
3.2.3 Time-of-flight secondary ion mass spectroscopy .....	35
3.2.4 Scanning electron microscopes.....	36
3.2.5 Atomic force microscopy.....	38
3.3 Device preparation and characterization .....	39
3.3.1 Electrodes fabrication .....	40
3.3.2 Temperature control.....	42

3.3.3 Permittivity measurement .....	48
3.3.4 Polarization measurement .....	54
3.3.5 SAW measurement .....	57
3.3.6 Conductivity measurement .....	62
4. Engineering the dielectric properties of (Ba,Sr)TiO <sub>3</sub> via tensile strain .....	65
4.1 Structure characterization .....	67
4.2 Dielectric properties .....	70
4.2.1 Strain induced phase transition .....	70
4.2.2 Critical thickness and anisotropic strain .....	77
4.3 Summary .....	79
5. Engineering piezoelectric properties of (K,Na)NbO <sub>3</sub> via compressive strain .....	81
5.1 Structural characterization and phase transition .....	82
5.2 SAW devices .....	86
5.3 Summary .....	94
6. Engineering the electric transport properties of SrTiO <sub>3</sub> via tensile strain .....	95
6.1 Strain oxides for neuromorphic engineering .....	96
6.2 From memristor to neuromorphic devices .....	99
6.2.1 Schottky contact versus ohmic contact .....	99
6.2.2 Memristive behavior .....	101
6.2.3 Neuromorphic behavior .....	103
6.2.4 Mechanism of resistive switching and plasticity .....	106
6.3 Summary .....	111
7. Conclusions .....	113
Reference .....	115
Appendices .....	122
Acknowledgements .....	129

# 1. Introduction

The development of modern electronic devices has revolutionized our quality and way of life over the past decades. One of the most basic but nevertheless most important devices in the information technology is the field-effect transistor. Shockley, Bardeen, and Brattain demonstrated the transistor in 1947 and later in 1956 they shared the Nobel Prize in Physics. At that time, a typical size of the transistor was several cm. Thanks to the development of the thin film technologies (e.g. deposition and lithography) the size of the electronic device has been reduced and its performance has been improved quit a lot. For instance, nowadays they work faster (from 100 kHz in the first electronic general purpose computer ENIAC to several GHz of the modern computer), the size becomes smaller (a single transistor is reduced to few nm size[1] nowadays), and integration into complex electronics is possible. Nevertheless, for further improvement of the devices, the improvement (engineering) of the different components of the device is necessary.

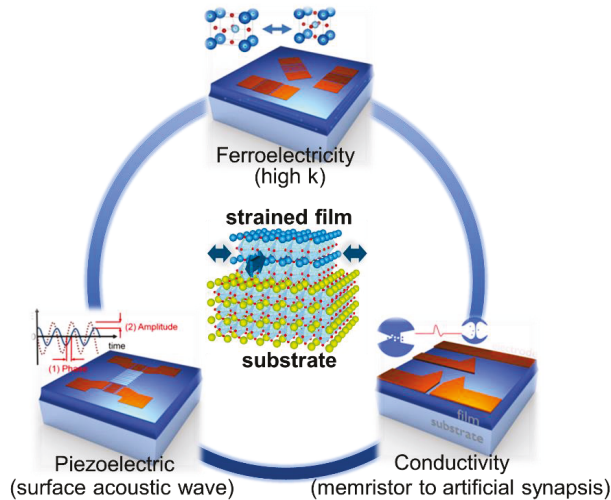


Figure 1-1: Sketch of the intention of this work. Thin oxide films ( $ABO_3$  perovskite structure) grow epitaxially and are biaxial strained on lattice-mismatched substrates ( $ABO_3$  perovskite structure with a different lattice constant compared to the film). As a result of the strain varies properties of the film, ranging from the ferroelectric, piezoelectric to conductive properties are changed (engineered). This engineering of the film properties is studied in this work.

Metal oxides represent one widely used family of materials to product advanced electronic devices. In order to further miniaturization of microelectronic components, metal oxides with high dielectric constant (high k) are necessary for instance for the gate dielectric or another dielectric

layers of electronic devices.[2] For instance,  $\text{HfO}_2$  with a dielectric constant of 25[3] is used as a gate dielectric in modern transistors. Nevertheless, there are other candidates with even higher dielectric constant. For example,  $\text{TiO}_2$  provides the dielectric constant of approx. 80,[4] and  $\text{SrTiO}_3$  has a dielectric constant of approximately 300 at room temperature.[5] However, besides looking for alternative materials, there are also other ways to improve the performance of existing material. For example  $\text{SrTiO}_3$  has a much higher dielectric constant of  $\sim 25000$  at its transition temperature. Unfortunately this transition temperature is close to 0 K.[6] Since the phase transition is generally strongly related to the structural properties of the material, it would be interesting to modify the material's structure to engineer its electronic properties. This is the major purpose of this work (see Figure 1-1).

The growth of strained oxide layers has evolved from predominantly curiosity driven basic research to a major technology in the field of semiconductor devices.[7, 8] The coupling between strain and polarization is pronounced especially in ferroelectric materials. In particular, thin film ternary (e.g. titanate or niobate) oxide ferroelectrics show profound features, e.g. giant permittivity, large piezoelectricity, or tunability, in the range of the phase transition temperature from the ferroelectric to the dielectric state. It has been long demonstrated that for single crystals the piezoelectric and dielectric properties can be strongly modified by the application of hydrostatic pressure.[9, 10] However, one of the great disadvantages lies in the restriction of the pressure (e.g. technically only small pressure can be applied and cracks appear typically already at a strain level of  $\sim 0.2\%$  [11] for bulk ceramics. Thanks to the development of the thin film technology, the application of ferroelectric is not restricted to bulk ceramics. For thin films, due to the clamping of the film to a substrate (see Figure 1-1) large strain can be applied and cracking occurs at much larger strain levels. Nowadays more and more ferroelectric films can be produced with a good quality by various preparation techniques. The strain has been used to enhance the charge mobility of semiconductors in thin film transistors.[12] The transition temperature to ferromagnetism [13] and superconductivity [14] may also be altered due to the strain in the film. In the case of ferroelectric materials, the onset of polarization is accompanied by a spontaneous strain of the material. Consequently, an applied strain can affect the ferroelectric properties, e.g. the stability of the ferroelectric phase, the transition temperature, and the electronic and electromechanical properties. In accordance with thermodynamic prediction [15] the ferroelectric transition temperature can be shifted by hundreds of degrees in strained ferroelectrics.

For heteroepitaxially grown thin films, mechanical stress is naturally induced by the underlying substrate. The stress is caused by the lattice mismatch and the difference in thermal expansion coefficients between substrate and film. Even more interesting thing is the combination of substrates and films with different crystallographic symmetries. In this case, the structural mismatch will be different in different crystallographic directions. As a result, not only the

structural but also the electromechanical properties of the layer might be different in different crystallographic directions.

Emboldened by the success of theory and experiment, the strain may tune other properties more than

- (i) the transition temperature and, thus, dielectric properties of ferroelectrics.
- (ii) For instance, all ferroelectrics are piezoelectrics. In piezoelectric material, the coupling between mechanical and electrical energy results in an electric polarization when stress is applied. The piezoelectric effect is largest close to the phase transition.[16] Thus it is of interest to analyze the impact of strain on the piezoelectric properties.
- (iii) Strain might also affect the electric conductivity of materials. This provides an option to improve the performance of memristive devices.

In this thesis, we try to tackle and discuss all these questions:

- (i) Many electric properties of oxide materials alter at the phase transition. Therefore, can we tailor the phase transition to the desirable temperature via strain? Do both types of strain (tensile and compressive) affect the phase transition?
- (ii) What kinds of electric properties can be affected by strain in oxide ferroelectrics and how can we characterize the impact of strain on the electric properties of these films?
- (iii) Are these altered properties applicable and do they improve the performance of electric devices?

To answer these questions, we first review the theoretical background on oxide ferroelectric materials in chapter 2. The sample preparation and characterization techniques (especially the lithography and temperature management of thin films) are introduced in chapter 3. The engineering of the phase transition, piezoelectric effects (in the form of surface acoustic wave (SAW) experiments), and electric conductance (e.g. memristive behavior) are presented in chapter 4, 5, and 6, respectively. In the end, the conclusions are summarized in chapter 7.

## 2. Theoretical background

In this chapter, first the structural properties of perovskites, including  $(\text{Ba,Sr})\text{TiO}_3$  and  $(\text{K,Na})\text{NbO}_3$ , are shown (see chapter 2.1), the polarization of ferroelectrics is discussed (see chapter 2.2), and the phase transition from ferroelectric to paraelectric in solid state is introduced in terms of the Landau theory (see chapter 2.3). Then for the engineering of the phase transition, two possible methods, doping and strain, are introduced (see chapter 2.4). The basics of the piezoelectric effect and its potential application in SAW devices are discussed in chapter 2.5 and, finally, the electron transport and ion transport (especially oxygen vacancies), in metal oxides are introduced in chapter 2.6.

### 2.1 Perovskites

In this work, the films and most of substrates are perovskites with the general chemical formula  $\text{ABO}_3$ . The A-site represents one or two types of cations and B-site is another type of cation with smaller size (see Figure 2-1). The B-site is surrounded by six oxygens, forming a  $\text{BO}_6$  octahedron. A large number of perovskite-type oxides with various properties can be obtained by substituting A and B cations. The simplest  $\text{ABO}_3$  structure is cubic, such as  $\text{SrTiO}_3$  at room temperature.

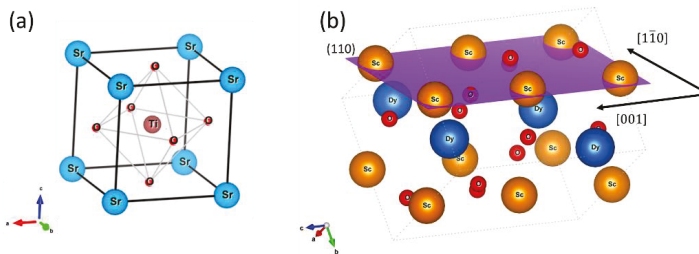


Figure 2-1: (a) Cubic unit cell of  $\text{SrTiO}_3$  belonging to the space group  $\text{Pm-3m}$ , and (b) orthorhombic unit cell structure of  $\text{DyScO}_3$ . In the case of  $\text{DyScO}_3$  which is used as a substrate in this work, the  $(110)$  plane and  $[001]$ , and  $[\bar{1}\bar{1}0]$  directions are marked, because all scandate substrates used in this work have a  $(110)$  cut. (note the size of unit cell is not to scale)

#### 2.1.1 $(\text{Ba}_x\text{Sr}_{1-x})\text{TiO}_3$

Strontium titanate ( $\text{SrTiO}_3$ ) is a promising dielectric material for device applications including capacitors and gate dielectrics. As shown in Figure 2-1, the  $\text{O}^{2-}$  is face centered in the unit cell and  $\text{Sr}^{2+}$  is located at the corners (A-site) of the unit cell. The center of the unit (B-site) is occupied by  $\text{Ti}^{4+}$ . The stoichiometric  $\text{SrTiO}_3$  is an insulator with a band gap of 3.2 eV at 0 V.[17] Normally  $\text{SrTiO}_3$  single crystals are transparent. However, in the non-stoichiometric material the color can

turn to brown. This change of the transparency is due to the free carriers that are induced by dopants and/or oxygen vacancies.[18]

The real part of the dielectric constant (permittivity) of SrTiO<sub>3</sub> ( $\epsilon = 300$  at 300 K) is higher than for most other common ceramic and polymer materials.[3] Thus it represents a potential candidate for so-called high-k applications like dielectric layers in transistors. Below room temperature its permittivity is even larger, it reaches values up to 25000 at liquid He temperature (4.2 K), see Figure 2-2. For a number of applications a high permittivity is desirable.

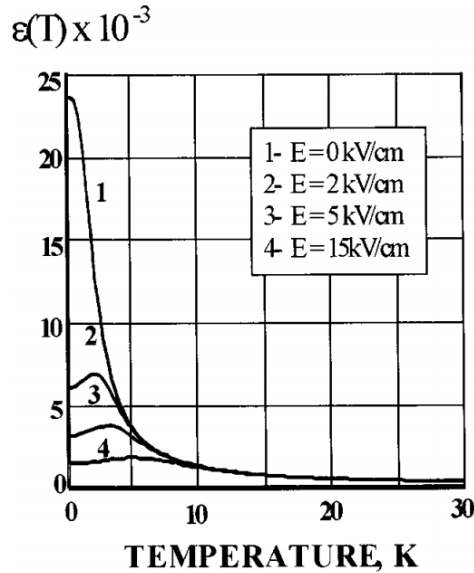


Figure 2-2: dielectric response of SrTiO<sub>3</sub> single crystal as a function of temperature from 0 K to 30 K under various d.c. electric field.[6]

An enhancement of the permittivity at a given temperature (e.g. room temperature) can be achieved via doping or by applying strain in the material. One of the major aims of this work is to engineer the dielectric properties of the perovskites via doping and strain.

By substituting Sr by Ba in Ba<sub>x</sub>Sr<sub>1-x</sub>TiO<sub>3</sub>, a structural change from cubic to tetragonal (*P4mm*) structure can be obtained at room temperature. The Curie-Weiss temperature depends on *x* in Ba<sub>x</sub>Sr<sub>1-x</sub>TiO<sub>3</sub> and can be fitted with a simple polynomial (see Figure 2-3(a)). The cubic to tetragonal ferroelectric phase transition, which is of first order in pure BaTiO<sub>3</sub>, transforms to a second-order phase transition at  $x \approx 0.2$ . [19] Later Vendik *et. al* presented the polynomial fit of this dependence. [20] In our work we used a linear and a polynomial dependence to describe the *x*-

dependence of  $T_C$ . The results are discussed in chapter 4.2 and these values show only a small deviation from the theoretical predictions.

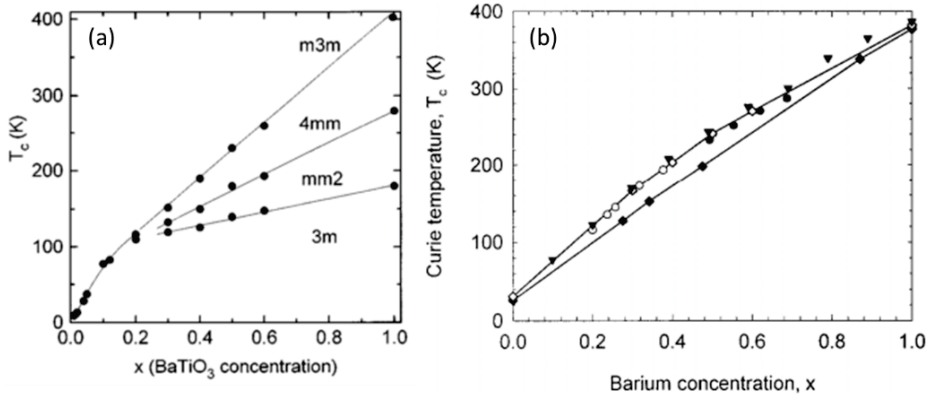


Figure 2-3: Temperature dependence of dielectric constant at frequency of 1 kHz in  $(Ba_xSr_{1-x})TiO_3$  ceramics. (adapted from (a) ref.[19], when  $x>0.2$  the transition is from high temperature cubic phase (point group  $m3m$ ) to tetragonal (point group  $4mm$ ), orthorhombic ( $mm2$ ) and trigonal phase ( $3m$ ), and (b) ref.[20])

### 2.1.2 $(K_xNa_{1-x})NbO_3$

Sodium potassium niobate ( $(K_xNa_{1-x})NbO_3$ ) represents a more complex type of  $ABO_3$  perovskite with K and/or Na as A-site and Nb as B-site. One of the interesting properties of this material is its large electromechanical coupling factor expressed by its piezoelectricity.[21] This provides the possibility to also tune the piezoelectric properties via doping and strain. The lattice parameters of  $K_xNa_{1-x}NbO_3$  single crystal are given in the Figure 2-4.

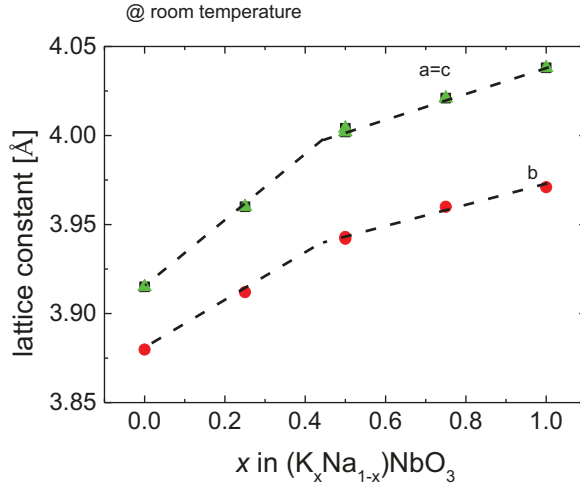


Figure 2-4: The pseudocubic lattice parameters of bulk  $K_xNa_{1-x}NbO_3$  as a function of  $x$  ( $x=0$ : ref.[22],  $x=0.25$  and  $0.75$ : ref.[23],  $x=0.5$ : ref.[24],  $x=1$ : ref.[25, 26]).

In order to estimate the lattice mismatch of film and substrate, we describe  $(K_xNa_{1-x})NbO_3$  via pseudocubic lattice parameters. In this notation, the orthorhombic unit cell with  $a \neq b \neq c$  and  $\alpha = \beta = \gamma = 90^\circ$  can be represented by a tilted pseudocubic unit cell.[27, 28] The resulting perovskite type  $ABO_3$  subcell for  $KNbO_3$  at room temperature is shown in Figure 2-5. In case of  $(K_xNa_{1-x})NbO_3$  some of the K atoms are substituted by Na atoms.

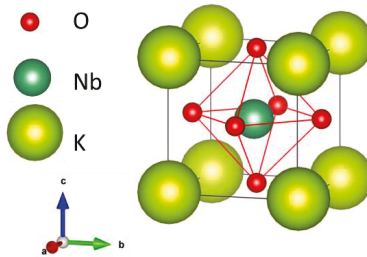


Figure 2-5: Illustration of the perovskite type  $KNbO_3$  subcell using a pseudocubic lattice.

Figure 2-6 provides the phase diagram of  $(K_xNa_{1-x})NbO_3$ . [29] For potassium concentrations  $x < 50\%$  the material shows a large number of phase transitions. Above 50% potassium, there is in principle only one important transition, which could affect the ferroelectric properties of this material, i.e. the transition from the cubic (at high temperature) to the tetragonal (at low

temperature) state. This is the reason, why we chose a concentration of 70% potassium for our samples (see chapter 5). The transition temperature from the cubic to the tetragonal state is at about 693 K (420 °C) for  $K_{0.7}Na_{0.3}NbO_3$ .

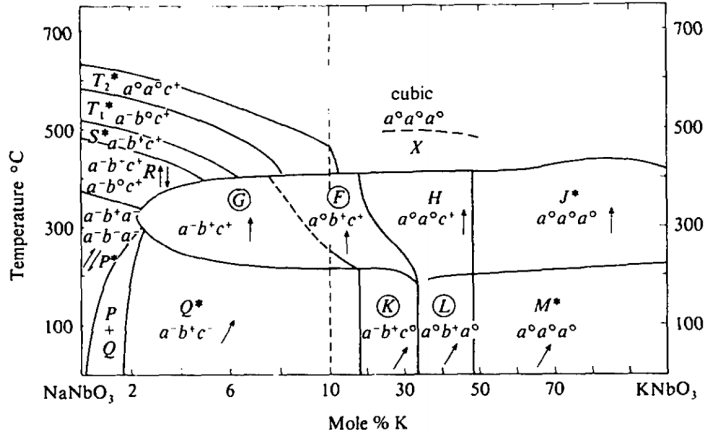


Figure 2-6: Phase diagram of  $K_xNa_{1-x}NbO_3$ . In each phase the tilt system is indicated according to the scheme of Glazer (1972)[30]. Vertical arrows indicate one-corner displacements and inclined arrows two-corner displacements of the cations. The phase X is the paraelectric state, while others, K, L, J, and F are ferroelectric states with different polarization states. (adapted from ref.[29])

Generally, any deformation of the perovskite structure results in (i) a change of lattice parameters and/or (ii) a slightly shift of the atomic positions of some or all atoms, e.g. a tilt of the  $BO_6$  octahedron. As a consequence, the B-site cation is often off-centered in order to attain a stable bonding situation. The resulting dipole is responsible for the ferroelectricity shown in most perovskites.

## 2.2 Ferroelectricity

A ferroelectric material is characterized by a spontaneous and switchable polarization, i.e. spontaneous dipoles that can be switched in an applied electric field. A dipole moment  $\mu$  is generated by two particles of charge  $q$  that are separated by a distance of  $r$ :

$$\mu = q \cdot r \quad (2-1)$$

In order to possess the spontaneous dipole moment, the centers of the positive and negative charges may not coincide in a ferroelectric. Therefore the ferroelectric cannot be centrosymmetric (e.g. cubic structure). A macroscopic polarization is typically formed by the spontaneous local dipole moments. The polarization is defined as the total dipole moment per unit volume ( $V$ ):

$$P = \frac{\sum \mu}{V} \quad (2-2)$$

Depending on the crystal structural, materials can be polarized along different possible axes. A region with an identical orientation of the polarization is called a ferroelectric domain. In a ferroelectric sample, domains with different orientations can coexist. The domain orientation can be switched from one state to another state under an external electric field.

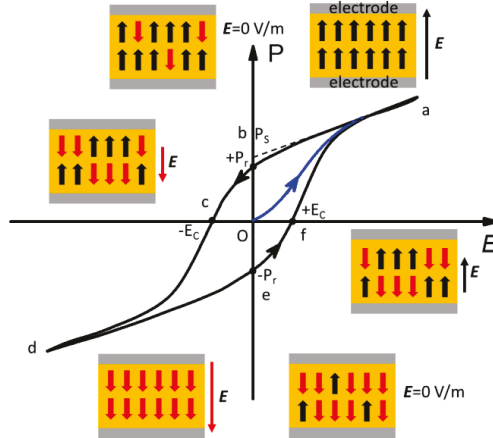


Figure 2-7: Typical  $P$ - $E$  hysteresis loop. The sketches show the macroscopic state of polarization under an external electric field.

Experimentally, the ability to switch the polarization can be observed by a measurement of the polarization as a function of the applied electric field. The result is a  $P$ - $E$  ferroelectric hysteresis loop (see Figure 2-7). Starting at the virgin state when  $P = 0$  and  $E = 0$  and increasing the external electric field, the polarization gradually increases towards a saturation state “a”, where all domains coherently orient along the electric field. The extrapolation of the polarization in this state to zero field defines the spontaneous polarization  $P_s$ . When the field is decreased to zero, the polarization decreases but does not return to zero. At  $E = 0$  it reaches the remanent polarization  $+P_r$ . When the field is reversed to the opposite direction, the macroscopic polarization switches at the so-called coercive field  $-E_c$ . A further decrease leads to a saturation of the polarization and if the field is reversed it behaves similar as described for decreasing electric fields.  $P$ - $E$  loops represent typical means to analyze the properties of ferroelectric materials.

### 2.3 Ferroelectric phase transition

One of the major parameters for the engineering of the ferroelectric properties is given by the variation of the ferroelectric phase transition, which is a structural phase transition in the ferroelectric material. This transition occurs at a certain characteristic temperature, the transition temperature. Typically above the transition temperature a higher symmetry (e.g. cubic) is observed which form is associated with the paraelectric (dielectric) state, whereas the noncentro symmetric (e.g. tetragonal) below the transition temperature usually shows a ferroelectric behavior in the perovskite oxides.

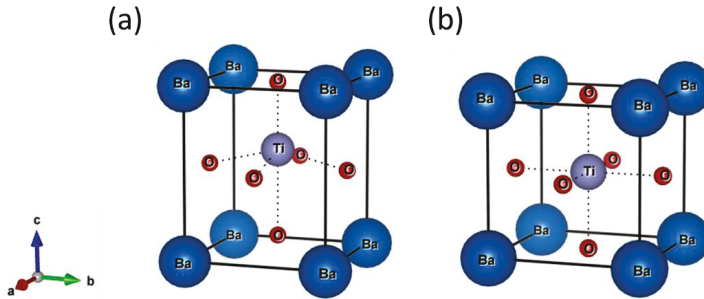


Figure 2-8: Sketch of the crystal structure of  $\text{BaTiO}_3$  (a) below and (b) above the phase transition temperature.

Figure 2-8 shows an example, the unit cell of  $\text{BaTiO}_3$  for the two phases. Above 393 K  $\text{BaTiO}_3$  possesses a cubic unit cell with the  $\text{Ti}^{4+}$  atoms at the body center. It undergoes a displacive structural phase transition to tetragonal structure at 393 K and  $\text{Ti}^{4+}$  moves a small amount along the z axis, while the  $\text{O}^{2-}$  moves a bit in the opposite direction. This displacements of the atoms break the cubic symmetry and the center of mass of the positive charges ( $\text{Ba}^{2+}$ ,  $\text{Ti}^{4+}$ ) does not coincide with the center of mass of the negative charges ( $\text{O}^{2-}$ ). As a result, a spontaneous electrical charges appear, and the material becomes ferroelectric.

It is obvious from figure 2-8 that the phase transition from the paraelectric to the ferroelectric state can be characterized by structural or electronic temperature-dependent analysis. However in real systems this often delivers values for the transition temperature that depend among others on the homogeneity of the sample, the choice of experiment, and even the criterion. Therefore we chose the Curie-Weiss temperature  $T_C$ , which can be determined more unambiguously and which is typically close to the phase transition temperature, to characterize the phase transition and, especially, its engineering. In the following, we will describe the Curie-Weiss law and Curie-Weiss temperature  $T_C$  and introduce the often used thermodynamic Ehrenfest classification with transition temperature  $T_0$ .

### 2.3.1 Curie-Weiss law

One way to characterize the phase transition is the use of the Curie-Weiss temperature  $T_C$ . It should be noted that the Curie-Weiss temperature and the temperature of the phase transition are not identical. Nevertheless, in most systems they are close to each other and often it is not easy to determine an exact temperature for the phase transition.

The electric susceptibility  $\chi$  describes the degree of polarization of a material in response to an applied electric field. The ratio between the polarization  $\mathbf{P}$  and the electric field  $\mathbf{E}$  defines the susceptibility:

$$\chi = \varepsilon - 1 = \frac{\mathbf{P}}{\varepsilon_0 \mathbf{E}} \quad (2-3)$$

where  $\varepsilon_0$  and  $\varepsilon$  are the permittivity of free space and of the given material, respectively. In the paraelectric state the temperature dependence of the electric susceptibility obeys the Curie-Weiss law:

$$\chi = \frac{C}{T - T_C} \quad (2-4)$$

where C is the Curie constant and T is the temperature.

Using these two equations and assuming, that  $\varepsilon \gg 1$ , we obtain the temperature dependence of the permittivity in the paraelectric state:

$$\frac{1}{\varepsilon} \approx \frac{1}{C} (T - T_C). \quad (2-5)$$

This linear temperature dependence allows us to determine  $T_C$  and C in our experimental results.

Microscopically, the thermal vibrations of the atoms in the solid lead to increasing fluctuations as temperature arising and finally lead to a change of the structure of the crystal. The detailed microscopic theory is different from material to material. However, macroscopically the thermodynamic Landau theory provides a useful descriptions for many different ferroelectrics.

### 2.3.2 Landau theory

The order parameter represents the quantity which can be used to describe the order of a system. For instance, the order parameter of a liquid, a ferromagnet, or a ferroelectric is the density, magnetization, or polarization, respectively.[31] Phase transitions are generally classified according to the Ehrenfest classification. The order of a phase transition is defined to be the order of the lowest-order derivative, which changes discontinuously at the phase boundary, i.e.:

- (i) The first order phase transitions, or discontinuous transition, happens due to the lack of a symmetry relationship between the two phases, i.e. there's no point where the two

phases are indistinguishable. In this case the phase transition is accompanied by release of heat (latent heat).

- (ii) The second order, or continuous, phase transitions, refers to the continuously decrease of the order parameter (e.g. spontaneous polarization in ferroelectrics) at the transition temperature.

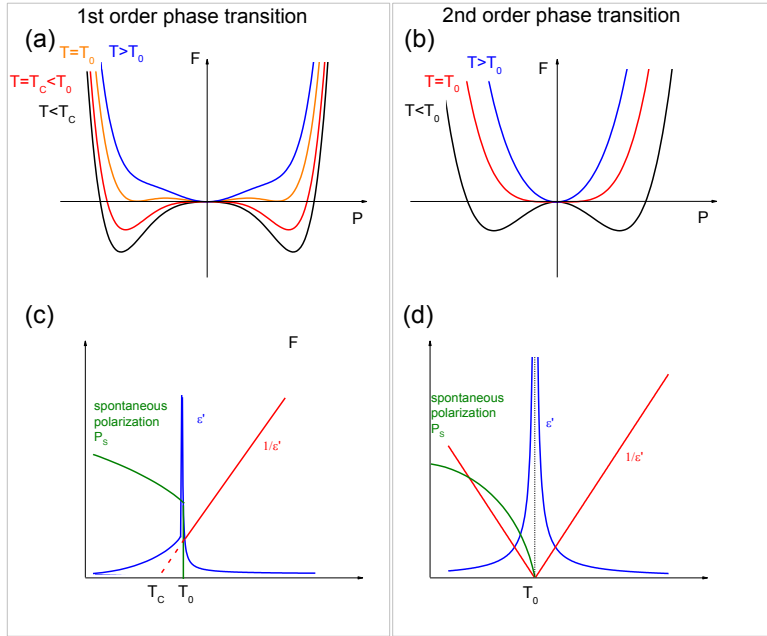


Figure 2-9: Sketches of 1<sup>st</sup> order and 2<sup>nd</sup> order phase transitions. Free energy as a function of the polarization (a) first order, at  $T > T_0$ ,  $T = T_0$ ,  $T = T_c < T_0$ , and  $T < T_c$ , (b) second order at  $T > T_0$ ,  $T = T_0$ , and  $T < T_0$ . Spontaneous polarization  $P(T)$ , permittivity and its inverse as a function of temperature for (c) 1<sup>st</sup> order and (d) 2<sup>nd</sup> order phase transitions.

For the ferroelectric phase the free energy  $F$  can be described by:[32]

$$F(T) = F_0(T) + \frac{1}{2}aP^2 + \frac{1}{4}bP^4 + \frac{1}{6}cP^6 + \dots - EP \quad (2-6)$$

where  $F_0(T)$  describes the temperature dependence of the high temperature phase near the phase transition.  $P$  is the polarization,  $E$  is the electric field, and  $a$ ,  $b$ ,  $c$  are the unknown and temperature dependent coefficients. To simplify this expression, we neglect the dependence of the parameters on  $P$  and consider  $E=0$ . The value of  $P$  in thermal equilibrium is given by the minimum of  $F$  as a function of  $P$ . The equilibrium polarization satisfies the extremum condition:

$$\frac{\partial F(T)}{\partial P} = aP + bP^3 + cP^5 + \dots \quad (2-7)$$

In order to obtain a ferroelectric state the coefficient of the term in  $P^2$  in eq. (2-6) goes through zero at the temperature  $T_0$ :

$$a = a_0(T - T_0) \quad (2-8)$$

where  $a_0$  is taken as a positive constant. The first order and second order phase transition can be describe as:

- (i) consider  $b < 0$ , in this case  $c$  should be positive in order to keep  $F$  to be positive. This is sketched in Figure 2-9(a). If  $T < T_0$  ( $a < 0$ ), the free energy may have a minimum at non-zero  $P$ . This case describes a first order phase transition.  $T_C$  is Curie-Weiss temperature and  $T_0$  is the transition temperature;

- (ii) when  $b > 0$ ,  $c$  can be neglected. The polarization for zero applied electric field is:

$$a_0(T - T_0)P + bP^3 = 0 \quad (2-9)$$

and the free energy has a minimum at the origin when  $a_0 > 0$  or  $P^2 = a_0(T - T_0)/b$  when  $a_0 < 0$  (Figure 2-9(b)). This case describes a second order phase transition since the polarization goes continuously to zero at the transition temperature.

In the following, the phase transition is characterized by the measurement of the Curie-Weiss temperature (see example in Appendix C).

## 2.4 Engineering the phase transition

During the phase transition, the macroscopic and microscopic properties of materials show interesting changes:

- (i) the dielectric response shows a peak near the phase transition temperature.[33, 34]
- (ii) the piezoelectric coefficient is enhanced near the phase transitions,[16] and
- (iii) the material shows an increase of conductivity at the phase transition.[35-37]

As a consequence, it is of great interest to shift the phase transition temperature to the operation temperature (e.g. room temperature) in order to create materials with superior properties. The electric properties of oxides can be altered using doping or in case of epitaxial films the misfit strain between film and substrates (i.e. clamping effect), or a combination of both.

### 2.4.1 Doping

The substitution of cations at the A-site of the  $ABO_3$  perovskites results in a change of the microstructure and, therefore, the ferroelectric properties. Generally the substitutions in

perovskites obeys the Goldschmidt tolerance factor, which is imposed by the ionic radii of the cations:[38]

$$t = \frac{R_A + R_O}{\sqrt{2}(R_B + R_O)} \quad (2-10)$$

where  $R_A$ ,  $R_B$ , and  $R_O$  are ionic radii of A-site and B-site cations, and oxygen, respectively. Generally perovskites exhibit a tolerance factor of  $0.78 < t < 1.05$ . [39] Too large A-site cations or too small cations cannot crystallize in the perovskite structure under equilibrium conditions. The variation in ionic radii induces either deformations or rotations of  $\text{BO}_6$  octahedra, which leads to a decrease of the symmetry. As a result, the unit cell symmetry is lowered from cubic to tetragonal, orthorhombic, or rhombohedral crystal structure (see Figure 2-10).

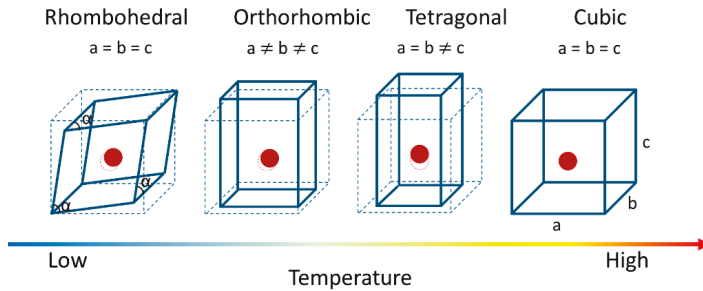


Figure 2-10: Sketch of perovskite structure distortion from cubic (high temperature) to tetragonal, orthorhombic, and rhombohedral (low temperature) for  $\text{BaTiO}_3$ . Red dot indicates the distortions of the off-centered B-cation.

One of the most direct methods to introduce ferroelectricity into  $\text{SrTiO}_3$  is doping with other cations (e.g.  $\text{Ba}^{2+}$ ,  $\text{Ca}^{2+}$ , or  $\text{Bi}^{2+}$ ). For pure  $\text{SrTiO}_3$   $t \cong 1$  and for  $\text{BaTiO}_3$ ,  $t \cong 1.06$ . Actually  $t > 1$  means that the  $\text{Ti}^{4+}$  ion is too smaller and/or that the  $\text{Ba}^{2+}$  is large.[40] In  $\text{Ba}_x\text{Sr}_{1-x}\text{TiO}_3$  with  $x > 0.2$ , the crystal structure undergoes a sequence of phase transitions from cubic to different ferroelectric phases: tetragonal, orthorhombic, and rhombohedral as shown in Figure 2-10. For  $x < 0.2$ , the Curie-Weiss temperature  $T_C$  varies proportional to  $(x - x_c)^{1/2}$ , where  $x_c = 0.035$  is the critical concentration. For  $x > x_c$   $\text{Ba}_x\text{Sr}_{1-x}\text{TiO}_3$  reveals a clearly “classical” ferroelectric behavior, i.e. dielectric response without frequency dependence, whereas for  $x < x_c$  its permittivity shows a strong frequency dispersion,[41] i.e. here  $\text{Ba}_x\text{Sr}_{1-x}\text{TiO}_3$  shows a so called “relaxor” or “glass-like” ferroelectric behavior.

## 2.4.2 Strain

Strain in perovskites provides another option for the engineering of the dielectric properties of the materials. In this study, we mainly focus on the strain induced by an underlying substrate. It is worth to note that bulk crystals typically crack under moderate strains of only 0.1%, while in biaxial films the strain can reach up to a few percent before crack occurs. The limit of strain without crack formation in thin film is given by the Griffith criteria:[42]

$$\epsilon_s = (1 - \nu) \sqrt{\frac{2\gamma}{\pi E t}}, \quad (2-11)$$

where  $\nu$  is the film's Poisson's ratio,  $\gamma$  is surface energy,  $E$  is the Young's modulus, and  $t$  is the thickness. According to Frank and van der Merwe,[43] the biaxial strain is defined as:

$$\epsilon_s = \frac{a - a_0}{a_0}, \quad (2-12)$$

where  $a_0$  is the lattice parameter of the film material under stress free conditions and  $a$  is the measured in-plane lattice parameter of the strained film. It has been demonstrated that the biaxial strain can shift the transition temperature of ferroelectrics and superconductors,[44] it is even used to enhance the mobility of charge carriers in semiconducting material.[45] The in-plane strain modifies the structure of films by:

- (i) The change of the in-plane lattice parameters. Typically, the in-plane modification is partially compensated by the change of opposite sign of out of plane lattice parameters (Poisson effect). As a result, a structure distortion (e.g. from cubic to orthorhombic) can be triggered.[34, 46]
- (ii) Modification of the density of dislocations.[47, 48] Typically film with a thickness exceeding a certain characteristic thickness (one fifth of the Matthews-Blakeslee critical thickness (see chapter 4)) starts to accumulate a high density of dislocations.[49] This leads not only to a higher conductance, but also to a relaxation of the strain.

As a consequence, the ferroelectric and conductive properties can be modified due to the strain-induced change of the structure and defect density of the material. Figure 2-11 shows sketches of tensely and compressively strained films grown on a substrate with a misfit lattice parameters. High-quality substrates are required for coherently strained films. Either various scandates (i.e. DyScO<sub>3</sub>, TbScO<sub>3</sub>, GdScO<sub>3</sub>, and SmScO<sub>3</sub>) or different dopings (i.e. Ba<sub>x</sub>Sr<sub>1-x</sub>TiO<sub>3</sub>) are used to provide various misfit lattice parameters in this work.

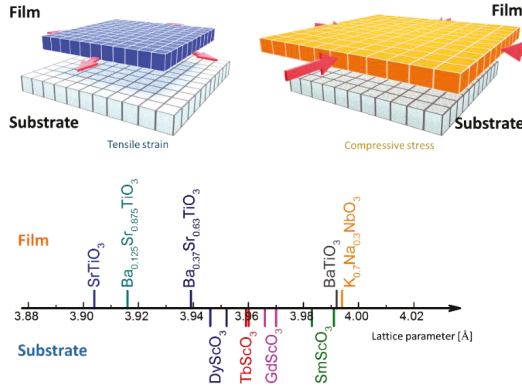


Figure 2-11: Sketch of heteroepitaxy leading to tensile and compressive strain and in-plane lattice parameters of various materials studied in this work. Here the situation of different doped films is sketched.

Several theoretical approaches have been developed to explain and understand the strain induced modification of the ferroelectric properties.[50] For instance, a strain-phase diagrams for SrTiO<sub>3</sub> can be generated via thermodynamic analyses by assuming a single domain state for all possible ferroelectric phases in a thin film.[15]

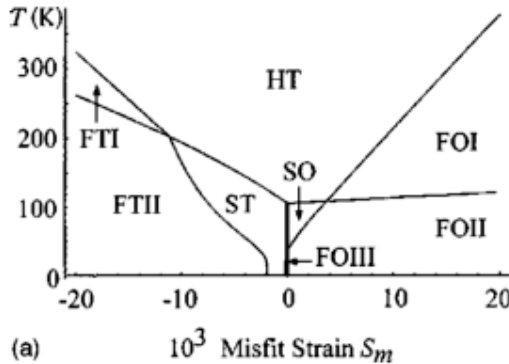


Figure 2-12: The strain-phase diagram of SrTiO<sub>3</sub>, where high symmetry tetragonal, purely “structural” tetragonal and orthorhombic states, purely ferroelectric tetragonal and orthorhombic phases, and three “mixed” states are labelled HT, ST, SO, FTI, FOI, FTII, FOII, and FOIII, respectively. (adapted from ref.[15]).

Figure 2-12 shows the resulting strain-phase diagram calculated from this thermodynamic analysis. It indicates that room temperature ferroelectricity can be obtained in SrTiO<sub>3</sub> with sufficiently large tensile strain of approximately  $\epsilon \cong 0.15\%$ . In a similar way, we can evaluate the expected temperature for the phase transition of our films. By minimizing the Helmholtz free energy  $F$  expressed as a function of the polarization (see eq. (2-6) one can evaluate the expected

transition temperature. For film with a misfit strain the free energy  $F$  has to be described as a function of strain, temperature, and polarization. The relevant general expression is given in ref[15]. The minima of the free energy  $F$  with respect to the polarization and structural order parameter represent the energetically favorable phase, i.e. the equilibrium single domain thermodynamic states. For  $\text{SrTiO}_3$ , a positive strain and a temperature  $T > 120$  K, the shift of  $T_C$  is given by:

$$\Delta T_C = 2\varepsilon_0 C(Q_{11} + Q_{12})\varepsilon_s / (s_{11} + s_{12}), \quad (2-13)$$

where  $\varepsilon_0$  is the permittivity of vacuum,  $C$  is the Curie-Weiss constant,  $Q_{ij}$  and  $s_{ij}$  represent the electrostrictive coefficients and elastic compliances, and  $\varepsilon$  is the strain.

## 2.5 Piezoelectricity

The piezoelectric effect describes the ability of a material to generate an electric field in response to an applied mechanical stress. When a piezoelectric is placed under mechanical stress, the atomic structure of the crystal changes resulting in a shift of the positively and negatively charged sublattice, which resulting the generation of an electric field. The piezoelectric effect is reversible, i.e. the materials generates stress when an electric field is applied. The electric field is proportional to the stress. For small fields, the constitutive relation for a piezoelectric material can be written as:[51, 52]

$$\begin{bmatrix} \varepsilon_1 \\ \varepsilon_2 \\ \varepsilon_3 \\ \varepsilon_4 \\ \varepsilon_5 \\ \varepsilon_6 \end{bmatrix} = \begin{bmatrix} S_{11} & S_{12} & S_{13} & 0 & 0 & 0 \\ S_{12} & S_{11} & S_{13} & 0 & 0 & 0 \\ S_{13} & S_{13} & S_{33} & 0 & 0 & 0 \\ 0 & 0 & 0 & S_{44} & 0 & 0 \\ 0 & 0 & 0 & 0 & S_{44} & 0 \\ 0 & 0 & 0 & 0 & 0 & 2(S_{11} - S_{12}) \end{bmatrix} \begin{bmatrix} \sigma_1 \\ \sigma_2 \\ \sigma_3 \\ \tau_{23} \\ \tau_{31} \\ \tau_{12} \end{bmatrix} + \begin{bmatrix} 0 & 0 & d_{31} \\ 0 & 0 & d_{31} \\ 0 & 0 & d_{33} \\ 0 & d_{15} & 0 \\ d_{15} & 0 & 0 \\ 0 & 0 & 0 \end{bmatrix} \begin{bmatrix} E_1 \\ E_2 \\ E_3 \end{bmatrix}, \quad (2-14)$$

and

$$\begin{bmatrix} D_1 \\ D_1 \\ D_1 \end{bmatrix} = \begin{bmatrix} 0 & 0 & 0 & 0 & d_{15} & 0 \\ 0 & 0 & 0 & d_{15} & 0 & 0 \\ d_{31} & d_{31} & d_{33} & 0 & 0 & 0 \end{bmatrix} \begin{bmatrix} \sigma_1 \\ \sigma_2 \\ \sigma_3 \\ \sigma_4 \\ \sigma_5 \\ \sigma_6 \end{bmatrix} + \begin{bmatrix} e_{11}^\sigma & 0 & 0 \\ 0 & e_{11}^\sigma & 0 \\ 0 & 0 & e_{33}^\sigma \end{bmatrix} \begin{bmatrix} E_1 \\ E_2 \\ E_3 \end{bmatrix}, \quad (2-15)$$

where  $D$  is the electric displacement,  $S$  is the strain,  $E$  is the applied electric field, and  $\sigma$  is the stress. Furthermore,  $\epsilon$  is the permittivity,  $s$  is the elastic compliance,  $d$  is the piezoelectric coefficient. The superscripts  $^{\sigma}$  indicates that the quantity is measured at constant stress. The piezoelectric constants are tensors and relate to both the direction of the applied stress and the electric field. The subscript numbers refer to the axes and directions of deformation as shown in Figure 2-13.

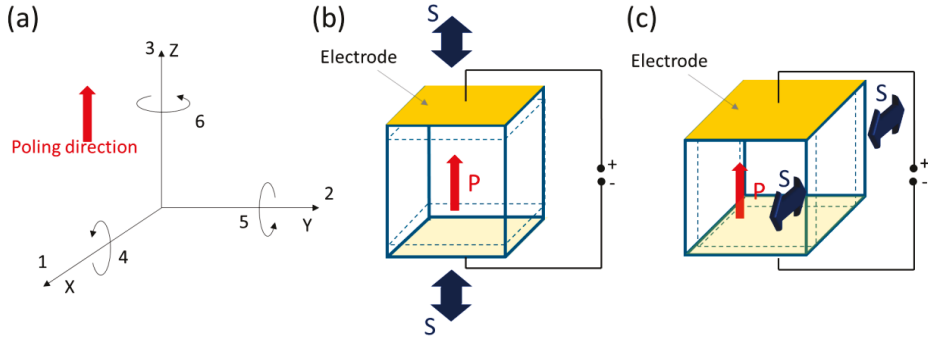


Figure 2-13: (a) Sketch of the axes and directions of deformation, and as examples (b)  $d_{33}$  and (c)  $d_{31}$  coupling modes.

One of the most used constant to characterize the piezoelectric properties of a material is the piezoelectric coefficient. It is defined by the electric polarization generated in a material as function of the applied mechanical stress:

$$d_{ij} = \frac{P}{S}, \quad (2-16)$$

where  $P$  is polarization, and  $S$  is the stress. In  $d_{ij}$ , the first subscript refers to the direction of polarization generated in the material, the second refers to the direction of the applied stress or to the direction of the induced strain. A sketch of the axes and directions of deformation is given in Figure 2-13. For instance,  $d_{33}$  describes the polarization in z direction for a force pointing in z-direction, whereas  $d_{31}$  correlates the polarization in z-direction and the strain in x-direction. Generally large  $d_{ij}$  constants relate to large mechanical displacements which are of advantage for motional transducer devices like the SAW employed in this work. The piezoelectric coefficient  $d_{ij}$  directly affects the effective electromechanical coupling coefficient  $k_{eff}$ . The electromechanical coupling coefficient  $k_{eff}$  represents the ability of a piezoceramic material to transform electrical energy to mechanical energy and vice versa:

$$k_{eff}^2 = \frac{\text{energy converted}}{\text{input energy}}, \quad (2-17)$$

A possible and important application of the piezoelectric effect is given by device based on SAW. A SAW is an acoustic wave traveling along the surface of a material. Its amplitude typically decays exponentially with depth into the substrate. The directly piezoelectric coupling to SAW is achieved by interdigitated transducers on top of a piezoelectric material. When a potential is applied to a pair of electrodes, it causes a periodic displacement of the surface which can generate a wave, i.e. a SAW. The details on the setup of SAW devices are discussed in chapter 3.

## 2.6 Conductivity

Most of the perovskites are dielectric, i.e. it is an electrical insulator that can be polarized by an applied electric field. Basically, an insulator has a band gap of more than 3 eV. However, insulators can become electrically conductive when a sufficiently large voltage is applied or proper defects are induced.

### 2.6.1 Oxygen vacancy in SrTiO<sub>3</sub>

In our oxides materials, a typical defect contributing to electrical conduction is oxygen vacancy in the structure. Their density and mobility can be affected by different means, e.g. temperature, doping, and strain.[53, 54] This provides the tunability of the conduction in oxides.

As any other solid, oxide contains a certain concentration of defects. These defects can be located either at surface or interface or they are embedded in the bulk of the material. Depending on their location different mechanisms have to be considered for the resulting conductivity.[37, 55, 56]

Schottky defects are typically formed close to the surface or to grain boundaries. Vacancies represent one kind of defects. They are an empty lattice site in the ideal crystal structure. Because the atoms can be neither created nor destroyed within a closed system, the removed atom which resulting a vacancy has to move somewhere. One way to accommodate the removed atom is to move it to the boundary of the solid. This is called Schottky-disorder (Figure 2-14(a)). Atoms can also sit in between the regular lattice structure, occupying the interstitial lattice sites. This is so called Frenkel-disorder (Figure 2-14(b)). The Frenkel-defects require sufficient space in the crystal lattice for the atoms. As a consequence, Frenkel-defects are unlikely in close-packed crystals.

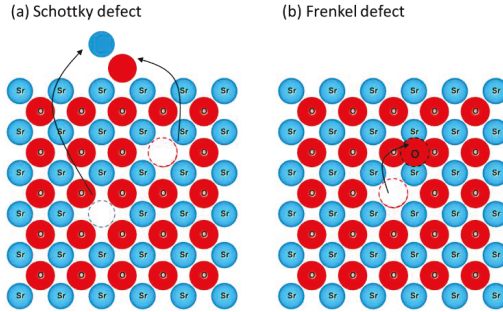


Figure 2-14: Sketch of Schottky defects and Frenkel defects in an ionic crystal.

In the densely packed crystal lattice of  $\text{SrTiO}_3$ , the only feasible type of intrinsic disorder is the Schottky disorder.[57] The oxygen vacancies are positively charged and act as donors. The mobility of oxygen vacancies is much higher than that of cation vacancies in  $\text{SrTiO}_3$  at temperature below 1400 K. The oxygen exchange reaction is given by:[56]



where  $O_O$  is the oxygen ions on a regular lattice site,  $V_O^{\bullet\bullet}$  is the oxygen vacancies according to notation of Kröger and Vink. The energy of oxygen vacancies is situated just below the conduction band and act as a donor-type defect, see Figure 2-15.

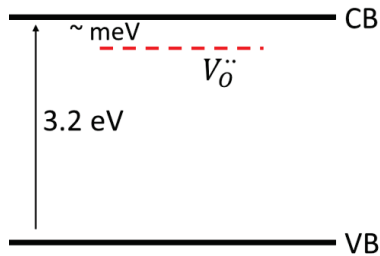


Figure 2-15: Schematic sketch of the energy levels of oxygen vacancy in  $\text{SrTiO}_3$ .

### 2.6.2 Resistance switching behavior

Oxygen vacancies cannot only modify the conductance of oxides, but they can also be responsible for unique features like resistive switching behavior and plasticity (i.e. a switching

with variable resistive states). Thus proper prepared oxides can be ideal candidates for memristor devices.

In contrast to a field-effect-transistor device (e.g. CMOS) a memristor represents a two-terminal device (see figure 2-16(a)), which means the same two terminals are responsible for the input signal to modify the output state and for the reading of the output signal. There are various kinds of materials which show a memristive behavior. The mechanisms can be completely different for the different materials. Most memristors are based on electronically driven materials, like ferroelectric, phase change, or spin torque materials. The detailed atomic-scale dynamics that is responsible for the switching in these systems is still unknown. Another type of the memristor is using defect driven materials. In this case the switching behavior is based on the formation of metallic filaments or oxygen diffusion. Electric field and temperature gradation can be used to control the switching behavior in such materials.

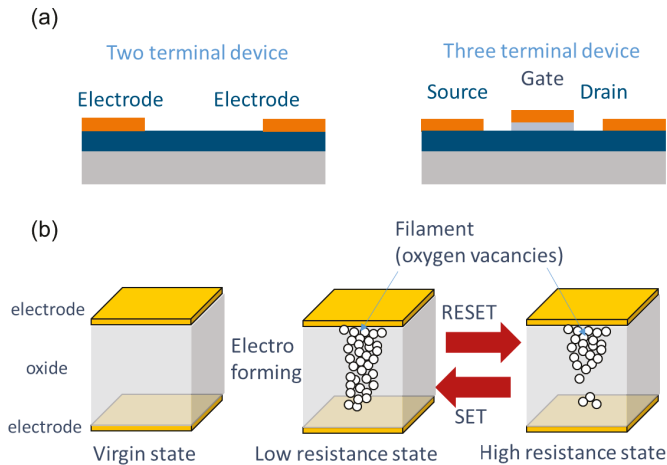


Figure 2-16: Sketches of two terminal device and three terminal device (a) and the formation of conductive filaments and switching behavior in oxides (b).

In this work, we will focus on memristor which is operated by controlling the oxygen vacancy diffusion in oxides leading to the reversible formation and disruption of conducting filaments. Figure 2-16(b) shows a sketch of the operation of such memristor which basically consists of three steps:

- i) Electroformation: In the origin state an electric stimulus is applied on the metal-oxide-metal structure which transfer the oxide from the insulating to the conducting state by forming filaments of oxygen vacancies.[57]

- ii) Reset: After the forming process, the conducting filament, which is formed by oxygen vacancies in oxides, connects the two electrodes. The device shows a low resistance state. In order to change the resistance state of the device, a large enough voltage of opposite sign is applied to move part of the oxygen vacancies back. As a consequence the metallic filaments break and the resistance between the two electrodes rises to the high resistive off state. This is the reset process.
- iii) Set: In order to switch back to the low resistance state, a set process is needed. A reversed voltage is applied between the two electrodes. The oxygen vacancies drift back to the electrode with negative voltage under electric field and form the metallic filament again. As a result the device shows the low resistive off state.

In figure 2-17, a schematic current-voltage curve of a memristor shows the switching and indicates a possible additional effect, the plasticity. The reversible changes can be ascribed to electrically induced redox-processes taking place in the oxide and/or at the oxide electrode interface. The plasticity behavior, also indicated in figure 2-17, is caused by the size and number of conducting filaments which depend on the switching characteristic like amplitude or repetition rate of set pulses. Since the mobility of the oxygen vacancies represents the dominant mechanism in this device, the tuning of oxygen vacancies, e.g. migration properties, via stain is a possible way to manipulate the resistive switching behavior.

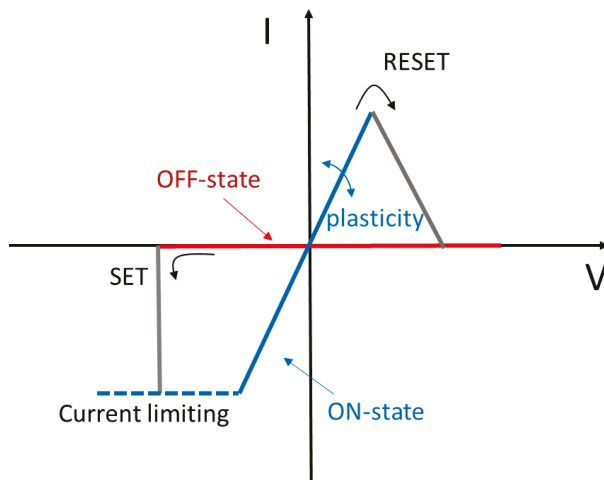


Figure 2-17: Schematic current voltage curve of a memristor with different stages of the switching procedure. The plasticity is indicated by the arrow showing that the slope (i.e. conductivity of the ON-state can vary.)

Due to its hysteretic I-V characteristic, the memristor which can be used as a non-volatile data storage, and a logic device at the same time. Moreover, combine both resistance switching and plasticity behavior, the device can emulate the biological synapses function in neuromorphic circuits. In the traditional von Neumann computational architectures, the system is divided into several parts, e.g. memory, control processing, and data paths. This separation can lead to serious bottlenecks because information has to be transferred repeatedly between different units of the system. In contrast, due to its switching and plasticity properties, the memristor can act as a memory and processor without extra data transfer. As a result the different computational elements might be mixed and used for a dynamic, self-learning system based on memristors with plastic behavior. This novel strategy is called neuromorphic computing. However even more simple devices are feasible, which are summarized in the discipline Neuromorphic Engineering.

However, there are still many open issues regarding the resistive switching and filament formation in neuromorphic devices. For instance, the physics of the resistive switching is still being discussed, it could for instance be due to metal-insulator or amorphous-crystalline transitions, or the generation, distribution, and redistribution of defects/ions in the device is not really understood. In Chapter 6, we will discuss how these effects can be triggered and controlled by strain in oxide films.

## 3. Sample preparation and experimental techniques

In this chapter, the experimental techniques and sample preparation are introduced that are used in this work. It starts with the film deposition methods. Then several film characterization techniques are introduced, including the methods used for the analysis of the structural, morphology, and stoichiometry of the films. The last part of this chapter is dedicated to the discussion of the device design and its preparation used for the temperature control and the electrical characterization of the strained ferroelectric films.

### 3.1 Thin film deposition

Two types of oxide film deposition techniques are involved in this work. Pulsed laser deposition (PLD) is used to prepare  $(\text{Ba,Sr})\text{TiO}_3$  films in the Forschungszentrum Jülich (FJZ)<sup>1</sup> and  $(\text{K,Na})\text{NbO}_3$  films are deposited via metal-organic chemical vapor deposition (MOCVD) at the Leibniz-Institut für Kristallzüchtung (IKZ) in Berlin<sup>2</sup>.

#### 3.1.1 Pulsed laser deposition

The PLD is a well-established deposition technique for thin film preparation. It represents an evaporation technology using a laser beam for the evaporation of the target material. Due to its flexibility it is ideal for the research on thin films where parameters have to be optimized, stoichiometries modified as other problems are examined in a very flexible way. As such it turns out to be ideal for our research, i.e. the preparation of thin epitaxial oxide films with different stoichiometries (e.g.  $(\text{Ba}_x\text{Sr}_{1-x})\text{TiO}_3$ ) on various single crystalline substrates with different lattice parameters (i.e. different lattice match between film and substrate).[58]

---

<sup>1</sup> In cooperation of the author with Dr. Jürgen Schubert and Willi Zander

<sup>2</sup> In cooperation of the author with Dr. Jutta Schwarzkopf and coworkers

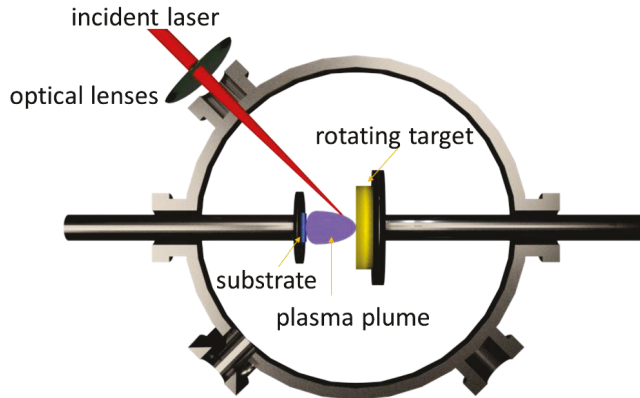


Figure 3-1: Sketch of the principle of pulsed laser deposition (PLD).

The work principle of PLD is as shown in Figure 3-1. An intense laser pulse is focused onto a target surface in a chamber, where it is (mainly) absorbed. Above a certain laser power, material from target is removed in the form of an ejected luminous plume. The target material of the plasma plume is then deposited on the substrate. There are several advantages from the PLD process. For instance, since the laser source is outside the vacuum chamber almost any condensed mater that absorbs the laser beam can be ablated; the well-defined (frequency, duration, and power of the beam) pulsed nature of PLD means that the film growth rate and thickness can be controlled in a perfect way; the kinetic energies of the ablated species arriving at the substrate can be controlled in a certain range.

In this work the main advantage of this method is the well-defined and stoichiometric transfer of the target composition to the substrate. However, there are also fundamental drawbacks of PLD, such as the production of large agglomerates (droplets) of material on the film during the ablation process, the large number of crystallographic defects in the film caused by the higher kinetic energy of ablation particles compared to other deposition techniques like chemical vapor deposition or classical evaporation.

In this work, sintered ceramic targets with stoichiometric  $\text{SrTiO}_3$ ,  $\text{Ba}_{0.125}\text{Sr}_{0.875}\text{TiO}_3$ ,  $\text{Ba}_{0.37}\text{Sr}_{0.63}\text{TiO}_3$ , and  $\text{BaTiO}_3$  are used for the PLD at Forschungszentrum Jülich. The corresponding epitaxial films are deposited on  $\text{DyScO}_3$  (110),  $\text{TbScO}_3$  (110) and  $\text{GdScO}_3$  (110) single crystalline substrates with various thickness ranging from 5 nm to 200 nm. The laser power was  $5 \text{ J/cm}^2$  with a repetition rate of 10 Hz. The process gas was oxygen at a pressure of 1 Pa, and a growth temperature of typically  $700 \text{ }^\circ\text{C}$  was used in order to facilitate epitaxial growth of the oxide films.

### 3.1.2 Metal-organic chemical vapor deposition

The MOCVD is a special chemical vapor deposition technique used to produce oriented or epitaxial films (including oxide films) of high quality. It is based on the pyrolysis reaction of the targeted elements. These precursor molecules are transported by a carrier gas ( $H_2$ ,  $N_2$ ) onto a heated substrate. The deposition and film growth is then dominated by a surface chemical reaction.

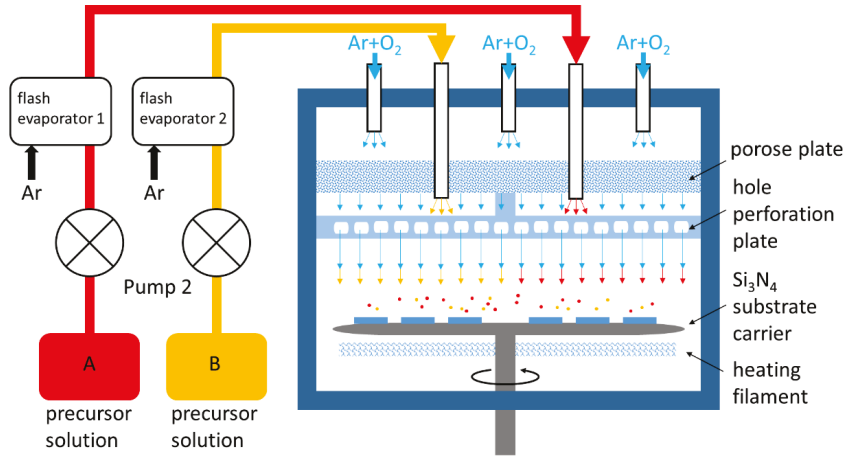


Figure 3-2: Sketch of the metal-organic chemical vapor deposition setup at the Leibniz-Institut für Kristallzüchtung, Berlin. Adapted from [59].

Figure 3-2 shows a sketch of MOCVD setup adapted from ref.[59]. In this work, MOCVD is used for the growth of  $(K_xNa_{1-x})NbO_3$  films on series scandites substrates, i.e.  $DyScO_3$  (110),  $TbScO_3$  (110),  $GdScO_3$  (110), and  $SmScO_3$  (110).  $K(thd)$  and  $Na(thd)$  ((thd) = 2,2,6,6-tetramethyl-3,5-heptanedione) and  $Nb(EtO)_5$ , dissolved in dry toluene at a concentration of 0.01 M, are used as source materials for Na and Nb, respectively. The films are deposited at a gas pressure of 2.6 kPa. A substrate temperature of 973 K offers the best condition for epitaxial growth of these oxides. In this work, a typical K to Na ratio of the precursor of 0.3:0.7, and an  $O_2$  to Ar ratio of 0.63 was used.

### 3.2 Film characterization

After the growth of the film, structure, stoichiometry, and morphology of the film are characterized in order to learn more about the quality and properties of the film. The technologies used for this purpose are sketched in the following sections.

### 3.2.1 X-ray diffraction

The crystalline structure of samples is analyzed by various X-ray diffraction (XRD) techniques. XRD is an electromagnetic radiation of wavelength ranging from 0.01 to 10 nanometers. To produce significant diffraction, the spacing  $d$  between the parallel crystalline planes and the wavelength of the impinging wave should be similar in size. The electrons of the atoms interact with the X-ray and produce secondary spherical waves emanating from the electron, leading to an elastic scattering of the X-ray. In case of a regular lattice (e.g. crystalline structure), most of the scattered waves cancel one another due to destructive interference, however some of them interfere in a constructive way in a few specific directions which are given by Bragg's law:

$$2d_{hkl} \sin \theta = n \lambda \quad (3-1)$$

where  $d_{hkl}$  is the spacing between diffracting planes,  $\theta$  is the incident angle,  $n$  is an integer, and  $\lambda$  is the wavelength of the incident beam. In a crystalline structure Miller indices (hkl) identify different planes of atoms, and the crystallographic direction [hkl] represents the vector normal to (hkl).

(a)

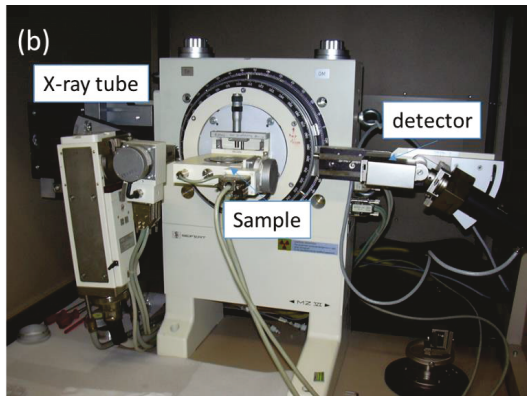
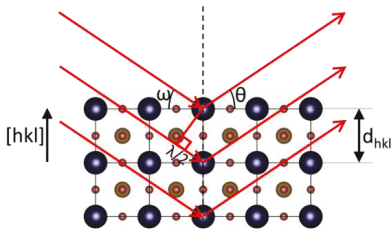


Figure 3-3: (a) Sketch of XRD for a lattice of a perovskite, and (b) image of one of the X-ray geometer used in this work.

In this work, first Bragg-Brentano scans are used to study the lattice mismatch between film and substrate, and the composition, relaxation, and thickness of the film. In the Bragg-Brentano geometry (see Figure 3-4) the angles of incident and detected X-ray beam are identical, i.e.  $\omega = \theta$ . As a result a single crystal specimen produces only one family of peaks in the diffraction pattern, i.e. the peaks for  $n \cdot d_{hkl}$  (see Figure 3-4b). Using for instance a Nelson-Riley fit of the series of peaks, we obtain an accurate determination of the out-of-plane lattice parameter  $d_{hkl}$  of the

crystalline structure. Similarly the thickness of a layer can be obtained by analyzing the constructive interference of the surface and bottom (interface between film and substrate) of the film.

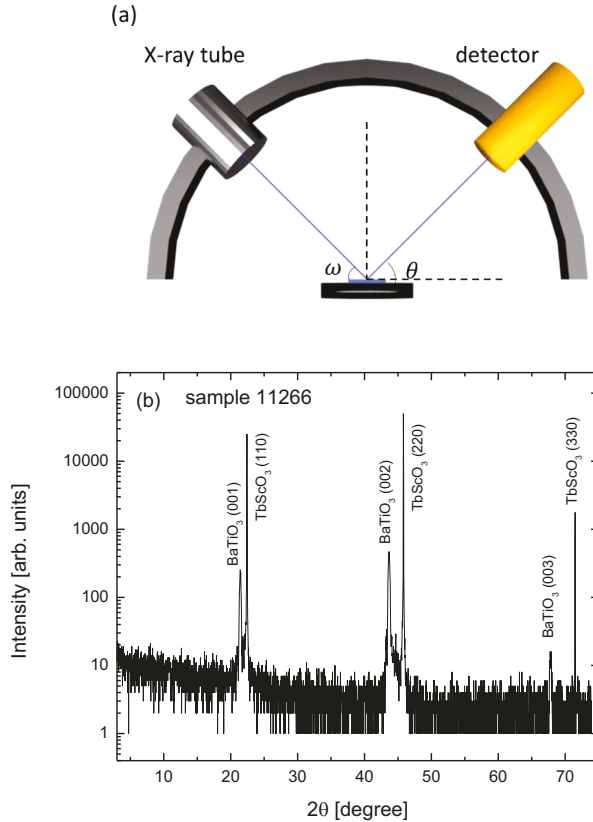


Figure 3-4: (a) Sketch of an XRD Bragg-Brentano scan. The incident angle  $\omega$  is defined by the X-ray source and the sample surface. The diffracted angle  $2\theta$  is defined by the incident beam and the detector angle. (b) Bragg-Brentano scan of an epitaxial  $\text{BaTiO}_3$  film ( $001$ ) orientation) on a  $\text{TbScO}_3$  ( $110$ ) substrate.

Figure 3-5 shows a series of Bragg-Brentano scans of  $\text{SrTiO}_3$  films of different thickness grown on  $\text{DyScO}_3$  substrates.

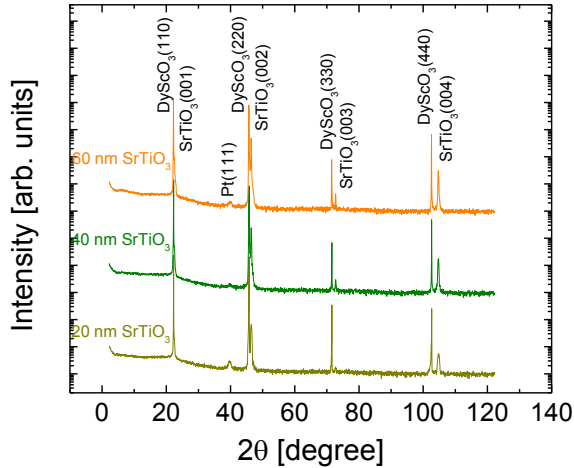


Figure 3-5: Bragg-Brentano scans of epitaxial SrTiO<sub>3</sub> layers of 20, 40, and 60 nm thick with (001) orientation on DyScO<sub>3</sub>(110) substrate. The Pt(111) peak is caused by the 20 nm Pt layer used as electrodes.

Second, rocking curves can be used to get an idea on the homogeneity of the sample. Rocking curves (see Figure 3-6) are recorded in a kind of Bragg-Brentano geometric ( $\omega' = \theta$ ), however, “rocking” the sample slightly, i.e.  $\omega' = \omega + \delta\omega$ . The resulting rocking curve (see Figure 3-6(b)) represents a mosaic spread, i.e. it shows how perfect a crystal is aligned. Crystal imperfections lead to a broadening of the rocking curve. Usually the full width at half maximum (FWHM) of the rocking curve is used to compare the quality of a crystal or the quality of epitaxy in case of epitaxially grown films.

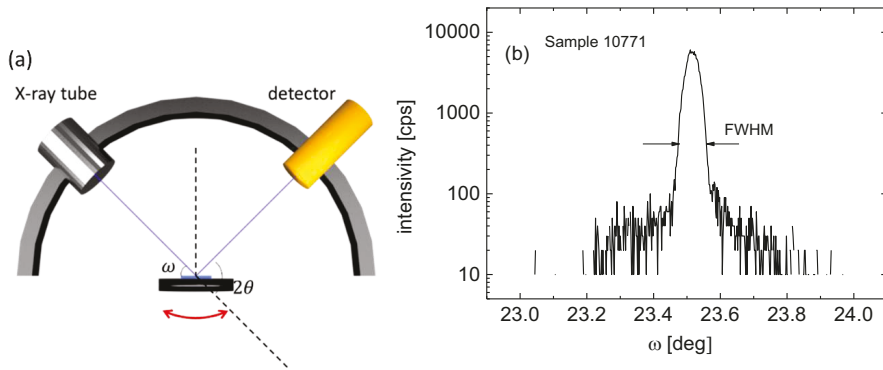


Figure 3-6: (a) sketch of an XRD rocking curve. (b) Result of a rocking curve on a 40 nm thick  $\text{SrTiO}_3$  film (sample number 10771) grown on a  $\text{DyScO}_3$  substrate with out-of-plane lattice parameter  $d_{\perp} = 0.3866$  nm and FWHM of 0.05 degrees.

The rocking curves (omega scan) of  $\text{SrTiO}_3$  films with a thickness ranging from 20 nm to 100 nm grown on  $\text{DyScO}_3$  substrate are given in Figure 3-7. No change of the FWHM is observed up to the film thickness of 105 nm. In a rocking curve, a perfect crystal should produce a very sharp peak. Defects (mosaicity, dislocations, and curvature) can create disruptions in the perfect parallelism of the planes and result in a broadening of the rocking curve. In Figure 3-7 the FWHM is about 0.08 deg for the film below 100 nm. For the film of 105 nm thick, it is 0.14 deg. This reveals that below 100 nm, the strained  $\text{SrTiO}_3$  grown on  $\text{DyScO}_3$  is less relaxed than thicker (above 100 nm) strained films. This could be caused by the cracks in the thicker films leading to a slightly curved film rather than perfectly flat one.

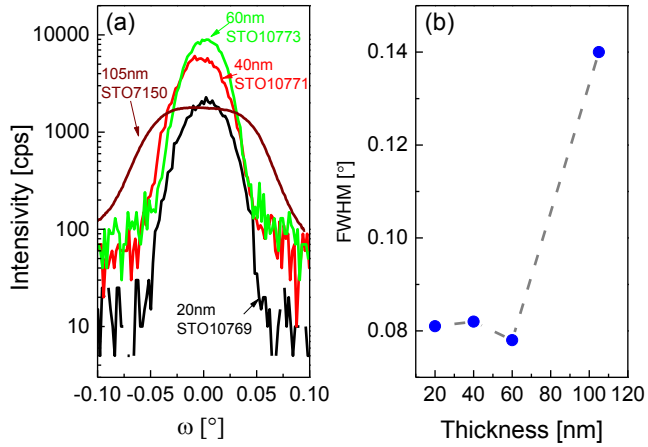


Figure 3-7: (a) Result of a rocking curve scan on the 20 nm, 40 nm, 60 nm, and 105 nm  $\text{SrTiO}_3$  film grown on  $\text{DyScO}_3$  substrate. (b) The FWHM as a function of film thickness.

Finally, reciprocal space mapping (RSM) provides the most complete information on the structure and epitaxy. It is vital for the analysis of our strained films. In principle RSM consists of a series of Bragg-Brentano (i.e.  $\omega - 2\theta$ ) scans, however each scan is collected with a slightly different tilt of  $\omega$  (see Figure 3-8(a)). By choosing adequate angular regime, the diffraction peaks of the film and substrate are recorded in a 2D plot revealing one in-plane and the out-of-plane lattice parameter for both systems. In this way it reveals the in-plane correlation of the lattice parameters (i.e. the epitaxy), the strain (i.e. deviation from the literature value), and even the strain relaxation for our strained epitaxial films.

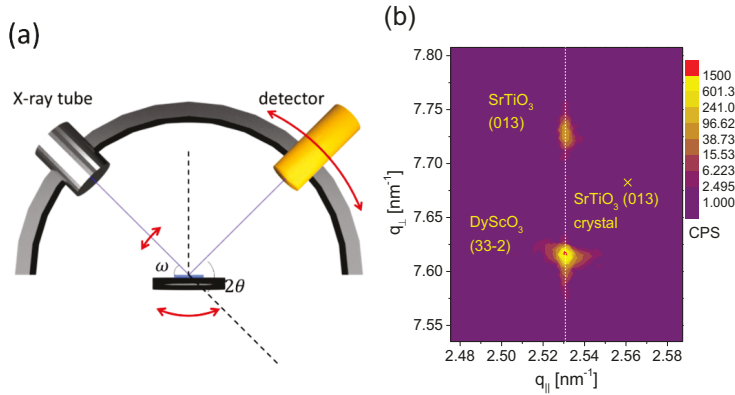


Figure 3-8: (a) Sketch of an XRD RSM. (b) Result of a RSM on a 90 nm thick  $\text{SrTiO}_3$  film (sample number 10773) grown on a  $\text{DyScO}_3$  (110) substrate.

Figure 3-8(b) shows a typical RSM result obtained for an epitaxial  $\text{SrTiO}_3$  film on  $\text{DyScO}_3$  simultaneously the  $(33\bar{2})$  relax of  $\text{DyScO}_3$  ( $33\bar{2}$ ) and the (013) reflex of  $\text{SrTiO}_3$  are mapped. The positions  $q_{\parallel}$  and  $q_{\perp}$  of the different reflexes reveal the d-spacing and the tilt of the diffracting planes of film and substrate. The epitaxial perfection is indicated by the fact, that the peak positions of film and substrate are identical with respect to  $q_{\parallel}$ . The difference between the experimental value and the literature value for unstrained material, reveals the resulting strain (in-plane and out-of-plane).

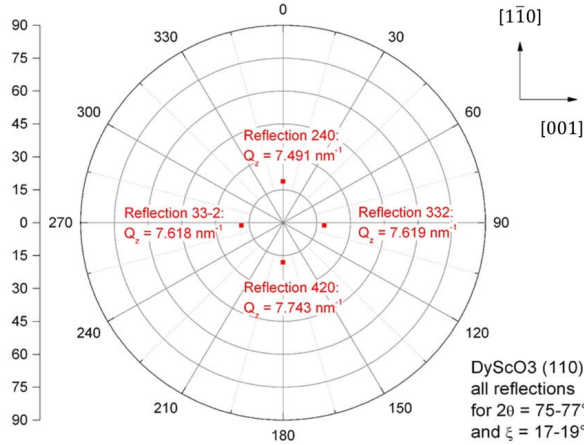


Figure 3-9: Pole figure of a DyScO<sub>3</sub> (110) substrate. The DyScO<sub>3</sub> peaks refer to the (240), (420), (332), and (33-2) reflections. For different reflections (or different directions), these peaks have different  $Q_z$  values. The unambiguous assignment allows to compare the measurement and theoretical calculated values for  $Q_z$ .

To calculate the lattice constant of the films, adequate peak positions of the Bragg reflections of the films are chosen from the RSMs measurements. In order to get a good accuracy of the values, the in-plane lattice constants are achieved by taking the average values for the scans at 0° and 180° and -90° and +90°, respectively. In principle, the reciprocal lattice vectors of the substrate (332) and (33 $\bar{2}$ ) peaks should be identical. However, this is not that case in the reciprocal space maps, because one can never align the sample perfectly. By taking the average values, one obtains a perfect agreement with the nominal values, because it simply averages out the misalignment of the sample. The accuracy of the lattice constants can be obtained from the c lattice constants of all four scan. For each sample, the RSMs are measured in the vicinity of (240), (420), (332), and (33 $\bar{2}$ ) Bragg reflections, as shown in the pole figure. The out-of-plane lattice parameters are calculated by taking the average of  $q_{\perp}$  of the four different reflections directions. The lattice parameters along the in-plane [001] direction are taken from the average value of the (332) and (33 $\bar{2}$ ) reflex, while the lattice parameters of [1 $\bar{1}$ 0] direction are calculated from the average of (240) and (420) reflex.

### 3.2.2 Rutherford backscattering spectrometry

Rutherford backscattering spectrometry (RBS) is a characterization technique that allows to analyze thickness and compositional planar layered systems. A beam of high energy ions (typically

2 MeV He-ions) impinges at a sample. The ions are scattered elastically by the nuclei of the atoms in the sample. The energy of the back scattered ions is analyzed via a detector. On the one hand, the higher the mass of an atom that is hit by an ion, the higher the energy of the scattered ion. On the other hand, the deeper the ion penetrates into the sample before it is scattered, the larger the loss of energy of the ion. The balance between both effects provides a depth profile of the different elements in the examined sample.

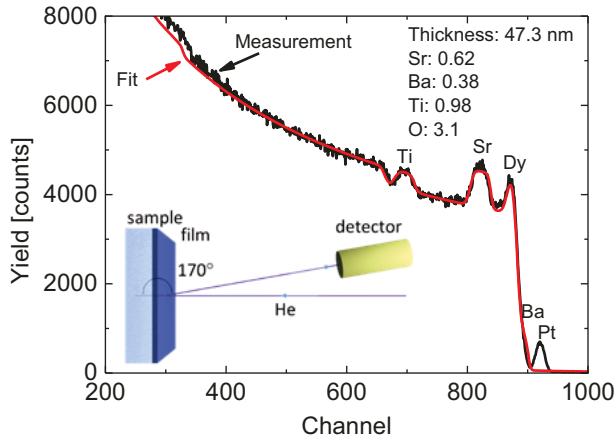


Figure 3-10: Typical RBS data of a  $\text{BaSrTiO}_3$  film (sample number 11158) grown on  $\text{DyScO}_3$  substrate consisting of the experimental data (black line) and the fit (red line). The fit parameters in this case are the thickness of the layer and the composition (see list in the figure) which are in good agreement with the nominal composition of the target of  $\text{Ba}_{0.37}\text{Ti}_{0.63}\text{TiO}_3$ . The insert shows a scheme of a Rutherford backscattering spectrometry geometry.

In this work the RBS measurement is done in FZJ and the data is analyzed with the program RUMP (<http://www.genplot.com/>). Figure 3-10 represents a typical example of a RBS result. The original measured data (black line in Figure 3-10) are analyzed via a fit (red line in Figure 3-10). The parameters used for the fit (RUMP) provide the thickness and stoichiometry of the film.

RBS is especially used to examine the thickness and composition of  $(\text{Ba}_x\text{Sr}_{1-x})\text{TiO}_3$  films with  $0 < x < 1$  (see Figure 3-11). Since Ba and Dy give quite similar peak positions in the RBS results, we use Si-substrates instead of  $\text{DyScO}_3$  for the RBS analysis. Figure 3-11(a) and (b) gives an example of such comparison.

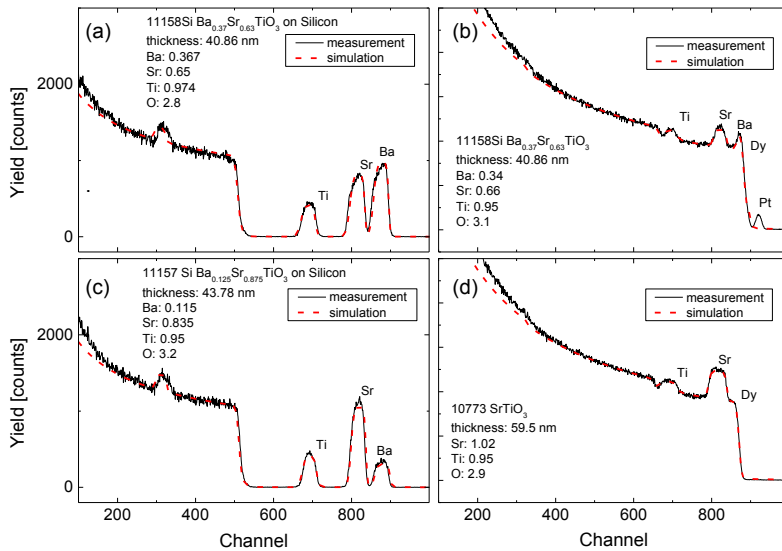


Figure 3-11: RBS results for  $Ba_{0.35}Sr_{0.65}TiO_3$  on (a) a Si-substrate and (b)  $DyScO_3$ ,  $Ba_{0.125}Sr_{0.875}TiO_3$  grown on (c) Si, and (d)  $SrTiO_3$  grown on  $DyScO_3$  substrate.

### 3.2.3 Time-of-flight secondary ion mass spectroscopy

Time-of-flight secondary ion mass spectrometry (ToF-SIMS) is a surface-sensitive analytical method used to obtain a depth profile of the composition of our samples. Figure 3-12 is a sketch of the ToF-SIMS measurement. It uses a pulsed ion beam to remove materials from the surface of the sample. Some of the removed material consists of positive or negative ions, the secondary ions. A mass spectrometer separates the sputtered positive or negative ions according to their mass-to-charge ratio and thus allows the identification of all the chemical elements present. One of the advantages of ToF-SIMS is that it can detect nearly all elements of the material, while the elements with light mass (e.g. K, Na) are difficult for RBS.

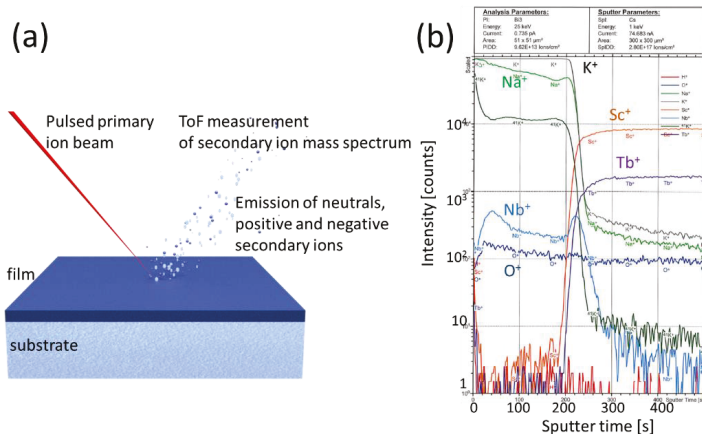


Figure 3-12: (a) Sketch of a ToF-SIMS measurement, (b) depth profiling of a  $K_{0.7}Na_{0.3}NbO_3$  film (sample number 41\_013) grown on  $TbScO_3$ .

In this work the ToF-SIMS is used to analyze the stoichiometry of some of our samples, especially for the  $K_xNa_{1-x}NbO_3$  thin film. From the depth profile one obtains the information on the variation of composition in the film. For instance, Figure 3-12(b) reveals gradual decreasing amount of Na from the surface to the film-substrate interface.

### 3.2.4 Scanning electron microscopes

The “visual” inspection of a sample represents still one of the most important tools to get information and understand problems of the sample and the preparation process. Next to this simple solution, optical microscopy, the scanning electron microscopy (SEM) offers images of the structure and morphology of samples down to nm scale. Moreover, combined with energy dispersive X-ray (EDX) one can obtain local information on elements in and on the sample. SEM uses a focused beam of high-energy electrons to generate signals at the surface of samples. The surface texture, chemical composition, and crystalline structure affect the electron-sample interactions and reveal a variety of signals. These signals include secondary electrons, which produce SEM images on the morphology and topography on samples. Furthermore, backscattered electrons are used to illustrate contrasts in composition in multiphase samples. Finally, due to the inelastic collisions of the incident electrons with electrons in discrete orbitals of atoms in the samples, X-rays could be produced for each element in a sample that is excited by the electron beam. Since each element has its own atomic structure that allows a unique set of peaks on its electromagnetic emission spectrum. This provides the possibility for the elemental analysis of samples, i.e. EDX.

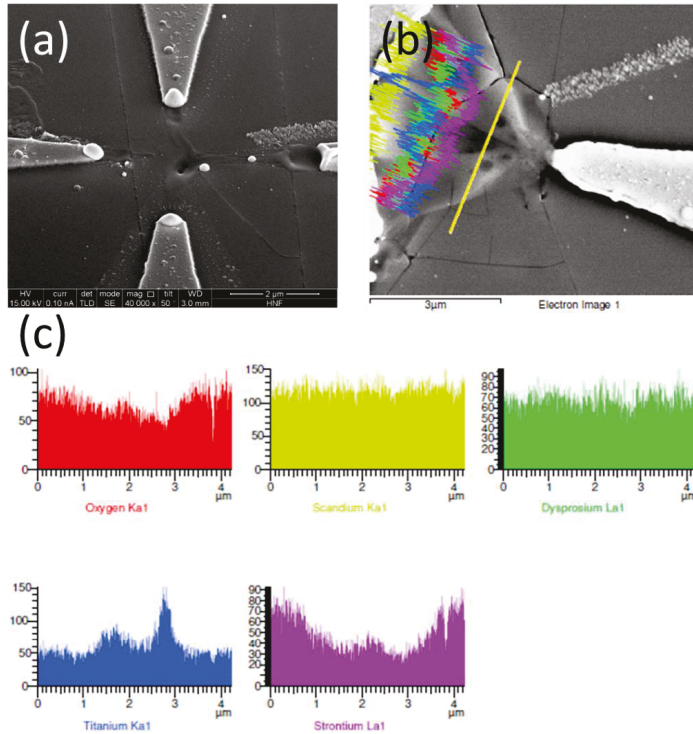


Figure 3-13: SEM images of 90 nm strained SrTiO<sub>3</sub> film (sample number 12187) grown on DyScO<sub>3</sub> substrate (a) with cross-like arranged electrodes. The image shows among others that the electrodes are partially melted after applying a 10 μA current. (b) Structure on the same SrTiO<sub>3</sub> film with cracks near a sharp planar electrode. The cracks appeared after high electric field application. The line marks the EDX measurement range and (c) shows the resulting EDX pattern for each element O, Sc, Dy, Ti, and Sr.

In this work a Gemini 1550 (Zeiss) is used for the characterization of films and samples especially after patterning. Furthermore, EDX is used in order to visualize migration and removal of elements in the SrTiO<sub>3</sub> film after applying large electronic current in these “nominal” isolators. Figure 3-13 shows an example of SEM picture of SrTiO<sub>3</sub> film with electrodes measured at HNF. The cross-like area in the middle and the tip electrodes are partially melted due to the heating effect during application of large currents during the electric characterization. Furthermore, a few cracks can be seen in the film. Because the conductivity of the film is typically not sufficiently large for SEM, a 10 nm conducting carbon layer is deposited before SEM measurement. The additional carbon layer will affect the electric characterization of the films. Thus most of the SEM pictures are taken after the electric characterization in this work.

### 3.2.5 Atomic force microscopy

Atomic force microscopy (AFM) offers an even higher resolution compared to SEM. Its work principle is based on a sharp tip (cantilever) that scans over the examined surface. Using a dedicated feedback loop the interaction or distance between the tip and the surface is controlled. The feedback parameters are then used to construct an image of the topography of the surface. Normally AFM involves a laser deflection to control the force and tip position for a feedback loop. As shown in Figure 3-14, a laser is reflected from the backside of the cantilever. A photodetector is used to monitor the laser beam, the electronic produces the feedback signal. It is worth to note that the AFM does not require a conducting sample because it uses the atomic forces to map the tip-sample interaction.

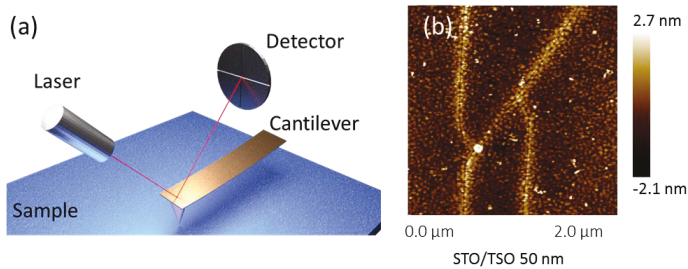


Figure 3-14: (a) Schematic sketch of an AFM and (b) example of an AFM image ( $10 \times 10 \mu\text{m}^2$ ) of a 50 nm thick  $\text{SrTiO}_3$  film (sample number 11916) grown on a  $\text{TbScO}_3$  substrate.

Typically surface roughness and cracks of our oxide films are characterized in this work. Figure 3-14(b) shows an example of AFM image on a 90 nm thick  $\text{SrTiO}_3$  film on  $\text{TbScO}_3$ . The bright lines are indications of cracks in the biaxial tensely strained film.

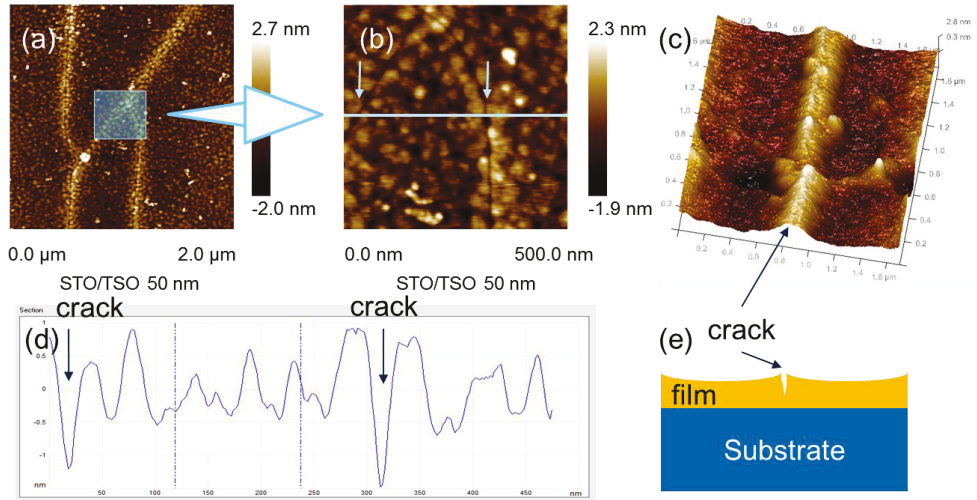


Figure 3-15: AFM images (a-c) of 50 nm thick SrTiO<sub>3</sub> film on TbScO<sub>3</sub> substrate. (d) Height profile from a cross section, marked as a straight line in (b), the two cracks are marked with arrows in both (b) and (d). (e) Sketch of the crack in the sample.

In order to learn more about the cracks, a smaller range (here 500 nm × 500 nm) is chosen for the AFM image. Figure 3-15 shows the resulting image of the cracks. It can be seen that there is a gap in the elevated stripes. Figure 3-15(e) gives a sketch that explains the stripe structure of the AFM image.

### 3.3 Device preparation and characterization

Most important for this work was the electronic characterization of the oxide films. Several electrical properties are characterized, e.g. permittivity, piezoelectric effect, and conductivity. Since we concentrate on the temperature dependence of these properties, most of the measurements are done in cryostats (CF1200). The sample is top-loaded through an access port on top of the cryostat. It is cooled by via liquid Helium and heated with the self-made heater underneath of the sample. This way temperatures ranging from 4 K to 500 K could be established without changing the system or breaking the vacuum. Several electronic measurement devices are connected to the sample to monitor the different parameters of the sample. A temperature controller (Lakeshore 332) is used to control the temperature, a LCR meter (Sourcetric, ST2826A, or ST2826) is used to measure the capacitance of the film, a high frequency signal generator (Hewlett Packard, E4422B, ESG series signal generator, 250 kHz ~ 4.0 GHz) is used to generate SAWs, a spectrum analyzer (Anritsu, MS2661C, 9 kHz ~ 3 GHz) is used to detected the

SAW signal, a sourcemeter (Keithley 2835B) is used as current or voltage source, and a nanovoltmeter (Keithley 182) is used as a highly sensitive voltmeter. All measurement devices are controlled and the data are collected via a computer using LabVIEW programs.

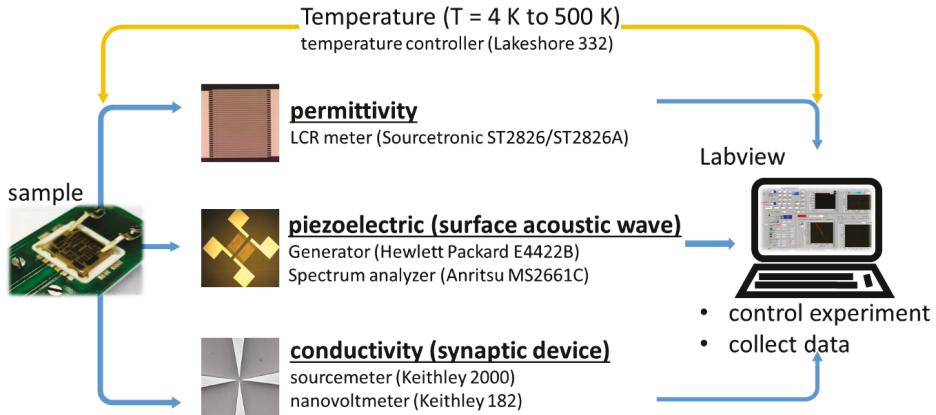


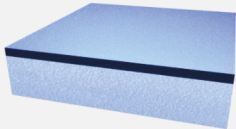
Figure 3-16: Sketch of the experimental setup and techniques introduced this chapter.

### 3.3.1 Electrodes fabrication

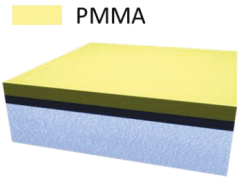
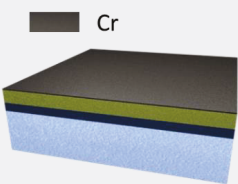
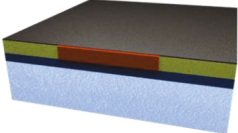
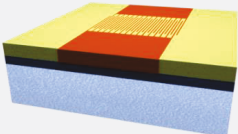
In order to study the electronic properties (permittivity, piezoelectricity, and conductivity) of the samples, the metal electrodes with reasonable design have to be prepared the films. The following part will describe the preparation techniques that was used for the preparation of these electrodes.

After the oxide films deposition, all electrodes of devices are prepared via e-beam lithography<sup>3</sup> and lift-off technology in FZJ. The specific lift-off process steps are as following:

Table 3-1: Summary of lithography and lift-off technique and key parameters for each step.

Step	Process	Description	Sketch
1	Cleaning	Chemical cleaning in acetone (5 minutes) followed by isopropanol (5 minutes). Both steps in an ultrasonic bath at 100% (320W), 37 kHz and room temperature. Finally, drying with nitrogen gas.	

<sup>3</sup> In cooperation of the author with Dr. Stefan Trelenkamp

Step	Process	Description	Sketch
2	Photoresist coating	<p>The photoresist, poly(methyl-methacrylate) (PMMA, in this work PMMA 649.04 950K, from company All resist is used), is spin-coated at first 1000 rotations per minute (rpm) for 5 s followed by 4000 rpm for 60 s.</p> <p>After spin-coating, samples are immediately baked on a hot plate at 180°C for 30 minutes. The typical thickness of the PMMA layer is 800 nm in this work.</p>	 <p>PMMA</p>
3	Cr deposition	<p>The conductivity of the samples in this work is too low for the following electron-beam lithography. Thus a 10 nm chrome layer is required on top of the PMMA layer. It is deposited via evaporation deposition (Balzers PLS 500).</p>	 <p>Cr</p>
4	E-beam exposure	<p>The sample with the electron-sensitive photoresist (PMMA) is ready for the e-beam lithography. An e-beam writer (VISTEC EBPG 5000 plus) based on a field-emission source is used in this work. The patterns are designed with AutoCAD. Typical e-beam doses are 300 <math>\mu\text{C}/\text{cm}^2</math> in this work.</p>	 <p>exposed PMMA</p>
5	Cr etching	<p>The 10 nm Cr top layer needs to be removed firstly. The etchant is a mixture of ceric ammonium nitrate <math>((\text{NH}_4)_2[\text{Ce}(\text{NO}_3)_6])</math>, perchloric acid (<math>\text{HClO}_4</math>) and deionized water by a ratio of 10.9 : 4.25 : 84.85 (MicroChemicals). Leading to a Cr etching rate of 80 nm/min. In this work the samples are left in the etchant for 12 s to ensure a complete Cr layer is removal. After etching, the sample is rinsed in deionized water for 60 s and dried with nitrogen gas.</p>	

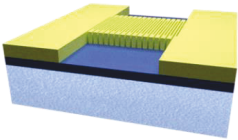
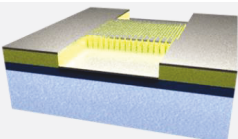
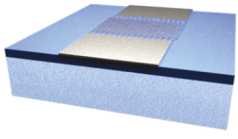
Step	Process	Description	Sketch
6	Development	The exposed photoresist is removed by a developing solvent (AR-600-55, methyl-isobutyl-ketone (MIBK) from Allresist) for 105s. After that, the sample is rinsed in isopropanol for 1 min to wash away the developing solvent and dried with nitrogen gas.	
7	Electrodes deposition	Metallic layers are deposited via thermal evaporation (electron beam). In most cases a 5 nm Ti layer is first deposited (adhesion layer) followed by a Pt layer with a thickness ranging from 15 nm to 100 nm (depending on the application). Alternatively, samples are deposited only with Pt layer via d.c. magnetron sputtering (Leybold Z400S).	
8	Lift-off	Finally the photoresist layer (including the metal layer on it) is washed away using acetone for 30 min. Followed by an ultrasonic bath at room temperature with moderate power for 1 min to make sure all resistor is removed. Finally, the sample is dried by nitrogen gas.	

Table 3-1 summarizes the electrodes patterning process. Most steps are more or less standard. However, they have to be optimized for the given system. One unusual step has been added. A typically 10 nm thick Cr layer is deposited on the PMMA layer (step 3) in order to ensure a sufficient conductance of the system for the e-beam exposure. Since this Cr layer is thin, the high-energy electrons can pass through the layer with only little scattering. After the e-beam exposure, the Cr layer is removed by the etching solvent (step 5). This will not affect the surface of sample, because the 800 nm thick PMMA layer is covering the surface during all the previous processes. In the end, the electrode material is deposited either via evaporation or d.c. magnetron sputtering.

### 3.3.2 Temperature control

One of the most important parameters in the electronic characterization is the temperature. Basically it consists of 3 parts:

- (i) Cooling is provided by liquid He. A manually up- and downstream controlled He flow ensures a continuous cooling of the sample.

- (ii) Heating is provided by a self-made planar resistive heater which is placed directly below the sample.
- (iii) Finally there are the temperature sensors. We work with 3 different sensors:
  - The cryostat is equipped with an AuFe/Chromel thermocouple (actually with a heater) that allows to measure the temperature at the bottom of the inset of the cryostat.
  - Additionally we placed a second commercial sensor (Cernox<sup>®</sup>) in the sample holder.
  - However, in order to obtain the temperature at the film itself we developed an integrated thin-film resistive sensor made from the same material as the electrodes, i.e. Pt. this Pt sensor is calibrated using the Cernox<sup>®</sup> sensor and allows a precise determination of the sample temperature.

Figure 3-17 shows the cryogenic measurement setup. In combination with the Lake Shore temperature controller (PID controle) we can stabilize any temperature within the range of 5 K to 500 K within the cryostat. In the following sections we will describe the different sensors, especially the self-made heater and Pt-sensor, and starting with the sample holder.

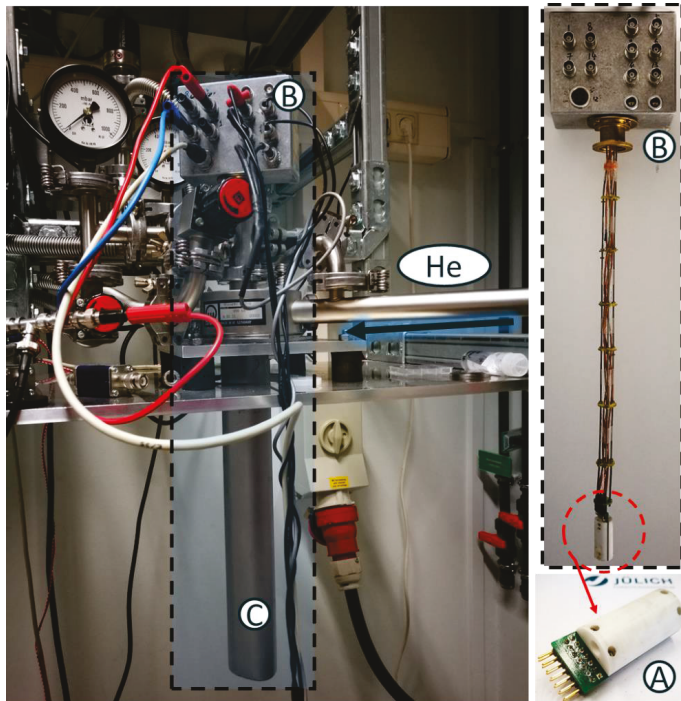


Figure 3-17: Images of a sample carrier (A), which is plugged to a holder (B), and then inserted into the cryostat (C).

A completely setup of the sample carrier is shown in Figure 3-18. Part ① is the electronic circuit board designed with 14 lines for the electric characterization. The ceramic parts ② and ③ serve as electronic and thermal shields, they are fixed with screws ④. The resistive Pt heater ⑥ is fixed by one of the ceramic shields ② and connect to two pins of the circuit board ① for the current supply (heating). The sample ⑦ with electrodes and Pt-sensor is placed onto the Pt film heater ⑥ and fixed with two clamps ⑤.

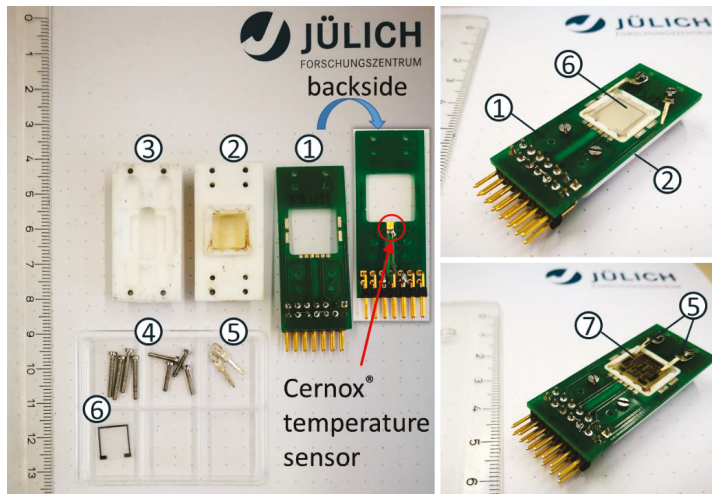


Figure 3-18: Illustrations of sample carrier. ① circuit board ② ceramic bottom ③ ceramic cap ④ screws ⑤ clamps ⑥ Pt film heater ⑦ sample.

The self-made Pt heater and Pt temperature sensor are prepared via lithography and lift-off technology on sapphire or simultaneous with all other electrodes, respectively (see Figure 3-19)

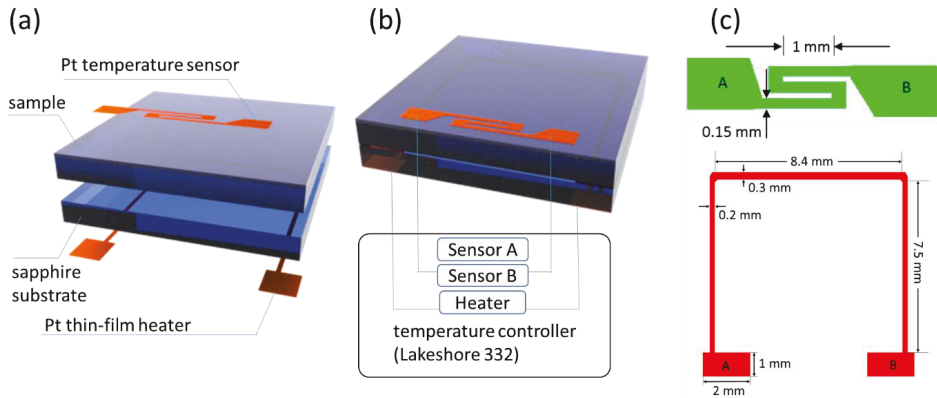


Figure 3-19: Sketch (a, b) and design (c) of the Pt thin-film temperature sensor and Pt thin-film heater on separate substrates. (note the size is not to scale)

The commercial temperature sensor (Cernox<sup>®</sup>) on the sample carrier is mounted about 2 mm away from the edge of the sample (see Figure 3-20). Before measurement, the Cernox<sup>®</sup> sensor is calibrated at room temperature and liquid nitrogen temperature. Due to the relatively homogenous temperature distribution in the cryostat, this sensor works quit well below room temperature. However, the integrated sensor is better, especially at elevated temperatures.

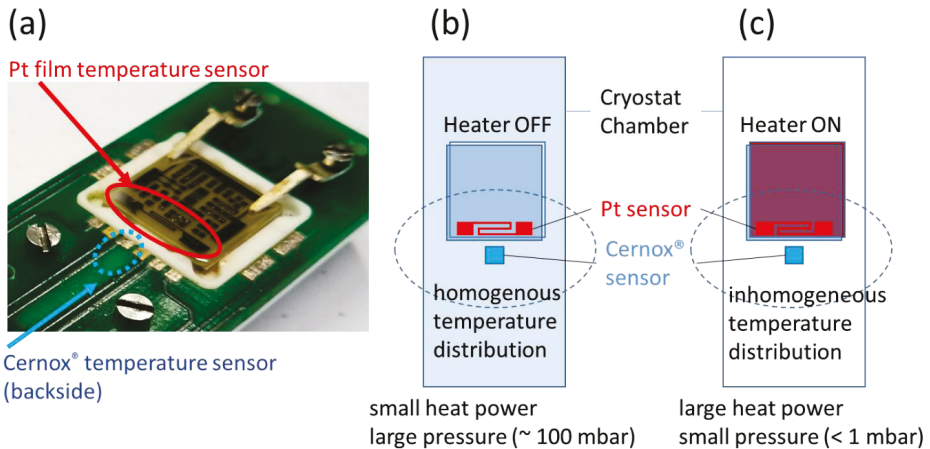


Figure 3-20: (a) Image of the integrated Pt thin-film temperature sensor and Cernox<sup>®</sup> temperature sensor on the sample carrier. Work principle of temperature control for (b) small heater power and large He pressure (typically > 100 mbar) at low temperature and (c) large heater power and small He pressure (< 1 mbar) for high temperature.

Prior to its use, the Pt temperature sensor has to be annealed and calibrated. Annealing: the Pt sensor was annealed in vacuum ( $< 1$  mbar) at  $T_{annealing} \cong 500$  K for 3 min. The sheet resistance of the Pt structure normally reduces to 80% of the original value. The resulting resistance of the Pt sensor depends on the thickness of the Pt layer (Figure 3-21). After the annealing process, the dependence between resistance and temperature of Pt temperature sensor becomes stable in all measurement process for  $T < T_{annealing}$ .

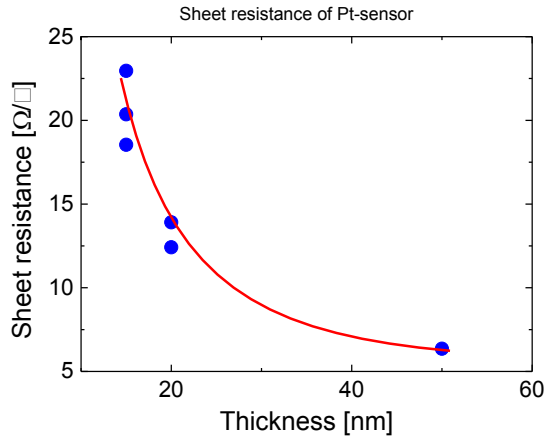


Figure 3-21: Sheet resistance of the Pt temperature sensors with various film thickness, the curve is a guide for the eye.

Calibration: in a second step the Pt-sensor is calibrated by measuring its resistance  $R_i$  at two different temperatures  $T_i$ , where  $i$  refers to the temperature. This is typically done by measuring at room temperature and a low temperature (e.g. 200 K) using the reading from the Cernox<sup>®</sup> sensor. The resulting calibration is given by:

$$T_{Pt} = a + bR_{Pt} \quad (3-2)$$

where  $b = \frac{T_1 - T_2}{R_1 - R_2}$ ,  $a = T_1 - \left(\frac{T_1 - T_2}{R_1 - R_2}\right) R_1$ , and  $T_{Pt}$  and  $R_{Pt}$  is the temperature and resistance of the Pt sensor, respectively.

In order to examine the linear dependence between resistance and temperature, the sample is heated using the Pt heater while recording its resistance and the temperature of the sample using a thermocouple. The measured data and the linear fit (dashed line) agree quite well (see Figure 3-22). This demonstrates our Pt thin-film temperature sensor works very well above room temperature.

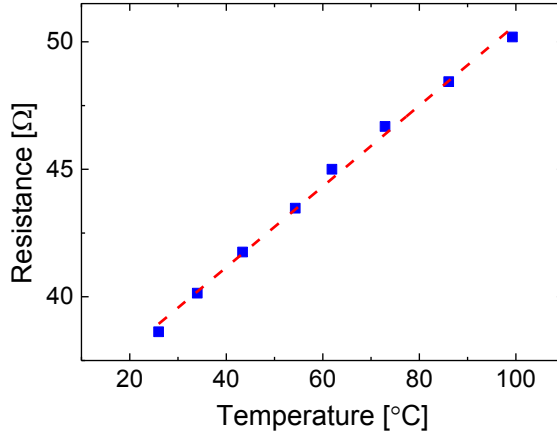


Figure 3-22: Linear dependence between temperature and resistance of an 80 nm Pt film temperature sensor.

The significant characteristic of metals used as resistive temperature sensor is their linear temperature dependence  $\alpha = \frac{dR}{dT \cdot R_{RT}}$  at elevated temperatures. The temperature coefficient  $\alpha$  is an intrinsic characteristic of the material. In our Pt thin films  $\alpha$  differs slightly from that of pure platinum since our temperature sensor consists of a combination of Ti and Pt and it most likely contains a large number of defects. Table 3-2 gives examples of the specific resistance at room temperature and the temperature coefficient  $\alpha$  for different samples.

Table 3-2: Specific resistances  $\rho_{RT}$  and temperature coefficient  $\alpha$  at room temperature measured for various Pt temperature sensor.

Sample Name	Film	Substrate	Thickness of film sensor	$\rho_{RT}$ ( $\Omega\text{m}$ ) ( $\times 10^{-7}$ )	$\alpha$ ( $\text{K}^{-1}$ )
STOref-1	-	SrTiO <sub>3</sub>	5nm Ti/ 15 nm Pt	3.29	0.00163
11269	SrTiO <sub>3</sub>	GdScO <sub>3</sub>	5nm Ti/ 15 nm Pt	3.48	0.00165
11268	SrTiO <sub>3</sub>	TbScO <sub>3</sub>	5nm Ti/ 15 nm Pt	2.68	0.00194

Sample Name	Film	Substrate	Thickness of film sensor	$\rho_{RT}$ ( $\Omega\text{m}$ ) ( $\times 10^{-7}$ )	$\alpha$ ( $\text{K}^{-1}$ )
10772	SrTiO <sub>3</sub>	DyScO <sub>3</sub>	5nm Ti/ 20 nm Pt	2.49	0.00232
TSOref	-	TbScO <sub>3</sub>	5nm Ti/ 20 nm Pt	2.94	0.00185
12189	SrTiO <sub>3</sub>	DyScO <sub>3</sub>	5nm Ti/ 50 nm Pt	2.52	0.00297
12190	SrTiO <sub>3</sub>	DyScO <sub>3</sub>	5nm Ti/ 50 nm Pt	2.73	0.00287

Figure 3-23 shows  $\alpha$  as function of the thickness of the Pt layer. With increasing Pt thickness, i.e. increasing amount of Pt in the temperature sensor,  $\alpha$  is getting closer to the literature value of pure platinum.

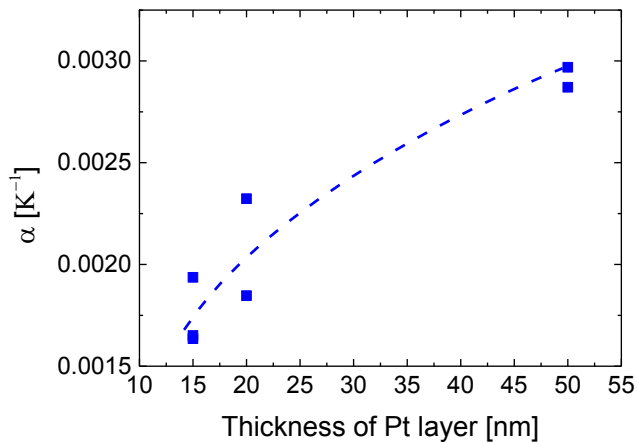


Figure 3-23: Temperature coefficient  $\alpha$  as a function of the thickness of the Pt film of various temperature sensors. The thickness of the Ti layer is always 5 nm.

### 3.3.3 Permittivity measurement

In this work we focus on mainly three electronic properties of our strained oxide films, i.e. the permittivity, piezoelectricity (in form of SAW measurements), and the conductivity. Let us start with the permittivity measurement. For the analysis of the in-plane dielectric properties of the

films, interdigitated electrodes (IDEs) are prepared on top of the film using e-beam lithography and a lift-off technique as described before.

In order to simplify the analyze process, all IDEs prepared for permittivity measurement are identical in this work. The design of the IDE is shown in Figure 3-24.

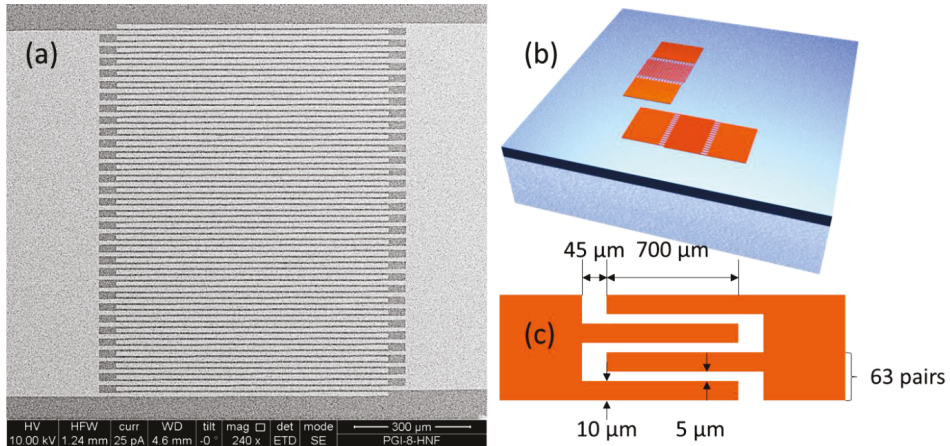


Figure 3-24: (a) Scanning electron microscopy picture of a pair of IDEs. (b) Sketch of IDEs, oriented in two perpendicular directions (typically along the 2 major crystallographic orientations of the substrate and, thus, film). (c) Illustration of the finger (digit) structure of the IDE (not to scale) with size annotations.

Figure 3-24(a) shows an SEM picture of an IDE. In order to analyze different in-plane directions of the permittivity, two IDEs oriented in two perpendicular directions are prepared on each sample. The interdigitated structure consists of 64 “fingers”. In order to simplify the data analysis, a relatively large gap of 5 μm is chosen in combination with a large effective length of the capacitor length of  $63 \times 700 \mu\text{m} = 44.1 \text{ mm}$ . (i) The first allows the use of the partial capacitive model, and (ii) the latter leads to a sufficient resolution of the capacitive measurement. In order to avoid stray fields, the gap is strongly extended to 45 μm at the end of each finger. The two electrodes of the IDE are bonded to the sample carrier and measured by a LCR meter (ST2826A). In the end the permittivity is evaluated from the measurement result using the “partial capacitance model”. [60]

The “partial capacitance model” is based on:

- (i) dividing the total capacitance into individual contributions (see Figure 3-25) and,
- (ii) using elliptical integrals or conformal mapping to describe the different contributions.

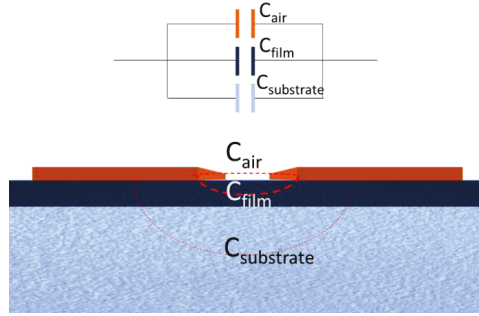


Figure 3-25: Sketch of the electric field distribution from the side view, and the equivalent electric circuit.

In our case, the measured capacitance can be divided into four partial capacitances (see Figure 3-25):

$$C_{total} = C_{air} + C_{film} + C_{substrate} + C_{setup} \quad (3-3)$$

where  $C_{air}$ ,  $C_{film}$ ,  $C_{substrate}$ , and  $C_{setup}$  are the capacitance of the ambient space (air), the film, the substrate, and the measurement setup (e.g. cables), respectively. By taking a reference measurement of an identical system but without the film:

$$C_{reference} = C_{air} + C_{substrate} + C_{setup}, \quad (3-4)$$

the capacitance of the film is simply:

$$C_{film} = C_{total} - C_{reference}. \quad (3-5)$$

In order to easily obtain the dielectric properties, the permittivity has to be calculated. The different contributions to the capacitance are:

$$C_{air} = w \cdot \varepsilon_0 \frac{2}{\pi} \ln \left( 4 \frac{l}{s} \right), \quad (3-6)$$

$$C_{film} = \frac{w \cdot \varepsilon_0 (\varepsilon_2 - \varepsilon_3)}{\frac{s}{t_2} + \left( \frac{4}{\pi} \right) \ln 2}, \text{ and} \quad (3-7)$$

$$C_{substrate} = w \cdot \varepsilon_0 (\varepsilon_3 - 1) \frac{1}{\pi} \ln \left( 16 \frac{t_3 - t_2}{\pi s} \right), \quad (3-8)$$

where  $w$  is the width of the planar capacitor,  $l$  is the length of the capacitor from one electrode to another one,  $s$  is the gap of the capacitor,  $t_1$ ,  $t_2$ , and  $t_3$  is the thickness of electrode, film, and substrate, respectively,  $\varepsilon_0$  is the permittivity of free space, and  $\varepsilon_1$ ,  $\varepsilon_2$ ,  $\varepsilon_3$  is the dielectric constant of the air, film and substrate, respectively (see Figure 3-26).

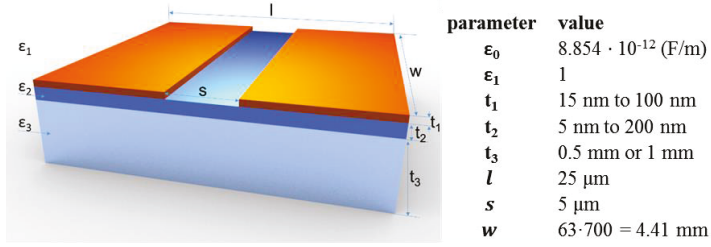


Figure 3-26: A planar capacitor consisting of an insulating substrate, a thin film with a large dielectric constant and conducting electrodes and value used in our work.

It should be noted that the conformal mapping used here is restricted to certain size conditions:

- (i)  $s \leq 2w/3$
- (ii)  $s \geq h$

According to the parameters of IDE in Figure 3-26, our design vouchsafes the applicability of the method. In our case the permittivity and  $\tan\delta$  can be written as:

$$\epsilon_{film} = \frac{(C_{total} - C_{reference}) \times \left( \frac{5 \cdot 10^{-6}}{t_2} + 0.883 \right)}{3.90 \times 10^{-13}} \quad (3-9)$$

$$\tan \delta_{film} = \frac{\tan \delta_{total} \cdot C_{total} - \tan \delta_{reference} \cdot C_{reference}}{C_{total} - C_{reference}} \quad (3-10)$$

here  $C_{total}$  and  $\tan \delta_{total}$  are the measured capacitance and losses for our sample and  $C_{reference}$  and  $\tan \delta_{reference}$  are the measured capacitance and losses for the corresponding substrate, respectively, and  $t_2$  is the film thickness in nm.

In order to calculate the permittivity of film, the capacitance of the pure substrate needs to be known. Moreover, in most cases the permittivity of the substrate also depends on the orientation of the applied electric field. Thus IDEs have to be deposited on the substrates to measure the value of  $C_{reference}$  and  $\tan \delta_{reference}$  as a function of field orientation and temperature. There are mainly three types of substrate involved in this work: (110)DyScO<sub>3</sub>, (110)TbScO<sub>3</sub>, and (110)GdScO<sub>3</sub>. All these three types of substrate are (110) cut scandates. Their in-plane orientation are recorded via XRD and marked by cuts of two corners indicating the two orientations [ $\bar{1}\bar{1}0$ ] and [001] (see Figure 3-27).

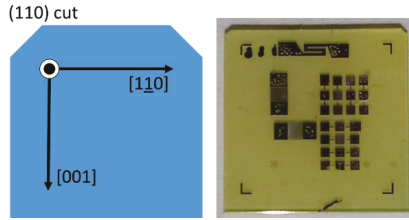


Figure 3-27: Sketch and image (sample number 11689) of a substrate (top view) showing the cut corners that indicate the crystallographic orientation.

The reference values  $C_{reference}$  and  $\tan \delta_{reference}$  are measured on each type of substrate for both directions (electric field parallel to  $[001]$  and  $[1\bar{1}0]$ ) in the temperature range from 5 K to 400 K at a frequency of 100 kHz and amplitude of the ac field of 0.25 V. Since all substrates show no visible frequency or voltage dependence, the reference data can be used for the calibration of all experiments in this work.

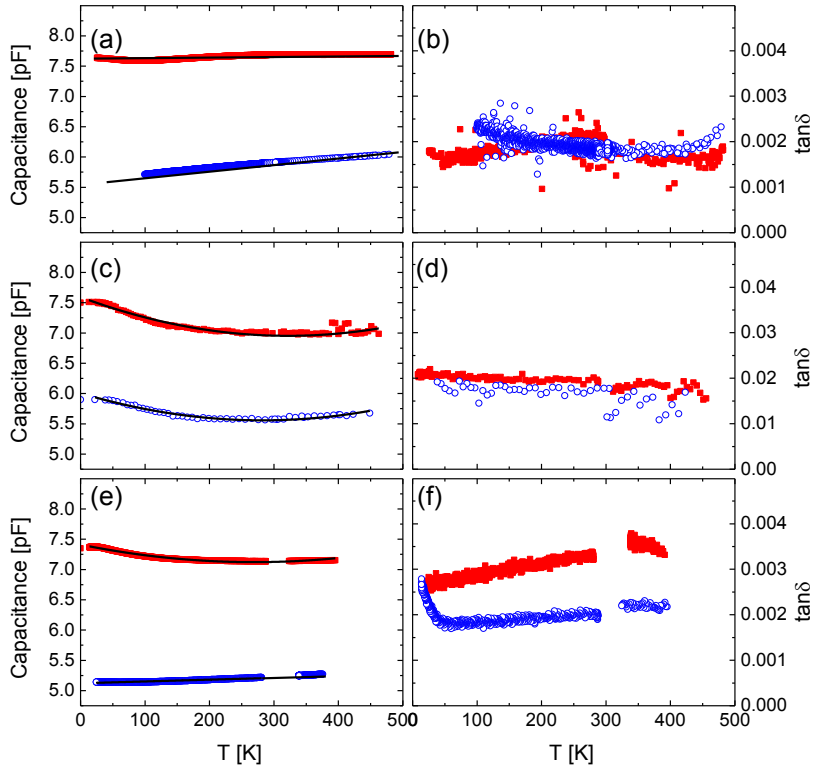


Figure 3-28: Capacitance and  $\tan\delta$  as a function of temperature for (a, b)  $(110)\text{DyScO}_3$ , (c, d)  $(110)\text{TbScO}_3$ , and (e, f)  $(110)\text{GdScO}_3$  substrates along  $[001]$  direction (red square) and  $[\bar{1}\bar{1}0]$  direction (blue open circle). The fits are given as the black lines in each capacitance plot.

Figure 3-28 shows the measured reference values  $C_{\text{reference}}$  and  $\tan\delta_{\text{reference}}$  as function of the temperature for all three types of substrates. Generally, the capacitance along the  $[001]$  orientation (red squares) is larger than that along the  $[\bar{1}\bar{1}0]$  orientation (blue open circles). For each direction the change of capacitance shows a slightly temperature dependence. The capacitance  $C_{\text{reference}}$  can be approximated by a polynomial fit:

$$C_{reference} = a + bT + cT^2 \quad (3-11)$$

with coefficients given in Table 3-3 for each type of substrate. The change of  $\tan\delta$  (losses of the substrate and the setup), is relatively small in the measured temperature range. Therefore we assume a constant loss  $\tan\delta$ . The fits of  $C_{reference}$  and  $\tan\delta_{reference}$  are used to calculate the permittivity and loss of the corresponding samples in this work.

Table 3-3: Fit parameters from the capacitance measurements  $C_{reference}$  and the approximate  $\tan\delta_{reference}$  value for the different substrates  $DyScO_3$ ,  $TbScO_3$ , and  $GdScO_3$ .

Substrate		$C_{reference} = a + bT + cT^2$ (pF)			$\tan\delta_{reference}$
		$a$	$b$	$c$	
<b>DyScO<sub>3</sub></b>	[001] 	7.1089	$1.8178 \cdot 10^{-4}$	0	0.001 ~ 0.003
	[1 $\bar{1}$ 0] 	5.2319	$9.2438 \cdot 10^{-4}$	0	0.001 ~ 0.003
<b>TbScO<sub>3</sub></b>	[001] 	7.59392	-0.00398	$6.17913 \cdot 10^{-6}$	0.01 ~ 0.02
	[1 $\bar{1}$ 0] 	6.00652	-0.00318	$5.64265 \cdot 10^{-6}$	0.01 ~ 0.02
<b>GdScO<sub>3</sub></b>	[001] 	7.4117	-0.00215	$3.99985 \cdot 10^{-6}$	0.002 ~ 0.004
	[1 $\bar{1}$ 0] 	5.12146	$2.97406 \cdot 10^{-4}$	0	0.001 ~ 0.003

### 3.3.4 Polarization measurement

In order to analyze the polarization of the strained films, the polarization is measured using a classic Sawyer-Tower circuit (see Figure 3-29):

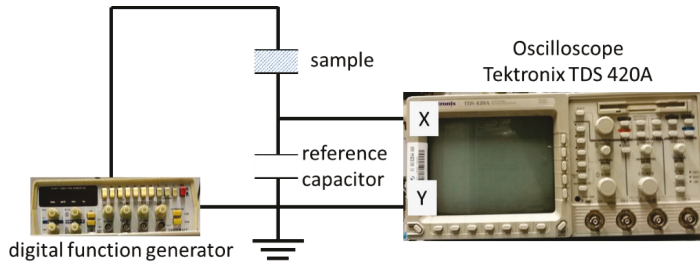


Figure 3-29: Sketch of a Sawyer-Tower circuit used in this work.

In this experiment, the signal generator provides the sweep voltage at high frequency, the resulting voltage across the reference capacitor is measured. Since the charge at the capacitor is identical to the charge of the ferroelectric sample, we obtain:

$$Q = C \cdot V \tag{3-12}$$

where  $C$  is the capacitance of the reference capacitor, and  $V$  is the voltage measured at capacitor. As a result, the polarization is:

$$P = Q/A \tag{3-13}$$

where the  $A$  represents the “effective area” of the capacitors. The capacitance of the reference capacitor should be much larger than the capacitance of the sample, thus most of the voltage is applied at the sample. In the measurement the reference capacitor is typically 47 pF.

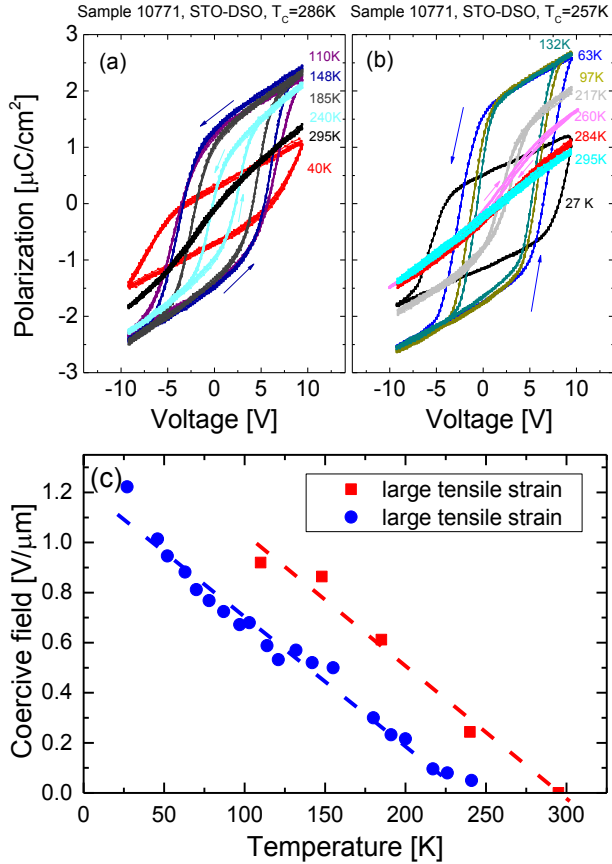


Figure 3-30: Typical polarization hysteresis measured by a Sawyer-Tower circuit on our strained SrTiO<sub>3</sub> film for electric field oriented along (a) the large and (b) the small in-plane tensile strain direction. (c) The coercive field extracted from the polarization hysteresis as function of temperature.

Figure 3-30 shows the hysteresis loops for a 40 nm thick SrTiO<sub>3</sub> film on a DyScO<sub>3</sub> (sample number 10771) for large tensile strain and small tensile strain (Figure 3-30b) at various temperatures and the resulting coercive field as a function of temperature. The results demonstrate that the strained film represents typical ferroelectric polarization hysteresis below a phase

transition temperature in both in-plane directions. The larger coercive field in the larger tensile strain orientation indicates the larger polarization compared to the smaller tensile strain direction at the same temperature. The different  $T_C$  values obtained from Figure 3-30(c) are 236 K and 296 K for the small and large strain direction, respectively.

### 3.3.5 SAW measurement

SAW devices are employed (i) to analyze the piezoelectric effect and (ii) the SAW properties in our strained films, and (iii) to check our films for possible sensor applications (e.g. mass detection or biosensors). The SAW experiments are also based on IDE structures on our film. However, this time we need two IDEs, one serves as a generator of SAWs (input) and the second one is the receiver (output), see Figure 3-31. The SAW generating IDE is connected to a high frequency signal generator (Hewlett Packard, E4422B, ESG series signal generator, 250 kHz ~ 4.0 GHz). The receiver IDE is connected to a spectrum analyzer (Anritsu, MS2661C, 9 kHz ~ 3 GHz), see Figure 3-31. Figure 3-31(a, b) show an example of a pair of IDEs. In this case “finger” width and the gap size are 5  $\mu\text{m}$  which results in a wavelength of 20  $\mu\text{m}$  for the SAW. In this work the wavelength and propagation distance (distance between input and output) are varied in order to find an optimum SAW response.

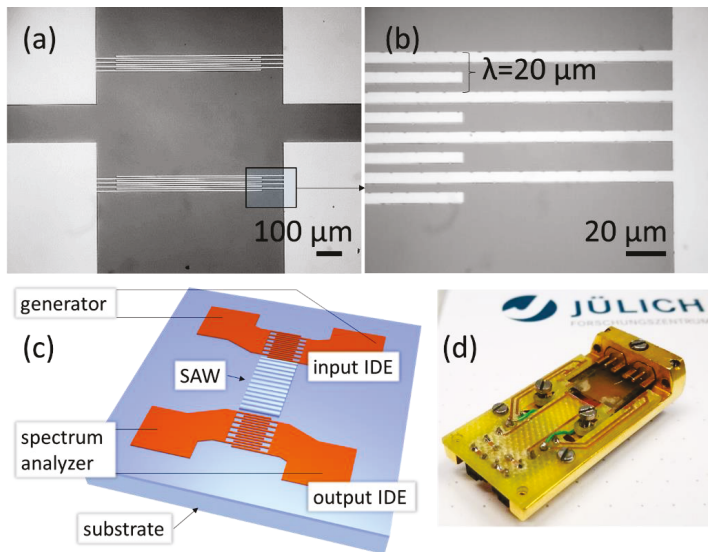


Figure 3-31: (a, b) Microscopic images of a pair of IDEs (SAW input and output) for a wavelength of 20  $\mu\text{m}$ , (c) Sketch of the measurement setup, and (d) sample carrier for the cryogenic SAW measurements.

In this work the IDEs is analyzed in a 2-port network. Where S-parameters describe the input-output relationship between the two ports.

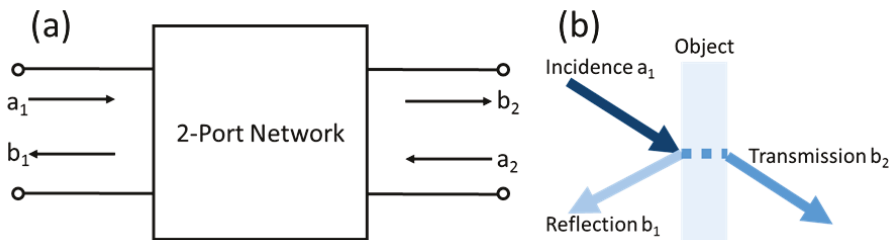


Figure 3-32: (a) Sketches of a 2-port network and (b) the transmission parameters.

Figure 3-32(a) shows a sketch of a 2-port network.  $|a_1|^2$  represents the incident power on port 1,  $|b_1|^2$  the reflected power from port 1, whereas  $|a_2|^2$  is the incident power on port 2, and  $|b_2|^2$  the reflected power from port 2. The transmission matrix relates these four waves in the following way:

$$\begin{bmatrix} b_1 \\ b_2 \end{bmatrix} = \begin{bmatrix} S_{11} & S_{12} \\ S_{21} & S_{22} \end{bmatrix} \begin{bmatrix} a_1 \\ a_2 \end{bmatrix} \quad (3-14)$$

where  $S_{11}$  is the input reflection coefficient of the network ( $S_{11}=b_1/a_1$ , return loss),  $S_{21}$  is the forward transmission coefficient through the network ( $S_{21}=b_2/a_1$ , insert loss),  $S_{22}$  is the output reflection coefficient, and  $S_{12}$  is the reverse transmission coefficient. Typically  $S_{21}$  is used to characterize the transport of the SAW on the samples. Although the  $S_{21}$  is not directly connected to the piezoelectric coefficient or coupling coefficients, the piezoelectric effect is the major reason of SAW signal.

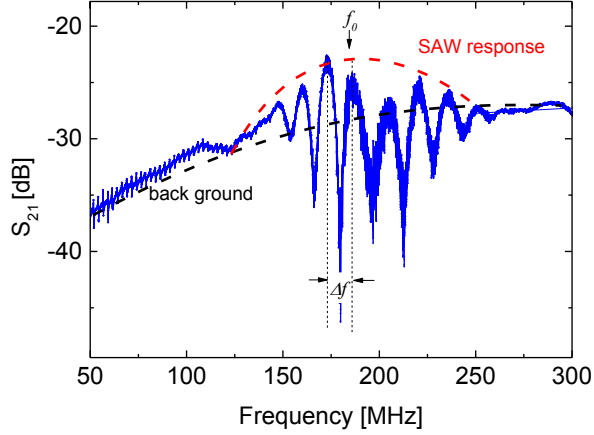


Figure 3-33: Measured SAW response as a function of frequency on a  $(K_{0.7}Na_{0.3})NbO_3$  film (sample number 41\_013).

Figure 3-33 shows a typical  $S_{21}$  (loss) spectrum obtained for SAW measurements. The measurements are usually performed with a power of  $1 \text{ mW} = 0 \text{ dBm}$ . The resulting unit is dB relative to  $1 \text{ mW}$  of power. The general reduction of the signal of approx.  $-30 \text{ dB}$  is caused by losses in the setup (microwave cables and esp. the bond wires). However, the oscillations observed in the frequency range from  $\sim 150 \text{ MHz}$  to  $\sim 250 \text{ MHz}$  are clear indications from the SAWs. Using:

$$v = \lambda \cdot f_0, \text{ or} \quad (3-15)$$

$$\Delta f = v/L \quad (3-16)$$

where  $v$  is the velocity of SAW,  $\lambda$  is the wavelength of SAW determined by the period of the IDEs,  $f_0$  is the center frequency (resonance frequency) of SAW,  $L$  is the SAW propagation distance between the IDEs, and  $\Delta f$  is the frequency difference between the adjacent maximum of  $S_{21}$ . We can obtain the propagation velocity SAW. Taking the result shown in Figure 3-33 as an example, the periodicity of IDEs is  $20 \mu\text{m}$  with  $5 \mu\text{m}$  width of “finger” and gap, respectively. The central frequency is expected to be around  $168 \text{ MHz}$  as shown in Figure 3-33, or calculated by eq. (3-15) and (2-3) with  $\Delta f = 6 \text{ MHz}$ . As a result, the propagation velocity of SAW is  $v \cong 3.36 \text{ km/s}$ , which agrees with the theoretical expectation.

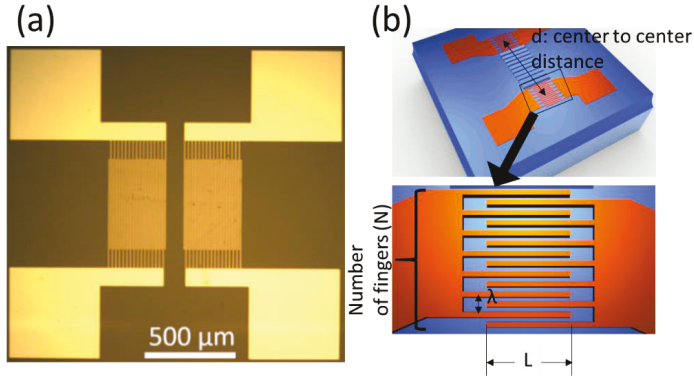


Figure 3-34: (a) Sketch of a SAW measurement structure and (b) parameters of the IDEs.

The aim to integrate the SAW IDEs is to (i) characterize the piezoelectric effect in the strained thin film and (ii) prepare a SAW sensor for *in situ* molecular deposition. In the beginning, various IDEs with different size are prepared on the LiNbO<sub>3</sub> substrate as references in order to find the favorable IDEs that can clearly reveal the center frequency and with less insert losses. Figure 3-34 shows a sketch of the pair of IDEs for SAW. The structural parameters of selected IDEs discussed in this work is shown in Table 3-4.

Table 3-4: Structural parameters of selected SAW structures on LiNbO<sub>3</sub> substrates.

structure name	wavelength $\lambda$ ( $\mu\text{m}$ )	finger width ( $\mu\text{m}$ )	gap ( $\mu\text{m}$ )	total number of fingers N (in one IDE)	number of pairs in one Ide	center to center distance between two IDEs ( $\mu\text{m}$ )	effect length of the finger ( $\mu\text{m}$ )
S1	20	5	5	64	32	845	700
S2	20	5	5	32	16	525	700
S3	20	5	5	8	4	285	700
S4	20	5	5	8	4	585	700
S5	20	5	5	8	4	285	1400

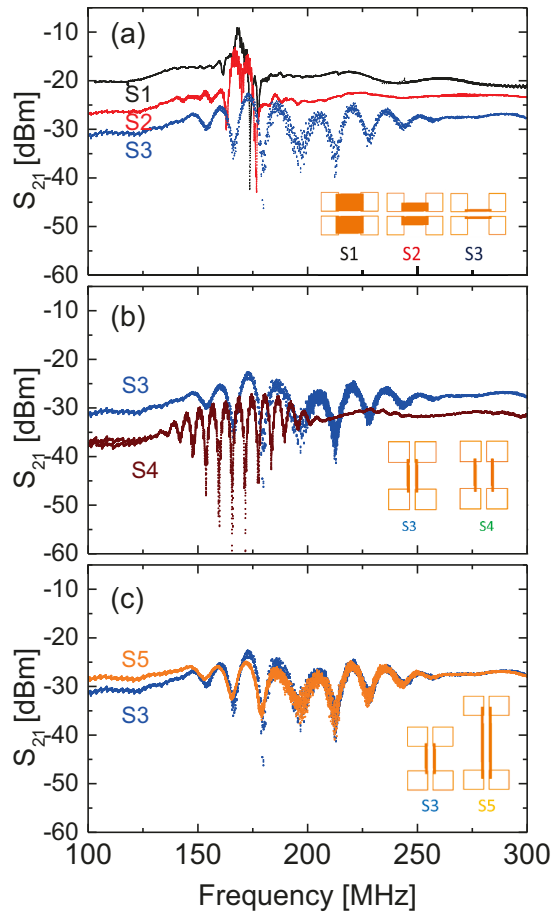


Figure 3-35: Measured SAW spectrum response centered at center frequency of ~ 168 MHz of structures S1 to S5 on LiNbO<sub>3</sub> substrate. The inserts show sketches of the different IDEs.

Figure 3-35 shows the results of comparisons among various IDE designs given in Table 3-4. It reveals that:

- (i) The amplitude increases with the total number of the fingers  $N$  (see S1, S2 and S3, Figure 3-35(a));
- (ii) The bandwidth decreases as  $N$  increases (see S1, S2 and S3, Figure 3-35(a));
- (iii) The difference between the beating frequency  $\Delta f$  decreases as the SAW propagation distance  $d$  (from center to center of IDEs) increases (see S3 and S4, Figure 3-35(b));
- (iv) The SAW spectrum responses show no pronounced dependence on the different finger length (see S3 and S5, Figure 3-35(c)).

The SAW structures chosen for the characterization of strained films in chapter 5 depend on the purpose of measurement. For instance, IDEs with a large number of fingers, short SAW propagation distance result in a relatively narrow spectrum with less interference signal where it is easier to identify the center frequency  $f_0$ . In contrast IDEs with less fingers induce more interference which causes more interference peaks in a spectrum and makes it easier to find  $\Delta f$ . Both of the structures can be used to characterize the velocity of SAW in the strained films.

### 3.3.6 Conductivity measurement

Finally, conductivity measurements are employed in this work to (i) study and understand the conductivity of our nominally isolating films, (ii) analyze the impact of the (anisotropic) strain on the conductivity, and (iii) demonstrate and understand the potential impact of current (e.g. “plasticity”[61, 62]) of the conductance in these materials. The latter might lead to memristor behavior or even artificial synapses device. In order to examine the temperature dependence of the conductivity, the sample is mounted to the sample carrier shown in Figure 3-18, which allows a simultaneous measurement of the conductivity and permittivity in the cryostat. In order to study different electron transport properties of the samples, various kinds of electrodes are prepared on the surface of the oxide film.

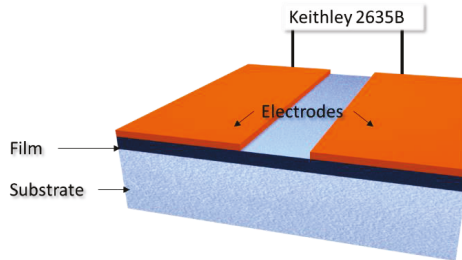


Figure 3-36: Layout of the in-plane conductivity measurement setup using a sourcemeter (Keithley 2635B).

Figure 3-36 sketches the basic layout of the conductivity measurement and Figure 3-37 gives a few examples of electrode designs. The details of the electrode geometry will be discussed in context with the experiments in chapter 5.

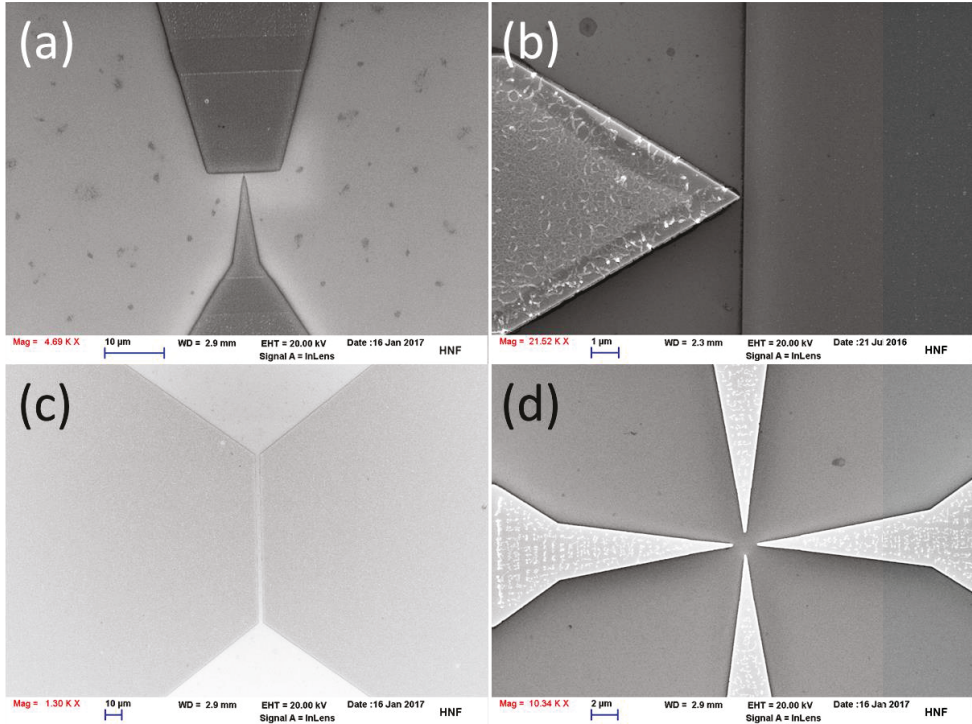


Figure 3-37: Scanning electron microscope images of various electrodes for conductivity measurement. “tip” or “flat” geometries of the electrodes provide different electric field distributions for the conductivity measurements.

Sourcemeeter (Keithley 2635B) is used to apply a dc bias  $V$  and at the same time measure the current  $I$  through the structures providing a conductance  $G = I/V$ . Similar to the capacitive experiment, the conductance consists of at least two contributions:

$$G_{total} = G_{substrate} + G_{film} \quad (3-17)$$

In order to obtain the electronic transport  $G_{film}$  in the film, the conductance of the substrate  $G_{substrate}$  has to be considered. Using the conformal mapping method, we obtain the specific conductivities for “flat” electrode structures (design similar to Figure 3-26):

$$\sigma_{film} = 1 / \left[ \frac{U}{I} \frac{\pi}{4(\ln 2 + (\pi s / 4 t_2))} w \right] \quad (3-18)$$

$$\sigma_{substrate} = 1 / \left[ \frac{U}{I} \frac{1}{\pi} \ln \left( \frac{16 t_3}{\pi s} \right) w \right] \quad (3-19)$$

where  $w$  is the width of the planar capacitor,  $l$  is the length of the resistor from one electrode to another one,  $s$  is the gap of the resistor,  $t_1$ ,  $t_2$ , and  $t_3$  is the thickness of electrode, film, and substrate, respectively (see Figure 3-26),  $U$  and  $I$  are measured voltage and current.

## 4. Engineering the dielectric properties of (Ba,Sr)TiO<sub>3</sub> via tensile strain

In this chapter, the effects of strain (in-plane tensile strain) on the electrical properties of (Ba<sub>x</sub>Sr<sub>1-x</sub>)TiO<sub>3</sub> (BSTO) thin films is presented.<sup>4</sup> Using single crystalline (110)DyScO<sub>3</sub>, (110)TbScO<sub>3</sub>, and (110)GdScO<sub>3</sub> substrates different lattice match and, thus, a different degree of tensile strains is generated in the epitaxially grown films. (see Figure 4-1)

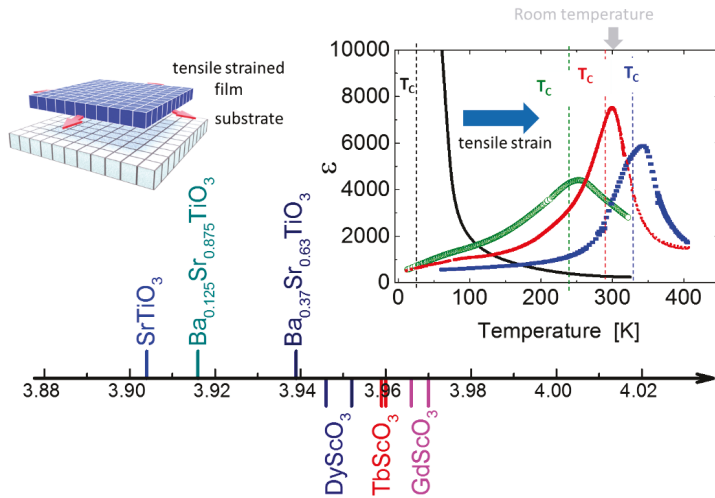


Figure 4-1: The left represents a sketch of a tensile strained film in this work. The right shows the tensile strain impact on the Curie-Weiss temperature. Furthermore, the relevant parameters of film and substrates discussed in this chapter are shown below.

Oxide ferroelectrics show profound features, e.g. giant permittivity, large piezoelectricity, or tunability, in the range of the phase transition temperature from the ferroelectric to the dielectric state. However, this temperature regime is typically far from room temperature. For instance, SrTiO<sub>3</sub> is an incipient ferroelectric, i.e. it shows no phase transition down to the lowest measurable temperatures (~0 K), and other oxides show a ferroelectric to dielectric phase transition far above room temperature, e.g. 403 K for BaTiO<sub>3</sub>,<sup>[63]</sup> 503 to 760K (depending on the composition) for PbZr<sub>1-x</sub>Ti<sub>x</sub>O<sub>3</sub>,<sup>[52]</sup> 763 K for PbTiO<sub>3</sub>,<sup>[64]</sup> and 628 K for NaNbO<sub>3</sub>.<sup>[65]</sup> In order to obtain desirable operating temperatures for these oxides, it is therefore necessary to modify the phase transition temperature for these materials. This engineering of the transition temperature could be achieved via strain, doping, or a combination of both. It has been shown for a number of perovskites,<sup>[66-72]</sup> tungsten bronzes,<sup>[73, 74]</sup> and bismuth layer-structured ferroelectrics<sup>[75, 76]</sup> that the clamp

<sup>4</sup> The majority of this chapter was published in Dai, Y., J. Schubert, E. Hollmann, G. Mussler, and R. Wördenweber, Engineering of the Curie temperature of epitaxial Sr<sub>1-x</sub>Ba<sub>x</sub>TiO<sub>3</sub> films via strain. Journal of Applied Physics, 2016. 120(11): p. 114101.

effect induces strain in epitaxial films resulting in a shift of the phase transition temperature. For example Haeni et al.[66] demonstrated a shift of phase transition temperature to room temperature for SrTiO<sub>3</sub>. However, the previous reports lack the systematic study of the impact of strain on the phase transition temperature. For this it is necessary to study systems with different strain, analyze for instance the impact of defects that lead to a relaxation of strain and last but not least show the impact of strain on other related properties like piezoelectricity or conductivity. This is done in this work.

Here, we report a systematic study of the impact of strain on the phase transition temperature of Ba<sub>x</sub>Sr<sub>1-x</sub>TiO<sub>3</sub> (BSTO) films. In order to obtain an established measure for the analysis of the phase transition temperature, we use the Curie-Weiss temperature  $T_C$ , which is close to the phase transition temperature. Furthermore by using the combination of Ba<sub>x</sub>Sr<sub>1-x</sub>TiO<sub>3</sub> with  $x \leq 0.37$  and various rare earth scandate substrates, we vary the in-plane lattice strain of the films from 0 to 1.7%. The electronic analysis of the films shows a systematic shift of the Curie-Weiss temperature, which is correlated to the in-plane strain. Using theoretical models, which consider the strain-generated formation of defects in the film and their impact on the strain relaxation, we can explain the correlation between the Curie-Weiss temperature and the strain modified structure of these films.

RSM measurements demonstrate that all films are grown epitaxially. The tensile in-plane strain is only partially compensated by a contraction of the out-of-plane lattice parameter. The permittivity is measured in a wide temperature range from 5 K to 400 K, and the Curie-Weiss temperature is evaluated from the temperature dependence of the in-plane dielectric response. The following results are shown and discussed:

- (i) The structural characterization indicates that the volume of the unit cell of the BSTO films increases due to the tensile strain. The resulting Poisson ratio of the film is  $\nu \approx 0.33$ , which is larger than but still close to the literature values of  $\nu \approx 0.23$  for unstrained defect-free SrTiO<sub>3</sub>. This is discussed in chapter 4.1.
- (ii) The permittivity measurements reveals a strain-temperature phase diagram for the epitaxial tensile strained BSTO thin films with a linear dependence of the Curie-Weiss temperature  $T_C$  on the strain. See details in chapter 4.2.1.
- (iii) Using equilibrium thermodynamic analysis (Landau thermodynamic theory), we can demonstrate that this linearity agrees with the theory. Small deviations from Landau theory can be explained by the relaxation of the strain due to defect formation in the film. The result reveals that in addition to the nominal misfit strain, the defect formation strongly affects the effective strain, and, thus, the dielectric response of epitaxially grown ferroelectric films. Details can be found in chapter 4.2.2.
- (iv) In the end, the dependence of the phase transition on the film thickness is analyzed. Especially the anisotropy of the permittivity and the resulting Curie-Weiss temperature

depends strongly on the thickness of the films. Thinner films show a large anisotropy than thicker films and the transition temperature drops dramatically in the thicker (above 120 nm thick) samples where cracks formed. The discussion is shown in chapter 4.2.2.

#### 4.1 Structure characterization

The most imported tool to analyze the epitaxial growth and structural change of the strained films are the various X-ray techniques starting with Bragg-Brentano scans, rocking curves, and, finally, reciprocal space mapping (RSM). These techniques have been introduced in chapter 3.2.1. Here we will provide more insight in the structural properties of our film by focusing on the RSM data. The complete set of XRD data is given in the appendix B.

For the sake of clarity, we arranged the samples according to the strain and labeled them A (smallest strain) to E (largest strain): thus sample A is  $\text{Sr}_{0.63}\text{Ba}_{0.37}\text{TiO}_3/\text{DyScO}_3$ , sample B is  $\text{Sr}_{0.875}\text{Ba}_{0.125}\text{TiO}_3/\text{DyScO}_3$ , sample C is  $\text{SrTiO}_3/\text{DyScO}_3$ , sample D is  $\text{SrTiO}_3/\text{TbScO}_3$ , and sample E is  $\text{SrTiO}_3/\text{GdScO}_3$ (see also Table 4-1).

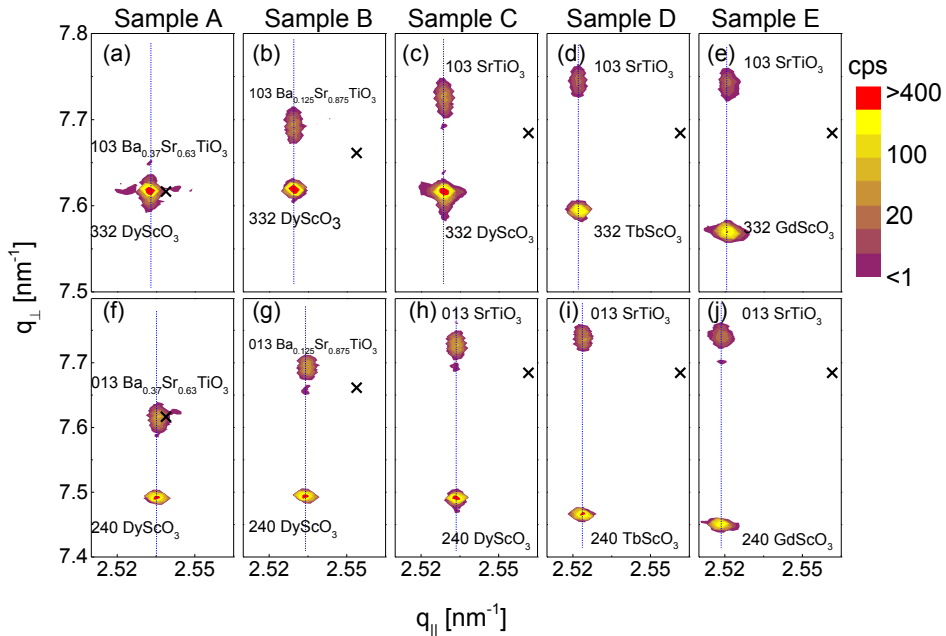


Figure 4-2: RSM of the XRD in the vicinity of the (332) (a-e) and the (240) (f-j) Bragg reflections of the substrates for samples A-E. The crosses mark the corresponding position of the reflection of unstrained BSTO for the respective stoichiometry. Adopted from ref[33].

Figure 4-2 shows a selection of RSM data obtained from XRD analysis of the two different in-plane orientations of the substrates for all samples. The upper and lower figures reveal the lattice correlation in the [001] and  $[1\bar{1}0]$  substrate direction, respectively. Figure 4-2 demonstrates the high quality of the epitaxy for all films. The  $q_{\parallel}$ -values are identical for the film and the substrate, i.e. within the experimental accuracy all in-plane lattice parameters of the films are matched to those of the respective substrate. As a consequence, the difference between the lattice parameters of the strained and unstrained (crosses in Figure 4-2) BSTO increases from sample A to E, i.e.  $q_{\parallel}$  shifts to smaller values compared to the  $q_{\parallel}$  value of the unstrained reference, and  $q_{\perp}$  shifts to larger values compared to its unstrained counterpart. Thus, with increasing lattice mismatch between film and substrate, the film experiences more and more strain. The tensile in-plane strain is partially compensated by a compressive out-of-plane strain. Using the RSM data, we can evaluate the lattice parameters and, thus, evaluate the nominal misfit strain of the films. Table 4-1 provides a summary of the lattice parameters and the resulting nominal misfit strain obtained from averaging the RSM data measured in the four different lattice directions (332),  $(33\bar{2})$ , (420), and (240).

Table 4-1: Lattice parameters (accuracy:  $\pm 0.001 \text{ \AA}$ ) and resulting nominal strain of our strained BSTO films. The lattice parameters  $a_{ref}$  represents the literature value of unstrained material.

Abbreviation	Film	Substrate	Lattice parameters of the film ( $\text{\AA}$ )			Resulting strain (%)			
			Reference	Experiment value			$\epsilon_a$	$\epsilon_b$	$\epsilon_c$
			$a_{ref}$	a	b	c			
A	$\text{Sr}_{0.63}\text{Ba}_{0.37}\text{TiO}_3$	$\text{DyScO}_3$	3.939	3.951	3.945	3.939	0.305 (0.219)	0.152 (0.067)	0.000 (-0.085)
B	$\text{Sr}_{0.875}\text{Ba}_{0.125}\text{TiO}_3$	$\text{DyScO}_3$	3.916	3.949	3.940	3.901	0.843 (0.810)	0.613 (0.580)	-0.383 (-0.415)
C	$\text{SrTiO}_3$	$\text{DyScO}_3$	3.904	3.951	3.946	3.882	1.204 (1.130)	1.076 (1.002)	-0.564 (-0.637)
D	$\text{SrTiO}_3$	$\text{TbScO}_3$	3.904	3.964	3.962	3.877	1.537 (1.403)	1.486 (1.352)	-0.692 (-0.823)
E	$\text{SrTiO}_3$	$\text{GdScO}_3$	3.904	3.971	3.966	3.875	1.716 (1.561)	1.588 (1.433)	-0.743 (-0.894)

Furthermore, corrected values of the strain using a Poisson ratio  $\nu=0.23$  (literature value for unstrained BSTO) are given in parentheses. The correction will be discussed later in this paper.

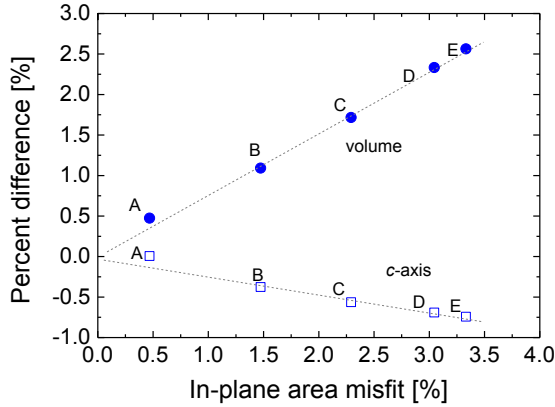


Figure 4-3: Volume of the unit cell (solid circles) and c-axis (open squares) differences as a function of the in-plane areal mismatch for samples A-E. The data are evaluated from the XRD data shown in Figure 4-2, the dashed lines indicate the linear dependence for both parameters. Adopted from ref[33].

In order to learn more about the structural changes induced by the strain, we calculate the in-plane areal lattice misfit and the volumetric change of the BSTO for all films. In a first approach, all misfit values are obtained via a comparison of the measured lattice parameters and the corresponding literature values for unstrained material (see Table 4-1). As such, these values represent nominal values for the c-axis lattice misfit, in-plane areal misfit, and volume mismatch. Later we will show that these values have to be corrected due to structural relaxation effects that are caused by defects in the material. For small concentrations  $x$ , unstrained BSTO has a cubic lattice. Its lattice parameter shows a linear dependence on the change of the barium content at room temperature, which can be approximated by  $a_{ref} = 3.904 + 0.094x$  (Å) for  $0 \leq x < 0.6$ . [77, 78]

Using  $a_{ref}$ , we can evaluate the nominal lattice mismatch for each lattice parameter, e.g.  $\varepsilon_c = (c - a_{ref})/a_{ref}$ , the resulting in-plane area mismatch  $(ab - a_{ref}^2)/a_{ref}^2$ , and the volume mismatch  $(abc - a_{ref}^3)/a_{ref}^3$ . The nominal lattice mismatch is given in tab. 1. Additionally, the c-axis mismatch and the volume change are plotted as a function of the areal misfit in Figure 4-3. The figure shows a linear decrease of the c-axis (out-of-plane) lattice parameter of the BSTO film with increasing areal mismatch, which indicates that the tensile in-plane strain is compensated by a shrinkage of the c-axis. However, this is only a partial compensation since the volume of the unit cell still increases with increasing areal mismatch as shown in Figure 4-3. A very interesting point here is the linear dependence between the volumetric change and the in-plane strain. This not only reveals that the Poisson ratio  $\nu$  is identical for all BSTO films, but we can also derive the value of the Poisson ratio for the strained films. It turns out to be  $\nu \approx 0.33$ , which is larger than but still close to the

literature value  $\nu \approx 0.23$  reported for unstrained crystalline  $\text{SrTiO}_3$ . [79] The increase of the Poisson ratio might be caused by defects in the films, which will be addressed later.

## 4.2 Dielectric properties

### 4.2.1 Strain induced phase transition

In the following, we will discuss the impact of the strain on the dielectric properties. The in-plane permittivity of  $\text{BaTiO}_3$  film under compressive stress are measured in the temperature ranging from 4 K to 500 K, and there is no permittivity peak visible in this temperature. As a result in the following discussions we will focus on the in-plane tensile strain effect. First we will restrict this discussion to the change of the Curie-Weiss temperature  $T_C$  caused by the tensile strain. Generally, changes of the cell volume or lattice parameters affect the ferroelectric phase transition. In BSTO, A-site cation substitution or alternatively mechanical pressure provides such an effect. This was simulated using, for instance, Ising-like model calculations [80] or a classical shell-model potential. [81] With increasing cell volume obtained by Ba-substitution or in-plane tensile strain, the potential well related to ferroelectric distortion becomes wider and deeper, and, as a consequence, the Curie-Weiss temperature is expected to rise. Therefore, the dielectric properties can strongly differ from those of unstrained material. Understanding these effects is of importance for engineering the dielectric properties via strain.

The in-plane dielectric properties are measured along the two orientations for all samples to determine the Curie-Weiss temperature  $T_C$ . Figure 4-4 shows typical data obtained for the permittivity and  $\tan \delta$  as a function of temperature. The peak in the permittivity and  $\tan \delta$  indicates the transition from the dielectric to the ferroelectric state. [68] The Curie-Weiss fit provides the exact  $T_C$  value for all samples (see dashed lines and their linear extrapolation in Figure 4-4).

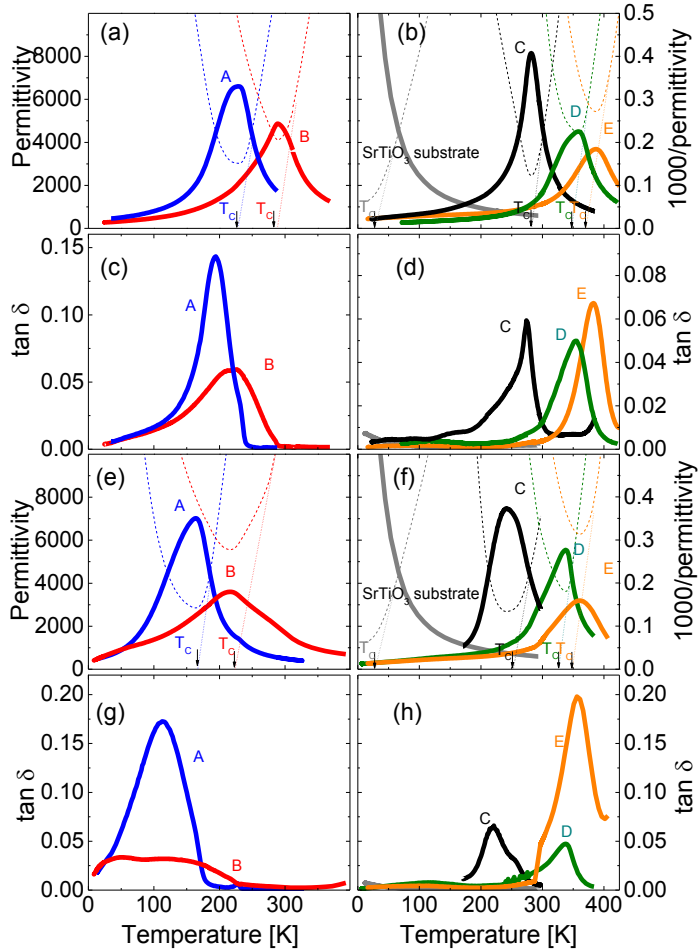


Figure 4-4: Temperature dependence of the dielectric permittivity for large (a, b) and small (e, f) strain and similarly  $\tan \delta$  for large (c, d) and small (g, h) strain for samples A-E (only the data for the large strain direction are displayed) and unstrained  $\text{SrTiO}_3$  (reference sample). The dashed lines in (a, b, e, f) show Curie-Weiss fits (plot of the inverse permittivity (right scale) vs. temperature), and the linear extrapolation provides the Curie-Weiss temperature  $T_C$ .

In order to analyze the impact of the strain on the Curie-Weiss temperature, we consider the change of  $T_C$  due to the strain. According to the literature,  $T_C$  of unstrained  $\text{BSTO}$  can be approximated by a polynomial fit:

$$T_C = a_0 + a_1x - a_2x^2 \quad (4-1)$$

with coefficients  $a_0=30$  K,  $a_1=484$  K, and  $a_2=-136$  K[81-83] or  $a_0=36$  K,  $a_1=356$  K, and  $a_2=0$  K,[84-86] (see Figure 4-5) respectively. The resulting  $T_C$ -values are quite similar for both approaches. We get  $T_C = (33 \pm 6)$  K,  $(84 \pm 8)$  K, and  $(179 \pm 23)$  K for unstrained  $\text{SrTiO}_3$ ,  $\text{Sr}_{0.875}\text{Ba}_{0.125}\text{TiO}_3$ , and  $\text{Sr}_{0.63}\text{Ba}_{0.37}\text{TiO}_3$ , respectively. Using these values as reference values for  $T_C$  of unstrained BSTO, we obtained the resulting change of  $T_C$ .

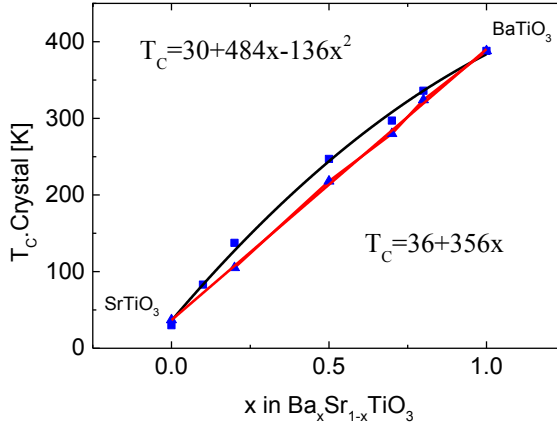


Figure 4-5: Curie-Weiss temperature as function of  $x$  for  $\text{Ba}_x\text{Sr}_{1-x}\text{TiO}_3$  crystals. The different fits (solid lines) result from literature values taken from ref[81-86].

The Landau thermodynamic theory can be used to predict the  $T_C$  enhancement due to strain.[66] In this approach, the shift of the phase transition temperature as a function of in-plane strain is given by:

$$\Delta T_0 = T_{0, \text{film}} - T_{0, \text{ref}} = 2\varepsilon_0 C \frac{Q_{11} + Q_{12}}{s_{11} + s_{12}} \varepsilon \quad (4-2)$$

where  $T_{0, \text{film}}$  and  $T_{0, \text{ref}}$  are the phase transition temperatures of the strained film and of the corresponding unstrained materials, respectively,  $\varepsilon_0$  is the permittivity of vacuum,  $C$  is the Curie-Weiss constant,  $Q_{ij}$  and  $s_{ij}$  represent the electrostrictive coefficients and elastic compliances, and  $\varepsilon$  is the strain. For the calculation we use literature values for the parameters  $Q_{ij}$ ,  $s_{ij}$ , and  $C$  (see Table 4-2). The difference between  $T_C$  and  $T_0$  is smaller than a few K (see appendix C), we can assume that  $\Delta T_C \cong \Delta T_0$ . Therefore eq. (4-2) can be used to predict the shift of the Curie-Weiss temperature due to strain in this work.

Table 4-2: Parameters used for the thermodynamic prediction of  $\Delta T_C$  (eq. (4-1)) for  $\text{SrTiO}_3$  and  $\text{BaTiO}_3$ .

	$Q_{11}+Q_{12}$	$s_{11}+s_{12}$	C	$T_{C,\text{ref}}$
<b>SrTiO<sub>3</sub></b>	-0.033 m <sup>4</sup> /C <sup>2</sup> [87]	$2.38 \times 10^{-12}$ m <sup>2</sup> /N [88]	$9 \times 10^4$ K [82]	36 K
<b>BaTiO<sub>3</sub></b>	-0.065 m <sup>4</sup> /C <sup>2</sup> [89]	$5.65 \times 10^{-12}$ m <sup>2</sup> /N [87]	$12 \times 10^4$ K [82]	393 K

Figure 4-6 shows a comparison of the experimentally determined strain dependence of  $\Delta T_C$  for our BSTO films and theoretical predictions based on thermodynamic considerations using eq. (4-2). The experimental results are based on the nominal strain (later we will demonstrate that these values have to be corrected, see for instance Figure 4-8). The experimental data and the theoretical prediction show the same behavior,  $\Delta T_C$  increases more or less linearly with increasing in-plane strain. The experimental data only deviate from linearity at large strain, and  $\Delta T_C$  seems to start to saturate at  $\epsilon \approx 1.2\%$ . The behavior of  $\text{BaTiO}_3$ ,  $\text{SrTiO}_3$ , and their mixture seems to be very similar. Let us discuss the different aspects of this plot in detail. There is only a small difference between the predictions for  $\text{SrTiO}_3$  and  $\text{BaTiO}_3$ , i.e.  $\Delta T_C$  is only slightly larger for  $\text{BaTiO}_3$ . Furthermore, both predictions already agree quite well with the experimental values. Only for large strain ( $\epsilon > 1.2\%$ ) do the measured data deviate from the theory. Compared with the theoretical prediction, it appears that the strain in the film is overestimated for  $\epsilon > 1.2\%$ . A possible reason might be that in this calculation all kinds of strain relaxation are ignored. This will be discussed in the final section of this publication.

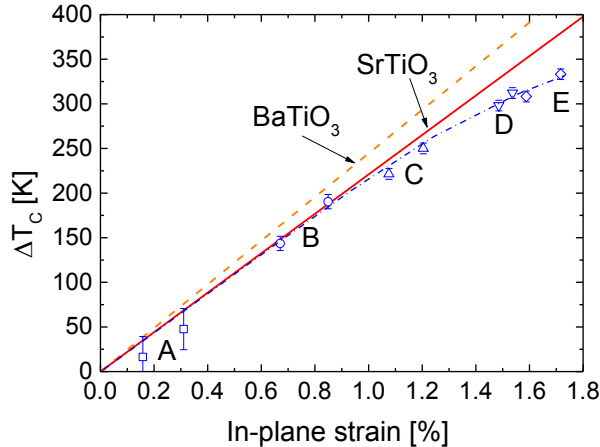


Figure 4-6: Enhancement of  $T_C$  as a function of the nominal in-plane strain for samples A (squares), B (circles), C (up triangles), D (down triangles), and E (diamonds). The samples are measured along the [100] and [010] directions of the film, i.e. there are always two data points for each sample. The in-plane strain is obtained from the comparison of the measured lattice parameters and the literature value of the lattice parameter. Later we demonstrate that this value has to be corrected (see Figure 4-8 and the related

discussion). The lines marked BaTiO<sub>3</sub> and SrTiO<sub>3</sub> represent theoretical predictions (eq. (4-2)) for strained BaTiO<sub>3</sub> and SrTiO<sub>3</sub>, respectively. The dashed-dotted line shows the trend of the experimentally determined strain dependence of  $\Delta T_c$  for our samples (guide for the eye). Adopted from ref[33].

In order to understand the impact of strain in strained epitaxial films, possible mechanisms for strain relaxation have to be considered. One of the major contributions to strain relaxation is provided by misfit dislocations which are automatically generated during film growth due to the strain. These dislocations reduce the elastic energy, and the strain is compensated by these defects which form during film growth.[90, 91] The equilibrium thermodynamic theories developed by van der Merwe[92] and Matthews and Blakeslee[93] predict a critical thickness  $h_c$ , below which the film grows without defects or misfit dislocations. In these theories, the total strain energy is relaxed by the termination of the misfit dislocation. The critical thickness is given by:[94]

$$h_c = \left[ \frac{b}{4\pi(1+\nu)\epsilon_0} \right] \left[ \ln \left( \frac{h_c}{b} \right) + 1 \right], \quad (4-3)$$

where  $\epsilon_0 = (a_{film} - a_{substrate})/a_{film}$  represents the lattice misfit at growth temperature (700 °C) defined by the lattice parameters of the unstrained film ( $a_{film}$ ) and the substrate ( $a_{substrate}$ ) at growth temperature,  $b$  is the extension of the dislocation line, and  $\nu$  is Poisson's ratio. We take reasonable values for  $b=0.4$  nm, Poisson's ratio  $\nu=0.23$  for unstrained BSTO[79] or, alternatively, our experimental value  $\nu=0.33$  for strained BSTO. Furthermore, literature values are used for the lattice parameters and thermal expansion coefficients of the film and substrates.[95] The resulting predictions for the critical thicknesses  $h_c$  due to dislocation formation are 11.1 nm, 9.6 nm, and 5.9 nm for SrTiO<sub>3</sub> grown on DyScO<sub>3</sub>, TbScO<sub>3</sub>, and GdScO<sub>3</sub>, respectively, along the large strain directions. Similarly, the critical thickness can be calculated for the other samples and for the small strain direction of BSTO. The resulting critical thickness is shown in Figure 4-7 as a function of lattice misfit.

Generally, epitaxial films start to grow fully strained until they reach the critical thickness. Once the film reaches the critical thickness, defects develop and the strain in the next layers decreases. As a result, the total effective strain of a film is smaller than the nominal strain, once the critical thickness is exceeded. Considering this effect, the strain relaxation is larger for the films with smaller critical thickness, i.e. the films with larger lattice mismatch.

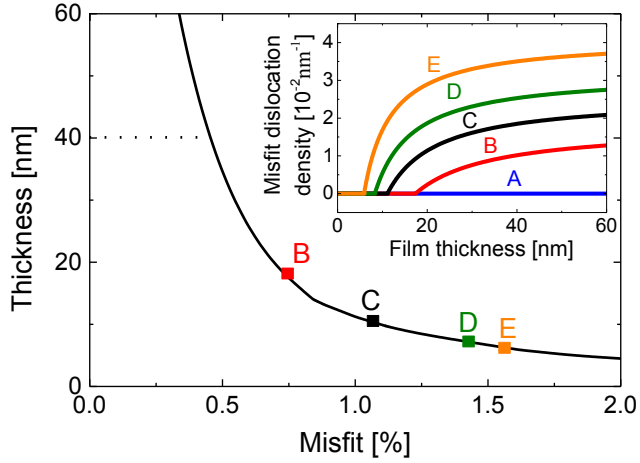


Figure 4-7: Critical thickness for the generation of misfit dislocations according to eq. (4-3). Only the values obtained for the large strain direction are displayed, and the critical thickness of sample A is about 157 nm, i.e. beyond the scale of the plot. The insert shows the misfit dislocation density as a function of film thickness for the large strain direction according to eqs. (4-4) and (4-5). Adopted from ref[33].

The analysis for BSTO (Figure 4-7) shows that for  $\epsilon \lesssim 0.5\%$  the critical thickness exceeds 40 nm, which is the thickness of our films. Therefore, we expect that sample A is fully strained with a very low density of “naturally grown” misfit dislocations. For all other samples, the critical thickness is smaller than 40 nm. As a consequence, dislocations are generated due to the larger lattice mismatch between film and substrate in these samples. In the following, we will briefly discuss the defect-induced strain relaxation in BSTO.

The accumulation of misfit dislocations starts at the critical thickness and eventually leads to complete relaxation of the strain if the films are sufficiently thick. Based on the equilibrium thermodynamic theory, the density of misfit dislocations is given by:[96]

$$\rho = 0, \text{ for } h < h_c \quad (4-4)$$

and

$$\rho \cong \frac{\epsilon_0}{|\mathbf{b}| \cos \lambda} \left(1 - \frac{h_c}{h}\right), \text{ for } h > h_c \quad (4-5)$$

where  $|\mathbf{b}| \cos \lambda$  is the projection of the Burgers vector of the defect to the substrate surface. By simply choosing the most common slip system  $[101]\langle 101 \rangle$  in perovskites,[96] we can use the lattice parameter of  $\text{SrTiO}_3$  (at growth temperature) as  $|\mathbf{b}| \cos \lambda$ . [97] The resulting equilibrium linear misfit dislocation density is given in the insert of Figure 4-7.

Obviously, misfit dislocations and other kinds of defects (e.g. oxygen vacancies[98]) contribute to the relaxation of the strain in the BSTO layers. The effective lattice parameter of the strained film can be approximated by:[79]

$$a_{eff} = \frac{va + vb + (1 - v)c}{1 + v}, \quad (4-6)$$

where  $v$  is Poisson's ratio, and  $a, b$  are the in-plane lattice parameters and  $c$  is the out-of-plane lattice parameter. Inserting reasonable parameters, e.g.  $v = 0.23$  and the experimentally determined lattice parameters (see Table 4-1), we obtain the effective intrinsic lattice parameter. For instance, for SrTiO<sub>3</sub> grown on DyScO<sub>3</sub>, TbScO<sub>3</sub> and GdScO<sub>3</sub> substrates these are 3.907 Å, 3.909 Å and 3.910 Å, respectively. Obviously, the values are slightly larger than the lattice parameter 3.904 Å for perfect (defect-free) SrTiO<sub>3</sub>. [99] Moreover, with increasing lattice mismatch between film and substrate, the effective intrinsic lattice parameter also becomes larger, e.g. in our case SrTiO<sub>3</sub> films grown on GdScO<sub>3</sub> have the largest intrinsic lattice parameter. Therefore, in order to obtain the correct strain one has to consider the lattice parameter of the unstrained material corrected by the effective intrinsic lattice parameter.

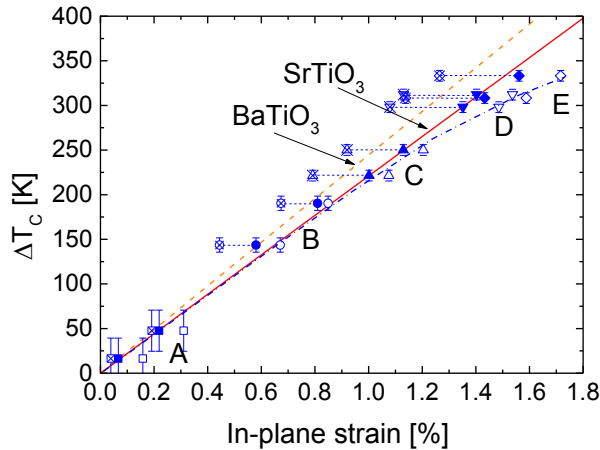


Figure 4-8: Enhancement of  $T_C$  as a function of in-plane strain for sample A (squares), B (circles), C (up triangles), D (down triangles), and E (diamonds) for the large and small strain directions. The open symbols represent data based on the nominal strain (dashed-dotted line serves as a guide for the eye) shown in Figure 4-6. The other symbols show the corrected values using a Poisson's ratio  $v=0.23$  (solid symbols) and  $v=0.33$  (open with crosses), respectively. The lines marked BaTiO<sub>3</sub> and SrTiO<sub>3</sub> represent theoretical predictions (eq. (4-1)) for strained BaTiO<sub>3</sub> and SrTiO<sub>3</sub>, respectively. Adopted from ref[33].

The resulting corrected values are given in Table 4-1 and Figure 4-6. Especially Figure 4-8 nicely demonstrates the improvement of the correlation between  $\Delta T_C$  and the strain obtained by the correction. The effective strain is reduced by the correction. The shift of  $T_C$  as a function of the strain becomes steeper and more linear up to the largest strain (see Figure 4-6), which now is in much better agreement with the theory predicting a linear dependence of  $\Delta T_C$  on the strain.

#### 4.2.2 Critical thickness and anisotropic strain

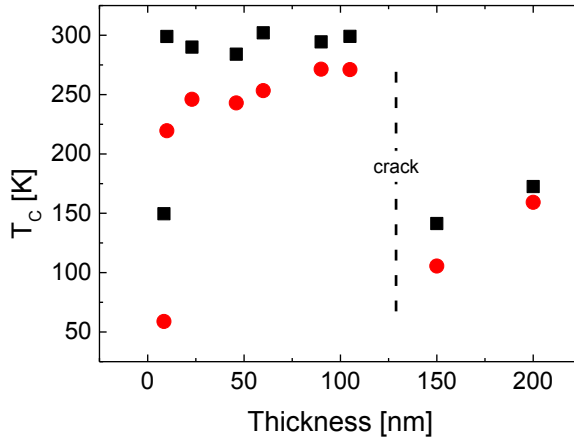


Figure 4-9: Curie-Weiss temperature as function of thickness for  $\text{SrTiO}_3$  films on  $\text{DyScO}_3$  measured for the large strain  $[001]$  (black squares) and small strain  $[1\bar{1}0]$  (red circles) orientation of the electric field.

Finally we analyze the impact of the thickness on the strain-induced ferroelectric phase transition in our strained  $\text{SrTiO}_3$  films. Figure 4-9 shows the Curie-Weiss temperature for  $\text{SrTiO}_3$  films of different thickness deposited on  $\text{DyScO}_3$ . Generally  $T_C$  first increases for both orientations of the electric field (i.e. large and small strain) with increasing thickness up to a “critical thickness” (for PLD deposited  $\text{SrTiO}_3$  on  $\text{DyScO}_3$  at about 120 nm) where crack formation sets in and leads to a strong relaxation of the strain in the film. Above this critical thickness,  $T_C$  drops to values of  $\sim 150$  K.

Figure 4-10 shows a summary of the differences of  $T_C$  measured for large and small in-plane tensile strains for  $\text{SrTiO}_3$  films on various substrates.  $\text{SrTiO}_3/\text{DyScO}_3$  and  $\text{SrTiO}_3/\text{GdScO}_3$  show a more or less exponential decrease of  $\Delta T_C$  with increasing thickness which agrees with the expected

structural relaxation of the lattice (and thus strain) with increasing thickness of the film. The slope of this decrease is steeper for DyScO<sub>3</sub> in the semilogarithmic plot, which agrees with the expectation of a larger anisotropy in DyScO<sub>3</sub> (1.27% and 1.06%) compared to GdScO<sub>3</sub> (1.66% and 1.75%). Finally, SrTiO<sub>3</sub> on TbScO<sub>3</sub> shows hardly any anisotropy since the anisotropy of the lattice parameter is also negligible in TbScO<sub>3</sub> (1.55% and 1.50%). Figure 4-10(b) shows the difference of the T<sub>C</sub> normalized to the average of T<sub>C</sub> for large and small strain. The normalized value decreases dramatically above the critical thickness of approx. 10 – 15 nm [33] where defects appear (not to be confused with the critical thickness for crack formation at about 120 nm). This indicates the relaxation of the strain happens accompanied by the defects.

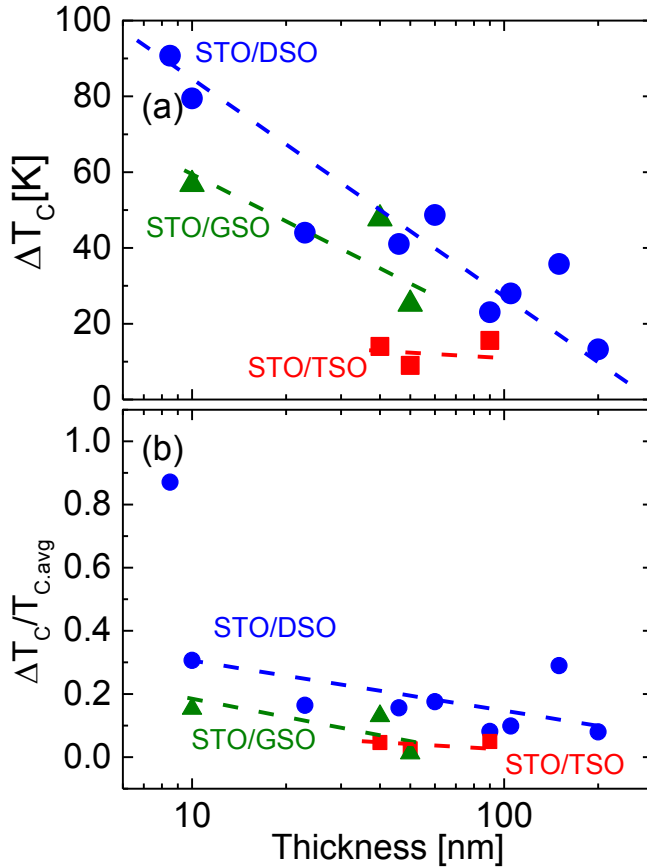


Figure 4-10: Difference  $\Delta T_C$  of (a) the Curie-Weiss temperature measured for large and small tensile strain direction, and (b) normalized to the average of  $T_C$  for large and small strain for each sample as a function of film thickness. The blue circles represent  $SrTiO_3/DyScO_3$ , the orange triangles are  $SrTiO_3/GdScO_3$ , and the red squares represent  $SrTiO_3/TbScO_3$ .

### 4.3 Summary

We systematically studied the correlation between the Curie-Weiss temperature and the strain in epitaxial BSTO films grown on various rare-earth scandate substrates ( $DyScO_3$ ,  $TbScO_3$ , and  $GdScO_3$ ). RSM results demonstrate that all films grow epitaxially on the different scandate

substrates with a resulting in-plane tensile strain that is partially compensated by a reduction of the out-of-plane lattice parameter. The volume of the unit cell increases linearly with the in-plane areal strain. The Poisson ratio of the films turns out to be  $\nu \cong 0.33$ , i.e. larger than but still close to the literature values  $\nu = 0.23$  for unstrained defect-free SrTiO<sub>3</sub>. The Curie-Weiss temperature is extracted from temperature-dependent measurements of the dielectric response. The resulting shift of the Curie-Weiss temperature agrees perfectly with the Landau thermodynamic theory if the strain relaxation due to defect formation in the films is considered.

We also demonstrated that the impact of strain on the properties of ferroelectric films, especially the Curie-Weiss temperature; can be understood and predicted using relatively simple theoretical models, which consider the elastic, electrostrictive, and defect properties of the film. This approach might be useful for the tuning of the transition temperature of ferroelectric thin films and, thus, the ferroelectric properties of these materials at operating temperature, e.g. room temperature. As such it might be a useful tool for the engineering of ferroelectric thin films in order to optimize their properties for the use in various electronic applications.

## 5. Engineering piezoelectric properties of $(\text{K},\text{Na})\text{NbO}_3$ via compressive strain

In this chapter, we will discuss the impact of compressive strain on the ferroelectric properties of  $(\text{K},\text{Na})\text{NbO}_3$  (KNNO) films which are deposited on various scandates substrates. Since KNNO typically shows piezoelectric properties, we will also demonstrate the impact of the strain on the piezoelectric properties by analyzing SAW properties in the strained KNNO films. (see Figure 5-1)

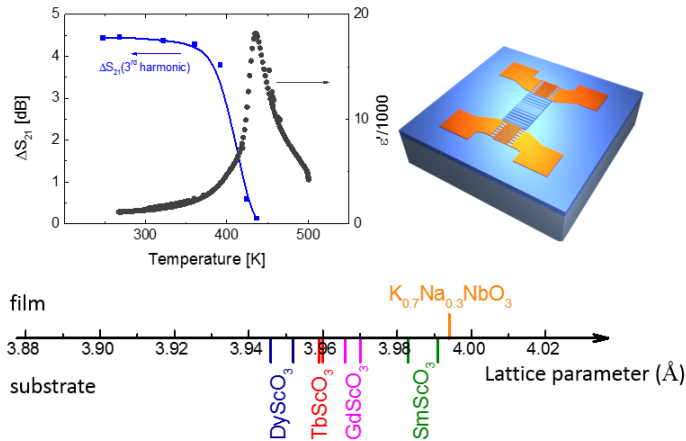


Figure 5-1: Comparison between the permittivity and the SAW response (here 3<sup>rd</sup> harmonic) of a compressively strained KNNO film on  $\text{TbScO}_3$ . The right represents a sketch of a SAW device used in this work. Furthermore the relevant parameters of film and substrates discussed in this chapter are shown below.

The following results are shown and discussed:

- (i) First the structure of the strained KNNO films is examined by XRD experiments (chapter 5.1.1). We demonstrate that all films are epitaxial.
- (ii) Then the permittivity (in-plane) of the films is measured in the temperature range from 4 K to 500 K and the resulting Curie-Weiss temperature  $T_C$  is analyzed (chapter 5.1.2). The Curie-Weiss temperature are clearly reduced from 693 K for unstrained  $\text{K}_{0.7}\text{Na}_{0.3}\text{NbO}_3$  [29] to 300 K to 400 K, depending on the lattice mismatch between the film and substrate (i.e. strain of the film). This indicates that the phase transition is shift to lower temperature with compressive strain.

- (iii) Finally, the propagation of SAW is investigated in our KNNO films using pairs of IDE electrodes for the generation and detection of the SAW (see chapter 5.2). The velocity and transmission coefficients  $S_{21}$  of the SAW as well as their anisotropy are analyzed and correlated to the permittivity of the films. It turns out that the strain can not only tune the dielectric properties of oxides, but also their piezoelectric effects.

## 5.1 Structural characterization and phase transition

Similar to the analysis of our strained BSTO films, we first investigated the epitaxial growth and strain in the KNNO films via XRD experiments. All KNNO films are grown via MOCVD (see chapter 3.1.2) on scandates ((110)DyScO<sub>3</sub>, (110)TbScO<sub>3</sub>, (110)GdScO<sub>3</sub>, and (110)SmScO<sub>3</sub>) and characterized via X-diffraction in the IKZ. In this work we explicitly chose the stoichiometry  $K_xNa_{1-x}NbO_3$  with  $x = 0.7$ , since for  $x > 0.5$  the phases diagram is less complex. For unstrained  $K_{0.7}Na_{0.3}NbO_3$  only one phase transition from the cubic to the tetragonal state is expected at 693 K (see chapter 2.1.2).[29] Figure 5-2 shows typical examples of RSM images of our strained KNNO films on the different scandates:

- (i) The agreement of the  $q_{\parallel}$  position of the film and substrate (in some cases indicated by the dashed line) demonstrates the perfect epitaxial growth of our films. Since the typical film thickness ranges between 30 nm and 50 nm, no structural relaxation is expected.
- (ii) As for the KNNO films, the resulting in-plane strain is partially compensated by an out-of-plane strain of opposite sign, i.e. in this case an increase of the out-of-plane lattice. From the RSM data we obtain for example values of 0.4072 nm (on (110)DyScO<sub>3</sub>) and 0.4017 nm (on (110)SmScO<sub>3</sub>).
- (iii) The satellite patterns can be attributed to different polarized domain structures in the KNNO films. The presence of these patterns are therefore a clear indication of the ferroelectric state at room temperature in all films.

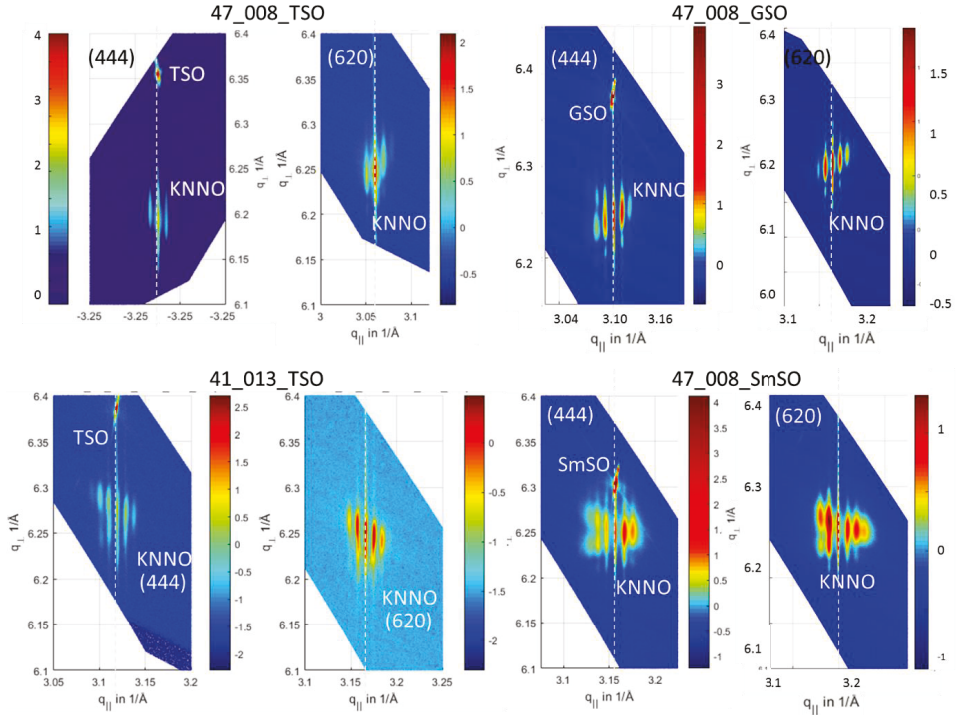


Figure 5-2: RSM of the  $K_{0.7}Na_{0.3}NbO_3$  epitaxial layers on  $(110)TbScO_3$ ,  $(110)GdScO_3$ , and  $(110)SmScO_3$  substrates. Since in some cases the substrate reflex lies outside the  $q_{\perp}$  scale, its  $q_{\parallel}$  position is indicated by the dashed white lines.

In order to determine the Curie-Weiss temperature of the compressively strained KNNO films, similar measurements of the permittivity are performed as shown in chapter 4.2.1, i.e. IDEs are prepared on the surface of KNNO film for electric field directions along the  $[001]$  or  $[1\bar{1}0]$  directions of the substrates and  $\epsilon$  is determined as function of temperature in the temperature range of  $\sim 4$  K to  $\sim 500$  K.

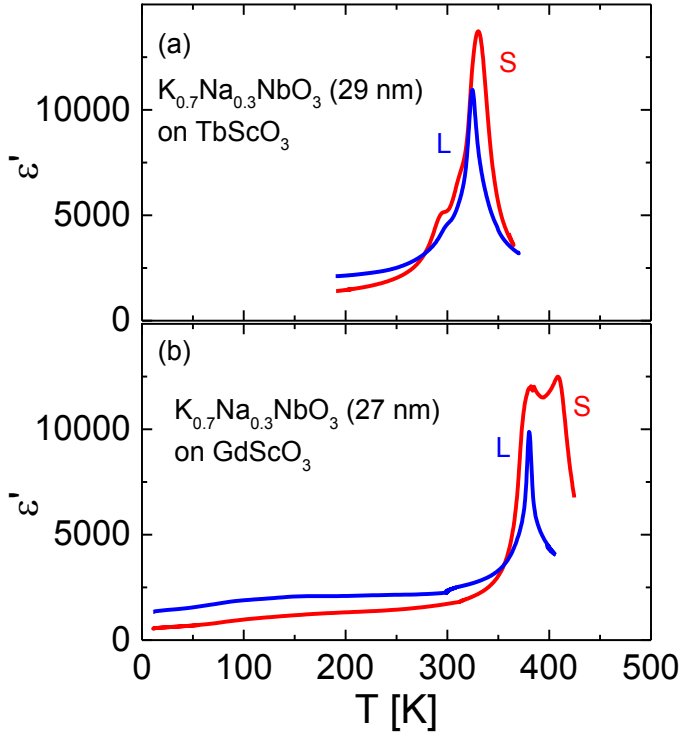


Figure 5-3: Temperature dependence of the dielectric permittivity for (a) a 29 nm thick  $K_{0.7}Na_{0.3}NbO_3$  film on  $TbScO_3$  (sample name 47\_008\_TSO), and (b) a 27 nm thick  $K_{0.7}Na_{0.3}NbO_3$  film on  $GdScO_3$  (sample name 47\_008\_GSO) measured at 100 kHz. “S” and “L” mark the small and large compressive strain in the in-plane orientations, respectively.

Figure 5-3 shows the permittivity as a function of temperature for two  $K_{0.7}Na_{0.3}NbO_3$  films on  $TbScO_3$  and  $GdScO_3$ . The Curie-Weiss temperature  $T_C$  can be extracted from the Curie-Weiss plot, i.e.  $1/\epsilon'$  versus  $T$ .

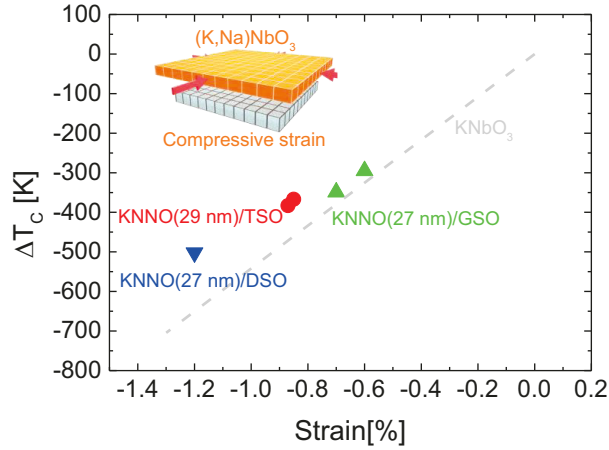


Figure 5-4: Shift of  $T_C$  as a function of strain for  $K_{0.7}Na_{0.3}NbO_3$  films on  $(110)TbScO_3$ ,  $(110)DyScO_3$ , and  $(110)GdScO_3$  substrate. The dashed gray line represents the theoretical prediction for  $KNbO_3$  crystals using eq. (4-2) and the parameters given in Table 4-2.

Figure 5-4 summarizes the results on the shift of  $T_C$  as a function of in-plane compressive strain for our KNNO films on  $TbScO_3$ ,  $DyScO_3$ , and  $GdScO_3$ .  $T_C$  is shifted to lower temperature compared to the  $T_C = 693$  K of unstrained material. Again the two data points obtained for each sample arise from the two in-plane orientations ( $[100]$  and  $[010]$ ) for each film. Since we use the “square-lattice model” (The film adapts a square shaped in-plane structure at the interface to the substrate during the growth) $[100]$  for the evaluation of the nominal strain, the data are in the right order, i.e. large compressive strain yields a large suppression of  $T_C$  in agreement with the theoretical expectation. The use of the “classical model” would yield the opposite result and, thus, contradict the theoretical expectation. As discussed in chapter 4, the shift of  $T_C$  as a function of in-plane compressive strain can be described by the thermodynamic eq. (4-2). Since we only found the necessary parameters for  $KNbO_3$  in the literature (see Table 4-2), we evaluated the expected impact of the strain on  $T_C$  for  $KNbO_3$  (see dashed line in Figure 5-4). Nevertheless, the difference between the theoretical prediction for  $KNbO_3$  and the experimental result for  $K_{0.7}Na_{0.3}NbO_3$  is quite small, indicating the good agreement between the theory and the experiments.

Table 5-1: Parameters used for the thermodynamic prediction of  $\Delta T_C$  (eq. (4-2)) for  $KNbO_3$ .

	$Q_{11}+Q_{12}$	$s_{11}+s_{12}$	$C$
<b>KNbO<sub>3</sub></b>	$0.067 \text{ m}^4/\text{C}^2$ $[101]$	$3.5 \times 10^{-12} \text{ m}^2/\text{N}$ $[101]$	$1.6 \times 10^5 \text{ K}$ $[102]$

## 5.2 SAW devices

In the previous chapters we demonstrate that we can engineer  $T_C$  and thus modify the permittivity of ferroelectric material via strain. In this chapter we will show that this also affects the piezoelectric properties of films. We will demonstrate this via measurements of the SAW for compressively strained KNNO films.

As discussed in chapter 3, identical IDEs are used for the input and output of the SAW. We prepared SAW devices for  $\text{SrTiO}_3$ ,  $\text{BaTiO}_3$ , and  $\text{K}_{0.7}\text{Na}_{0.3}\text{NbO}_3$  on  $\text{DyScO}_3$ ,  $\text{TbScO}_3$ ,  $\text{SmScO}_3$  and  $\text{GdScO}_3$  substrates. Whereas the soft ferroelectric  $\text{SrTiO}_3$  and  $\text{BaTiO}_3$  films showed no measureable SAW signal, the KNNO system did show a significant SAW signal. Therefore we will focus on the SAW experiments on the KNNO strained films. In a first step we optimized the design of the IDEs and their distance (distance between input and output) for the SAW experiments and analyzed the difference of the SAW signal on the orientation of the SAW propagation. Table 5-2 shows different design parameters of SAW IDEs prepared on different samples.

Table 5-2: Design parameters for the SAW IDEs on KNNO films.

structure name	wavelength $\lambda$ ( $\mu\text{m}$ )	finger width and gap ( $\mu\text{m}$ )	total number of fingers N (in one IDE)	Distance between IDEs ( $\mu\text{m}$ )	Effective finger length ( $\mu\text{m}$ )
41_013_TSO	20	5	32	420	500
47_008_TSO	12	3	8	500	300
47_008_GSO	12	3	8	500	300

### (i) SAW signal and propagation velocity

The SAW propagation in our KNNO films strongly depends on its orientation. Figure 5-5 shows the transmission coefficient  $S_{21}$  as function of frequency for a 47 nm thick KNNO film on  $\text{TbScO}_3$  (sample name 41\_013\_TSO) measured for four different orientations of the SAW. Here  $0^\circ$  defines the orientation of the SAW propagation in the  $[1\bar{1}0]\text{TbScO}_3$  direction (i.e. small compressive strain) and  $90^\circ$  defines SAW propagation in the  $[001]\text{TbScO}_3$  direction (i.e. large compressive strain), the directions of  $\pm 45^\circ$  are oriented accordingly.

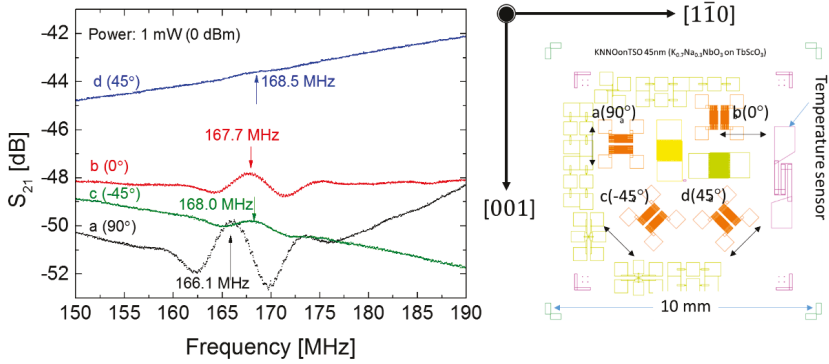


Figure 5-5: Frequency response of different SAW designs on a 47 nm thick  $K_{0.7}Na_{0.3}NbO_3$  film on  $(110)TbScO_3$  (sample name 41\_013\_TSO) showing the frequency range of the first harmonic and AutoCAD image showing the orientation of the different designs a, b, c, and d. The arrow in the graph marks the peak of the SAW signal at the central frequency.

It is interesting to note the center frequency is slightly different in different orientations (Figure 5-5). Actually the center frequency reveals the velocity of SAW:

$$v = \lambda \cdot n \cdot f_n \quad (5-1)$$

where  $\lambda$  is the wavelength of SAW, defined by the period of IDE,  $n$  is the order of harmonic, and  $f_n$  is the  $n^{\text{th}}$  of harmonic. Due to the background noise, the peak of the SAW spectrum cannot always be determined unambiguously (see direction “d” in Figure 5-5).

Another characteristic that can be used for the determination of the SAW velocity is the beating frequency. In acoustic waves, a beat is the interference pattern generated by two interfering waves of different frequencies. In our case, these two waves are the SAW itself and the directly coupled electromagnetic signal of the input IDE. Since the latter moves with the speed of light the resulting correlation that describes this beating is relatively simple:

$$\Delta f = v/L \quad (5-2)$$

where  $\Delta f$  is the difference of frequency between two adjacent maxima of interference pattern in  $S_{21}$  and  $L$  is the distance between two IDEs (input and output). An example of a SAW response on a  $LiNbO_3$  substrate has been presented in chapter 3.3.5. Here we will first discuss the SAW velocity for strained KNNO samples.

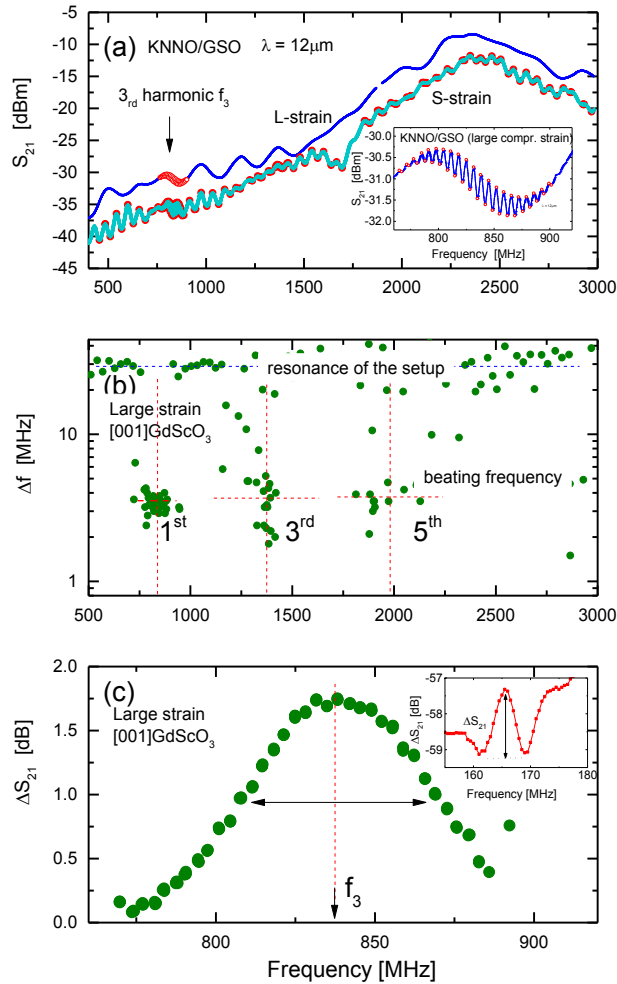


Figure 5-6: (a) Spectral response of SAW along  $[001]\text{GdScO}_3$  (larger compressive strain) and  $[110]\text{GdScO}_3$  (small compressive strain). The insert shows a detailed spectrum in the range around the 3<sup>rd</sup> harmonic frequency, where the automatically recorded maxima and minima are marked (red dots). (b) Difference between adjacent beating frequencies and (c)  $\Delta S_{21}$  at the 3<sup>rd</sup> harmonic frequency measured along  $[001]\text{GdScO}_3$  (sample name 41\_013\_GSO). The inserts shows the definition of  $\Delta S_{21}$ .

Figure 5-6 provides a summary of all data ( $S_{21}$  as function of frequency) and the resulting automatically recorded in this work to identify the velocity and maximum transmission coefficient of the SAW in our strained films. Figure 5-6(a) represents the complete SAW spectrum in the

frequency range from the 3<sup>rd</sup> harmonic to the 9<sup>th</sup> harmonic. It is measured for a KNNO film on GdScO<sub>3</sub> substrate (sample name 41\_013\_GSO) along the large compressive strain ([001]GdScO<sub>3</sub>) and small compressive strain ([001]GdScO<sub>3</sub>) orientations. The geometry of the sample is given in Table 5-2. The insert of (a) shows a detailed spectrum in the range around the 3<sup>rd</sup> harmonic, where the maxima and minima of the response are marked in order to clearly identify  $\Delta f$  and  $\Delta S_{21}$ . Figure 5-6(b) shows the resulting  $\Delta f$  as function of frequency for the large compressive strain direction. It clearly shows two different characteristic frequencies  $\Delta f$ :

- (i) A large value for the minimum-maximum distance  $\Delta f$  at ~30 MHz which characterizes the resonance of the experimental setup and
- (ii) A smaller value for  $\Delta f$  at ~3.4 MHz which represents the beating frequency. The latter is clearly visible at the 3<sup>rd</sup>, 5<sup>th</sup>, and 7<sup>th</sup> harmonics, although the 5<sup>th</sup> and 7<sup>th</sup> harmonics are difficult to be observed directly from the SAW spectrum in Figure 5-6(a). Inserting the value of  $\Delta f$  into eq. (5-2), the velocity of the SAW along large compressive direction at room temperature is calculated as ~3376 m/s.

Figure 5-6(c) shows another way to evaluate the velocity of SAW. Here  $\Delta S_{21}$  is plotted as a function of frequency as depicted in the inset, i.e. the background signal is removed and only the contribution from SAW is presented. The peak of the  $\Delta S_{21}$  spectrum at the 3<sup>rd</sup> harmonic represents the center frequency  $f_3$ . Using eq. (5-1) a velocity of ~3386 m/s is obtained which agrees well with the value obtained from the beating effect. Therefore we assume reasonable values of  $v \cong 3381 \pm 5$  m/s for the velocity of the SAW at room temperature (see Table 5-3).

Table 5-3: Electronic properties of the SAW parameters for a 47 nm and 29 nm thick  $K_{0.7}Na_{0.3}NbO_3$  film on (110)TbScO<sub>3</sub> (sample 41\_013\_TSO) measured at room temperature.

Sample name	Orientation	Center frequency $f_1$ (MHz)	Wave length $\lambda$ ( $\mu$ m)	Velocity (m/s)	$\Delta S_{21}$ (dB)
41_013_TSO	a (90°) [001]	166.1	20	3322	2.44
	b (0°) [ $\bar{1}\bar{1}0$ ]	167.7	20	3354	0.94
	c (-45° to [001])	168	20	3360	0.40
	d (45° to [001])	168.5	20	3370	0.01
47_008_TSO	Large [001]	281.8	12	3381	1.25 (3 <sup>rd</sup> )
	Small [ $\bar{1}\bar{1}0$ ]	279.2	12	3350	1.60 (3 <sup>rd</sup> )

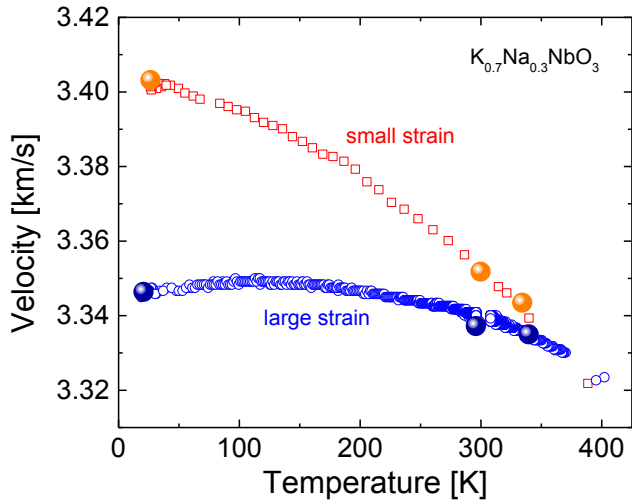


Figure 5-7: Velocity of the SAW as a function of temperature characterized by beating frequency  $\Delta f$  (open symbols) and  $f_3$  (solid symbols) along the large and small compressive strain orientations (sample name 41\_013\_GSO).

In the next step the temperature dependence of velocity is measured (see Figure 5-7). Although the absolute values for the SAW velocity are similar for both directions, their temperature dependence is different. Whereas the SAW velocity is nearly temperature independent for the large strain direction, it decreases slightly with the temperature for the small strain orientation.

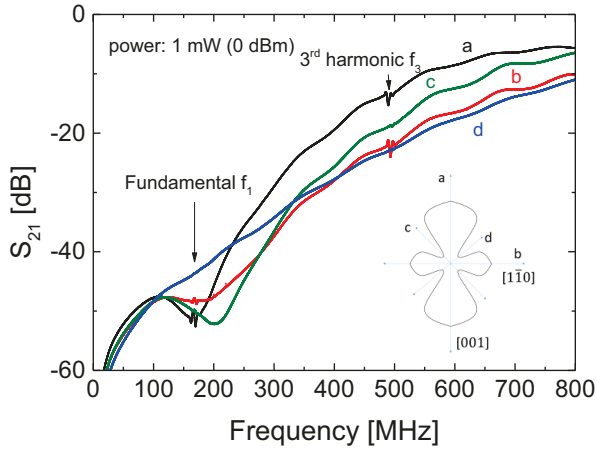


Figure 5-8: SAW response of a 47 nm thick KNNO film on (110)TbScO<sub>3</sub> (sample name 41\_013\_TSO). Showing the fundamental and 3<sup>rd</sup> harmonic for the different designs. Insert shows a sketch of the dependence between SAW velocity and in-plane orientation.

(i) Higher harmonic and anisotropy

The IDE generates (and receives) SAWs when the wavelength is equal to the period of the IDE. Additionally to the center frequency, odd harmonics can be generated and recorded. Figure 5-8 shows as an example the fundamental and 3<sup>rd</sup> harmonic for one of our samples. Normally the signal at odd harmonics should be smaller than for the fundamental frequency. However, in our thin film SAW device, the magnitude of the 3<sup>rd</sup> harmonic is stronger than the fundamental one. Actually it is the strongest SAW signal, the 5<sup>th</sup> to 9<sup>th</sup> harmonic are getting weaker again. Considering the limitation of “large scale” conventional photolithography to be typically ~500 nm for the finger width, the 3<sup>rd</sup> harmonic can be enhanced to about 5 GHz in our KNNO strained film. Since the sensitivity scales with the frequency,[103] this demonstrates the potential for application of these SAW sensors.

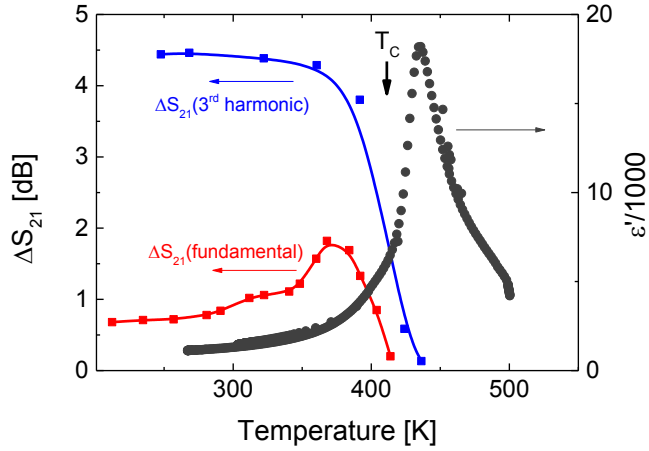


Figure 5-9:  $\Delta S_{21}$  for the fundamental (red) and 3<sup>rd</sup> harmonic (blue) and permittivity (black) as a function of temperature for a 47 nm thick KNNO film on TbScO<sub>3</sub> measured along the  $[1\bar{1}0]$ TbScO<sub>3</sub> orientation (sample name 41\_013\_TSO).

(ii) Correlation between SAWs and the Curie-Weiss temperature

Figure 5-9 demonstrates the correlation between the SAW response and the phase transition, which is obtained from the measurement of the permittivity. It shows the experimental results for a KNNO film on TbScO<sub>3</sub> along  $[1\bar{1}0]$ TbScO<sub>3</sub> direction as function of temperature. The  $T_C$  for this orientation is 416 K. In order to estimate the intensity of SAW from the measured SAW spectrum, we define the value  $\Delta S_{21}$  of the peak-to-valley at center frequency  $f_1$  as shown in Figure 5-9(c). The different  $\Delta S_{21}$  along the different orientations reveal the intrinsic material properties, e.g. the electromechanical coupling effect (the amplitude of SAW is proportional to the piezoelectric constant[104]).  $\Delta S_{21}$  vanishes in the temperature range slightly above the  $T_C$ , where the material enters the paraelectric state. There is even a peak in  $\Delta S_{21}$  for the fundamental frequency range (see Figure 5-9(a)), i.e. the largest SAW signal is obtained slight below the phase transition temperature. As a consequence, the  $\Delta S_{21}$  seems to provide an alternative way to measure the phase transition in terms of the piezoelectric effect.

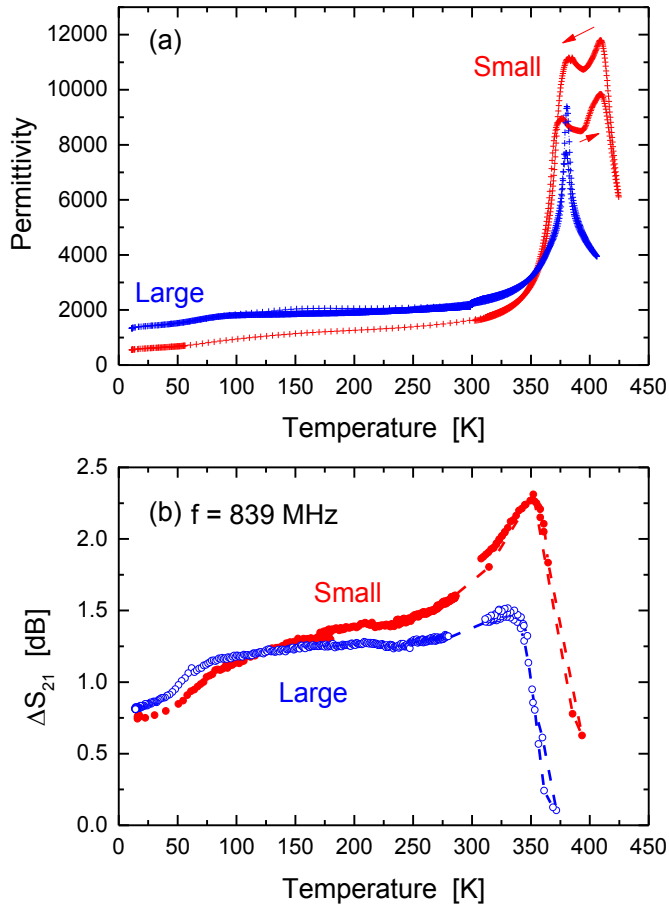


Figure 5-10: Permittivity (a) and  $\Delta S_{21}$  at the 3<sup>rd</sup> harmonic frequency (b) as function of temperature measured along the large ( $[001]$ GdScO<sub>3</sub>) and small ( $[\bar{1}\bar{1}0]$ GdScO<sub>3</sub>) orientations (sample name 41\_013\_GSO).

Finally, Figure 5-10 shows the permittivity and  $\Delta S_{21}$  as a function of temperature measured for a KNNO film on GdScO<sub>3</sub> (sample name 41\_013\_GSO). The results are similar to that shown in Figure 5-9, i.e.  $\Delta S_{21}$  vanishes at  $T_0$  and a maximum just below  $T_0$  (which is close to  $T_C$ ) is observed at the temperature of the onset of the peak in the permittivity. This indicates that the piezoelectric

effect (piezoelectric coefficient) is strongest near the phase transition temperature, as predicted in theory.[16]

### 5.3 Summary

In this chapter, the impact of compressive strain in KNNO thin film on the dielectric and piezoelectric response are characterized and discussed. The result shows:

- (i) In contract to tensile strain effect in SrTiO<sub>3</sub> film, compressive stress in KNNO thin film shifts the  $T_C$  to lower temperature, As in the case of tensile strain in BSTO, it can be fitted by the Landau thermodynamic predictions;
- (ii) Due to its anisotropic strain the dielectric properties depend on the orientation of the field in the KNNO thin film.
- (iii) The propagation of SAW is demonstrated for the KNNO thin film and the SAW response, i.e. strength and velocity, also depend on the in-plane direction of the propagation.
- (iv) The velocity of SAW can be evaluated either via beating frequency or the  $\Delta S_{21}$  spectrum. Both results agrees well with each other and yield values of  $\sim 3.36$  km/s.
- (v) The strength of the signal correlates to the phase transition of the film. It is largest below  $T_C$  and vanishes at  $T_C$ .

In conclusion, we demonstrate that the engineering of  $T_C$  does not only resulting a tuning of dielectric properties, but also allows to tailor the piezoelectric response.

## 6. Engineering the electric transport properties of SrTiO<sub>3</sub> via tensile strain

In this chapter we discuss the impact of strain on the electric transport properties of SrTiO<sub>3</sub> thin films. Generally SrTiO<sub>3</sub> in the cubic perovskite crystal structure is a band insulator with a band gap of 3.2 eV at room temperature. Therefore it can be used as an insulator in the metal-ferroelectric-insulator structure. However, it is known that under compress or tensile strain SrTiO<sub>3</sub> films can vary the electric conductance. This is mainly caused by three mechanisms:

- (i) enhancement of the mobility of electrons and oxygen vacancies due to the strain,[105-107]
- (ii) shift of the phase transition[35, 108], and
- (iii) strain induced oxygen vacancies.[109, 110]

All mechanisms are indicated in Figure 6-1:

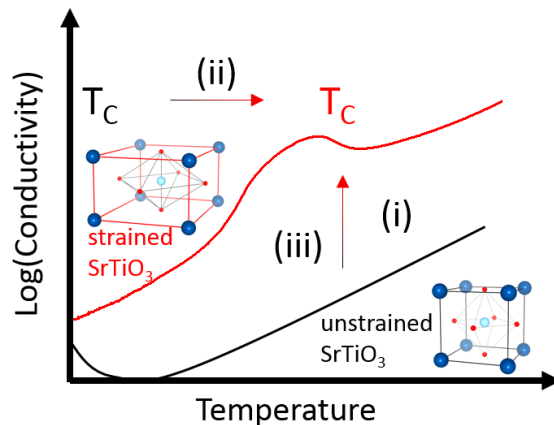


Figure 6-1: Sketch of the impact of strain on the conductivity due to the shift of  $T_C$  and defect formation (oxygen vacancies) in SrTiO<sub>3</sub> thin films.

The neuromorphic computing has become a promising revolutionary approaches for data storage and data operation. In contrast to the classical von Neumann architecture, the neuromorphic architecture provides the ability to tackle complex problems like rigid design, inability to tolerate faults, and the bottleneck of information transfer due to its “learning” ability. Similar to the synapse in the brain, a two-terminal device (memristor with plastic behavior which is also called “artificial synapsis” (see chapter 2.6.2)) is one of the most basic elements in the neuromorphic system. The artificial synapsis involves two important properties:

- (i) a resistive switching behavior (like a classical memristor) and
- (ii) a plasticity, which allows the memristor to be modified (i.e. “learning”).

There exist quite a lot of systems based on various mechanisms that exhibit plastic memristive behavior. For instance, molecular and ionic thin film memristive systems are based on mobile defects in the materials.[111, 112] Insulator-to-metal phase transition driven memristors[113] and ferroelectric memristors are based on electronically driven defects in the materials.[114, 115] One of the most pursued type of memristor is based on uniform and nonuniform oxygen diffusion in oxides.[116] In this type of materials, oxygen vacancies play the significant role in the resistive switching behavior. Different explanations for the diffusion of oxygen vacancy have been suggested ranging from the development of conductive filaments,[117] the modulation of the interface barrier height,[55] and space charge limited current effects.[118] The control of the oxygen vacancy diffusion in these materials represents one of the major issues of these promising type of memristor, especially in case of a “learning” memristor showing plasticity.

The oxide  $\text{SrTiO}_3$  can be modified in order to obtain partial conductivity. This is typically done by enhancing the defects concentration. In previous studies this has been achieved for instance, by Cr-doping [119], varying the growth temperature or oxygen partial pressure[120] , or thermal treatment at elevated temperatures.[121] However, there is no report on strain induced resistive switching behavior in oxides. In this chapter, we use strain to engineer the mobility of oxygen vacancies, and, as a consequence, tune the electric transport properties of oxide thin films. We use epitaxially grown  $\text{SrTiO}_3$  thin films which are strained (typically  $\sim 1\%$ ) due to the lattice mismatch between film and the substrate.

We will start with the basic discussion the electronic transport properties in strained  $\text{SrTiO}_3$  thin film, followed by the presentation of different memristive device based on the strained  $\text{SrTiO}_3$  thin film and their properties.

In the following sections we will use the following notation for the states and the processes in our devices:

- the resistance states of the memristive cell are called “high resistance state (HRS)” or “OFF state”, and,
- “low resistance state (LRS)” or “ON state”.
- A write operation changing a device cell from the HRS to the LRS is called a “SET” operation, while an opposite write operation is called a “RESET” operation.

## 6.1 Strain oxides for neuromorphic engineering

In a first test, epitaxial SrTiO<sub>3</sub> films with various thickness were investigated with respect to their conductivity. All films were deposited via pulsed laser deposition on (110) oriented DyScO<sub>3</sub>, TbScO<sub>3</sub>, and GdScO<sub>3</sub> substrates. According to the discussion in chapter 4, the Curie-Weiss temperature  $T_C$  is shifted to temperature around room temperature for the films deposited on (101)DyScO<sub>3</sub> whereas  $T_C$  is above room temperature for (101)TbScO<sub>3</sub> and even higher for films on (101) GdScO<sub>3</sub> (see Figure 6-2).

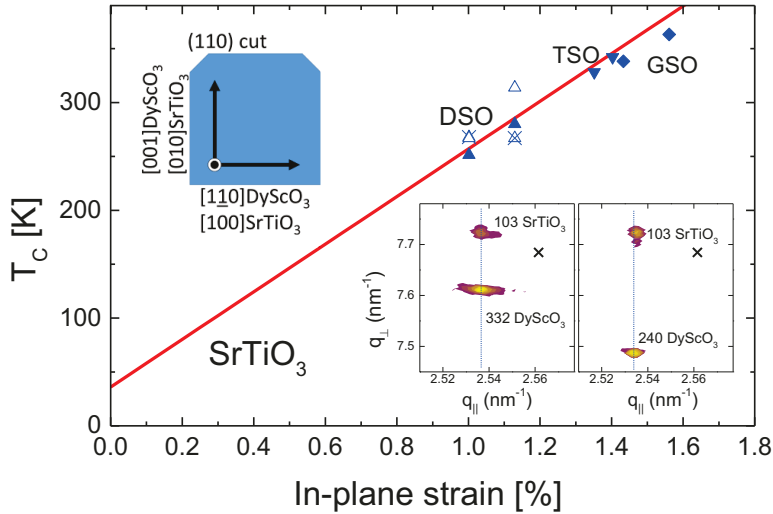


Figure 6-2: Theoretical expectation according to eq. (4-2) (solid line) and experimental data (symbols) for  $T_C$  for strained SrTiO<sub>3</sub>. The different symbols mark the films grown on DyScO<sub>3</sub> (solid up triangles for 40 nm thick film, open up triangles for 60 nm thick film, and crosses mark for 90 nm thick film), TbScO<sub>3</sub> (solid down triangles), and GdScO<sub>3</sub> (solid diamonds) substrates. The inserts show the reciprocal space mapping of the XRD in the vicinity of the (332) (left) and the (240) (right) Bragg reflections of the substrates for a 90 nm thick SrTiO<sub>3</sub> film grown on (101)DyScO<sub>3</sub>. The sketch indicates the crystallographic orientation of the SrTiO<sub>3</sub> in case of the growth on (110)DyScO<sub>3</sub>.

In order to study the electrical properties of the SrTiO<sub>3</sub> films, metal electrodes were deposited on top of the films using e-beam lithography and lift-off lithography technique.[122] Depending on the type of measurement different designs and metal combinations are chosen for the electrodes. They typically consist of a 5 nm thick Ti layer covered with a 50 nm thick Pt layer. In some cases, the Ti layer is omitted. For the characterization of the films and contacts we typically use “flat” electrode (extended plane-parallel electrodes, see for instance insert of Figure 6-4), for the

memristive devices typically a combination of a flat electrode with a sharp tipped electrode (see for instance insert of Figure 6-5(a)) is used.

Figure 6-3 shows the conductivity of two strained  $\text{SrTiO}_3$  films on  $(110)\text{DyScO}_3$  measured along the in-plane directions, i.e. the  $[010]\text{SrTiO}_3$  directions. For comparison the conductivity of unstrained single crystalline  $\text{SrTiO}_3$  is given. The measurements were performed using two opposing flat Ti/Pt electrodes with a length of  $500\ \mu\text{m}$  and a gap distance of  $3\ \mu\text{m}$ . The data are recorded in the ohmic regime in the current-voltage characteristics.

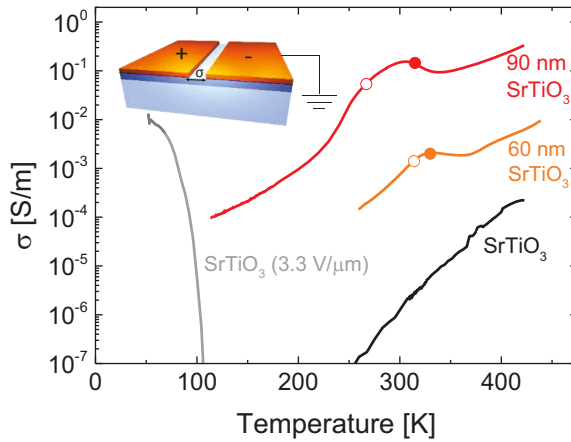


Figure 6-3: Conductivity as function of temperature for a 90 and a 60 nm thick  $\text{SrTiO}_3$  films on  $(110)\text{DyScO}_3$  measured along the large strain  $([010]\text{SrTiO}_3)$  directions and, for comparison, data obtained for single crystalline  $\text{SrTiO}_3$ . All measurements represent the conductivity at small electric fields, i.e. in the ohmic regime, except for the added data for crystalline  $\text{SrTiO}_3$  (gray line) which was measured at elevated field ( $3.3\ \text{V}/\mu\text{m}$ ). The symbols characterize the Curie-Weiss temperature  $T_C$  (open circles) and Burns temperature (solid circles). The insert shows the measurement setup.

Although especially the measurement on the conductivity of the strained films turns out to be difficult due to their “plasticity”, one of the major properties of these films discussed later, there are a number of interesting features visible in Figure 6-3:

- (i) Generally the conductivity is larger in the strained films compared to that of the single crystal. The enhanced conductivity might be a result of the enhanced density of defects (esp. oxygen vacancies) that are automatically generated by the strain in these

films.[33, 110] However, also the mobility of the charge carriers might be affected,[105] for instance by the shift of the phase transition (see next section).

- (ii) In all cases a peak in conductivity can be seen which seems to be associated with the ferroelectric phase transition.[35, 36] This peak is visible for the strained films, it also appears in unstrained SrTiO<sub>3</sub> if we extend the measurement to large fields (i.e. non-ohmic regime). Due to the shift of T<sub>C</sub>, this peak is shifted towards room temperature for our films.
- (iii) Finally, at high temperature (above room temperature) the conductivity increases.

The increased conductivity including the peak in the conductivity just below room temperature is one of the major reasons to choose these system for further memristor and neuromorphic experiments.

## 6.2 From memristor to neuromorphic devices

### 6.2.1 Schottky contact versus ohmic contact

Before we get to the main topic of this work, i.e. the memristor with plastic behavior, let us first discuss the role of the metal/oxides interface. It is known from literature, that the quality of the interface can strongly affect the transport behavior of metal-insulator-metal (MIM) structure devices.[123, 124] For instance, it is reported that Ti deposited on TiO<sub>2</sub> can create a high density of oxygen vacancies near a metal/semiconductor interface.[55] These oxygen vacancies can be beneficial for the resistive behavior of the oxide.[125-127] Therefore we tested two different types of metallic electrodes for our SrTiO<sub>3</sub> films, i.e. Pt-electrodes and a metallic bilayer consisting of Ti and Pt. In the first case the metal-oxide interface is formed by SrTiO<sub>3</sub>/Pt, in the second case it is defined by SrTiO<sub>3</sub>/Ti. The thickness of the Ti and Pt layers are always 5 nm and 50 nm, respectively.

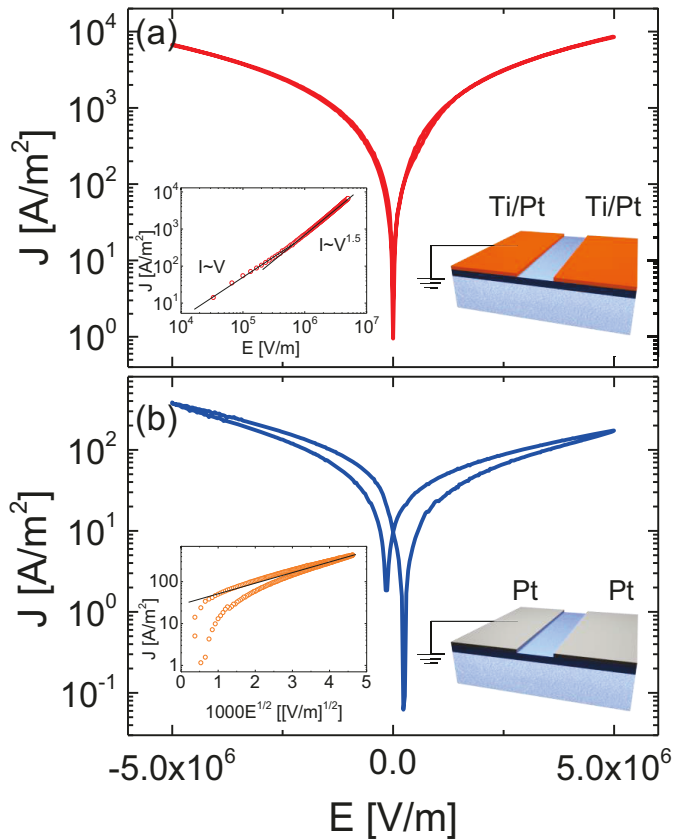


Figure 6-4: IVCs of a 90 nm thick strained SrTiO<sub>3</sub> film measured by two parallel electrodes (gap size 3 μm and length 500 μm) with the electric field oriented for (a) Ti/Pt electrodes and (b) Pt electrodes (see sketches). The inserts represent (a) a double logarithmic plot and (b) Schottky fit along the large tensile strain direction of the forward bias. Please note that always the absolute values of the current is plotted.

Figure 6-4 shows a comparison of typical current-voltage characteristics (IVC) of MIM structures obtained for different combinations of Pt and Ti/Pt electrodes. The measurements are performed at room temperature. In order to record the nano-current in the oxide film, a rather large gap of 3

$\mu\text{m}$  between the electrodes has been chosen. In order to obtain a large enough signal, this large distance is compensated by a large size ( $500\ \mu\text{m}$ ) of the electrodes along the gap (see structures in Figure 6-4). The main features of this experiment are:

- (i) The device with the Ti/Pt electrodes leads to much larger conductivity compared to the device with pure Pt electrode. This is most likely caused by the high density of oxygen vacancies at the  $\text{SrTiO}_3\text{-Ti}$  interface, which reduces the barrier height of the metal-oxide interface.[55, 56]
- (ii) As a result of the Ti layer, the two devices show a different conduction mechanism. In case of the  $\text{SrTiO}_3\text{-Ti}$  interface it behaves ohmic as indicated by the linear IVC obtained for small electric fields  $E < 4.8\ \text{V}/\mu\text{m}$  (see insert of Figure 6-4(a)), whereas we observe a Schottky behavior for the  $\text{SrTiO}_3\text{-Pt}$  interface (see insert of Figure 6-4(b)). Although in other reports the Schottky behavior has been utilized to establish a memristor,[123, 128, 129] we use the ohmic behavior of the  $\text{SrTiO}_3\text{-Ti}$  interface in combination with the strain enhanced conductivity for our artificial synapsis. However, using an asymmetric electrode concept, i.e. a combination of a flat and a tipped electrode.

### 6.2.2 Memristive behavior

Using the strained  $\text{SrTiO}_3$  films on  $(110)\text{DyScO}_3$  in combination with asymmetric Ti/Pt electrodes we developed planar memristors that show the desired plastic behavior. Figure 6-5 shows typical results obtained for asymmetric electrode designs consisting of a sharp tip opposing a flat electrode (see sketch in Figure 6-5(a)). The distance between both electrodes is  $500\ \text{nm}$ . Figure 6-5(a) shows the memristor behavior as well as the plasticity. In this measurement a continuous voltage sweep is applied on the electrodes, the values next to the curves indicate the number of the loop. The IVC loops show the typical memristor behavior with a high current (conductance) in the ON state and a low current (conductance) in the OFF state. However, while the OFF state stays low, the ON state increases with increasing number of cycles (see Figure 6-5(b)). This plastic behavior represents a gradual process defined by the migration of oxygen vacancies (see sketches in Figure 6-5). In the beginning the vacancies form a very thin channel that allow a small transport current. With each loop the channel grows wider until the local electrical field gradient becomes too weak to support any further oxygen vacancies migration. The role of the electric field and the resulting local temperature for the migration of the oxygen vacancies will be discussed later. Indications on the internal dynamics of the devices, i.e. motion of oxygen vacancies and resulting conducting mechanisms, can be obtained from the IVC (see Figure 6-5(c) and (d)).

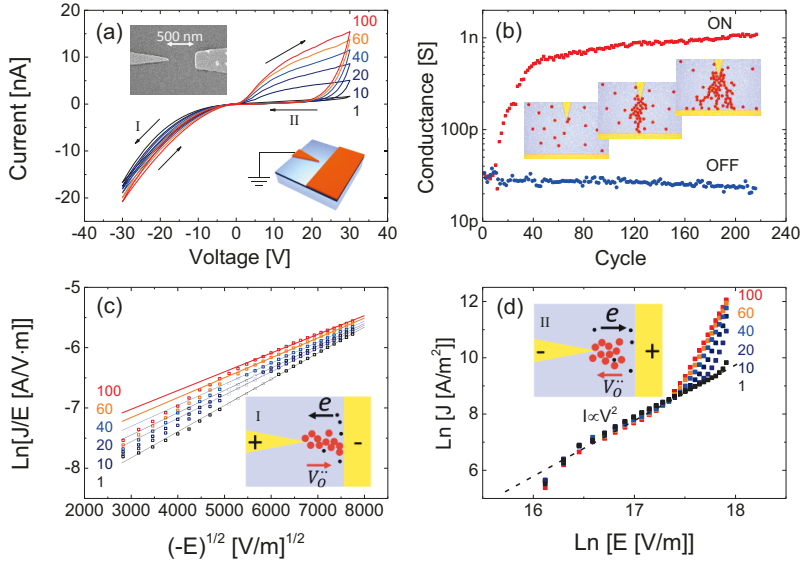


Figure 6-5: IVCs of an asymmetric pair of Ti/Pt electrodes consisting of a flat electrode (500  $\mu\text{m}$  wide) and tip ( $14^\circ$ ) at a distance of 500 nm (sketch in (a)) on a 90 nm large tensile strained SrTiO<sub>3</sub> film. (a) A series of subsequently recorded IVCs demonstrating the plastic memristor behavior, the numbers indicate the number of cycle, the positions for set, reset, and read are indicated. (b) Time dependence of the read signal recorded at a read voltage of 5 V for the ON state (red symbols) and OFF state (blue state) using the data in (a). (c) Poole-Frenkel emission fit of the reverse bias, and (d) double logarithmic of the OFF state plot with slope  $\sim -2$  indicating the trap controlled space charge limited current behavior at the low conductivity state. The sketches in the figure show the electrode geometry (a) or the expected distribution of oxygen vacancies (red dots) in (b, c, and d).

For the negative voltage (set voltage where electrons move from the flat electrode towards the tip) a Poole-Frenkel (PF) behavior [130] is observed (Figure 6-5(c)). The PF emission describes the hopping of electrons in an electrical insulator. Electrons are trapped in localized states. Due to thermal fluctuation they can briefly be excited to the conduction band and move under the impact of an electric field. For large electric fields this leads to a current density  $J$ :

$$J = q\mu E n_0 \exp \left[ -\frac{q\phi_B}{kT} + \frac{q}{kT} \left( \frac{qE}{\pi\epsilon\epsilon_0} \right)^{1/2} \right] \quad (6-1)$$

where  $q$  is the electron charge,  $\mu$  is the electronic drift mobility,  $n_0$  is the density of states in the conduction band (here the defect concentration),  $\phi_B$  is the voltage barrier for the hopping of the electrons in an isolator of the trap, and  $\epsilon$  is the dielectric constant.

Figure 6-5(c) shows a typical PF behavior, i.e. a linear correlation between  $\ln(J/E)$  and  $E^{1/2}$  in agreement with eq. (6-1). Using typical values for the mobility  $\mu = 0.4 \cdot 10^{-4} \text{ m}^2 \text{ V}^{-1} \text{ s}^{-1}$  and a density  $n_0 = 1.5 \cdot 10^{24} \text{ m}^{-3}$  of the electrons in  $\text{SrTiO}_3$ , [131] we obtain a value of  $\phi_B \cong 0.19 \text{ eV}$  which might describe the voltage barrier that the electrons overcome when hopping between defects in the  $\text{SrTiO}_3$ . With increasing number of voltage cycles the height and slope of the linear PF fit changes slightly (see Figure 6-5(c)). In terms of the PF model this implies that with the cycles the permittivity changes slightly (slope) and that the concentration  $n_0$  or voltage barrier  $\phi_B$  changes strongly (height of the fit). If we assume that the height of the voltage barrier is a characteristic property of the defects (oxygen vacancies) in our material which is not affected by the voltage cycles, the density of the defects  $n_0$  between the two electrodes has to change due to the voltage cycles. This agrees with the general picture, that electrons move along defects (oxygen vacancies) and that with increasing number of cycles more perculative channels form between both electrodes. This automatically affects the effective of defects between the electrodes. In the forward process, electrons move from the tip to the flat electrode. However, after the reset, oxygen vacancy are pushed away from the flat electrode, which will causes an interruption of the conductive channels. This gap with strongly reduced conductance dominates the conductivity of the forward bias in the OFF state. As a consequence the IVC shows the typical space charge limited current [132] with  $I \propto V^{1/2}$  (see Figure 6-5(d)).

### 6.2.3 Neuromorphic behavior

In order to examine the plastically of these devices, we performed various series of pulse measurements. Figure 6-6 shows a typical result obtained for the planar memristor structure ( $14^\circ$  tip electrode and flat electrode on a 90 nm thick strained  $\text{SrTiO}_3$  on  $\text{DyScO}_3$ ) for a series of set-pulses of different height. The electric fields are subsequently  $-60 \text{ V}/\mu\text{m}$  and  $-40 \text{ V}/\mu\text{m}$  for  $E_{\text{set}}$ ,  $60 \text{ V}/\mu\text{m}$  for  $E_{\text{reset}}$ , and  $10 \text{ V}/\mu\text{m}$  for  $E_{\text{read}}$ . The signal is constant at  $\sim 2 \text{ nS}$  for the off-state, where as it relaxes strongly in the on-state. The initial height of the on-state conductivity depends on

- (i) the starting point, i.e. the read conductivity at which we start the series,
- (ii) the amplitude of the set field  $E_{\text{set}}$ ,
- (iii) the duration of the set-pulse, and
- (iv) the repetition rate of the set-pulse.

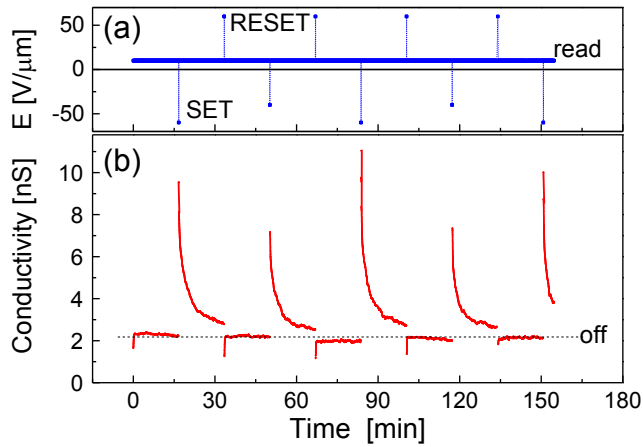


Figure 6-6: (a) Train of voltage pulses with  $+60$  V/ $\mu\text{m}$  for 5 s (RESET) and  $-60$  V/ $\mu\text{m}$  and  $-20$  V/ $\mu\text{m}$  for 5 s (SET) with a read electric field of  $10$  V/ $\mu\text{m}$ , (b) resulting read conductivity.

In the experiment shown in Figure 6-6, only  $E_{\text{set}}$  is varied. For the larger  $E_{\text{set}}$  (1<sup>st</sup>, 3<sup>rd</sup>, and 5<sup>th</sup> pulse) a large initial signal is recorded. The subsequent relaxation of the signal in the read-state looks very similar for all pulses (small and large  $E_{\text{set}}$ ).

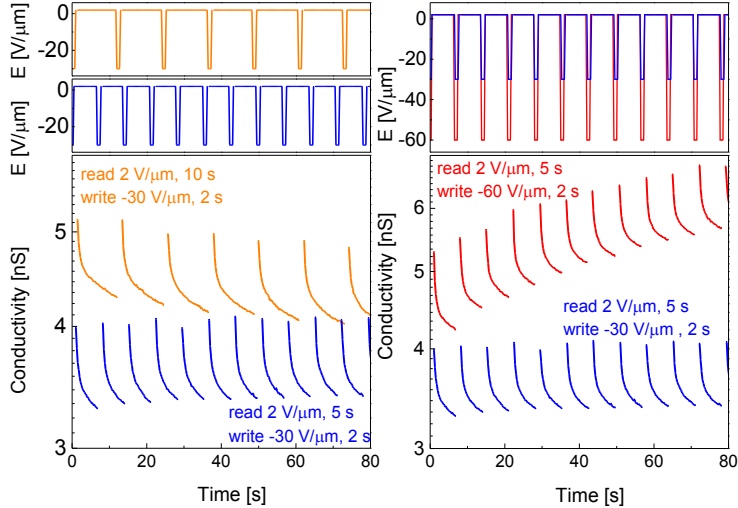


Figure 6-7: Relaxation of the conductivity in the read state for various series of electric set-pulse varying the frequency (left) or amplitude (right) of the stimulus. The top shows the two different set pulses (blue and red), the resulting read conduction is given the figure below using the same color code.

Figure 6-7 shows 4 different series of measurements where the frequency and amplitude of the set-pulses are varied. Moreover, different starting conditions are chosen and no RESET is applied between the pulses. Figure 6-7 demonstrates the large plasticity of the device. In all cases we observe the characteristic relaxation of the ON state signal similar to that shown in Figure 6-6. In the left set, the frequency of the set pulses is changed, and amplitude and pulse duration is identical. For the larger frequency a small increase of the general signal height is observed, whereas for the smaller frequency the general signal height decreases. For the right set, the amplitude of the set-pulse is modified, frequency and duration are identical. Whereas the signal level is nearly unchanged in case of the smaller set amplitude, it increases strongly for the large set amplitude. In conclusion, the signal changes show a large dependence on the set pulse, amplitude, duration and repetition rate, which is similar to biological synaptic plasticity, for instance, for the short term memory.

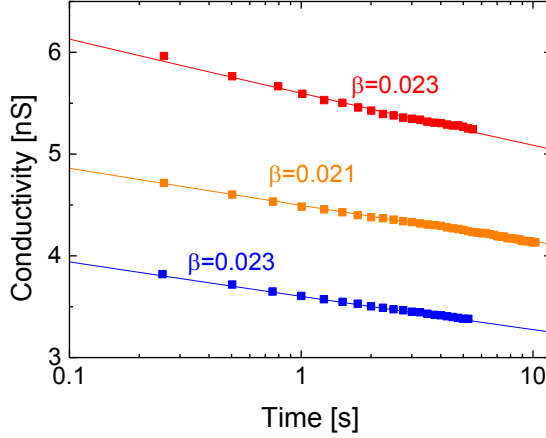


Figure 6-8: Typical fit of the relaxation of the read conductivity after a set pulse according to eq. (6-2). The data represent different measurements shown in Figure 6-7, the resulting mean relaxation time  $\tau \cong 100$  ps, the coupling parameter is  $\beta \cong 0.022$ .

The relaxation of the signal follows the classical relaxation process described by a Kohlrausch-Williams-Watts function:[133]

$$I(t) = A \exp \left[ - \left( \frac{t}{\tau} \right)^\beta \right] \quad (6-2)$$

where  $\beta$  is the coupling parameter (typically  $0 < \beta < 1$ ),  $\tau$  is the mean relaxation time, and A is constant parameter. All relaxation processes observed in our experiments can be fitted using eq. (6-2).

Figure 6-8 shows 3 typical examples. There is no significant difference for the different types of reset pulses. The exponent  $\beta \cong 0.022$  means small coupling in the system which indicates that the distribution of local conductivity is highly inhomogeneous. The mean relaxation time  $\tau \cong 100$  ps corresponds to a frequency of  $\sim 10$  GHz which is characteristic for the limiting frequency of dipole motion in ionic oxide crystals.[134]

#### 6.2.4 Mechanism of resistive switching and plasticity

In order to analyze the impact of the electrodes on the electric field and temperature distribution in the electroforming process, different electrode designs were simulated. In all cases the design was similar to that of the experiments, i.e. a sharp tip opposing a flat electrode with a

distance between the electrodes of 500 nm. However the sharpness (i.e. angle) of the tip was varied. The 2-D electric field distribution is calculated via finite-difference time-domain (FDTD) method [135] A typical field distribution is shown in the inset of Figure 6-9. Generally the field gradient is largest at tip of the sharp electrode. This gradient increases with the sharpness of the tip, i.e. with decreasing angle that describes the tip geometry. The electric field gradient leads to a current and, thus, to a local heating of the film. Both, electric field and the thermal effect, determine the drift of oxygen vacancy, i.e. the electroforming process.

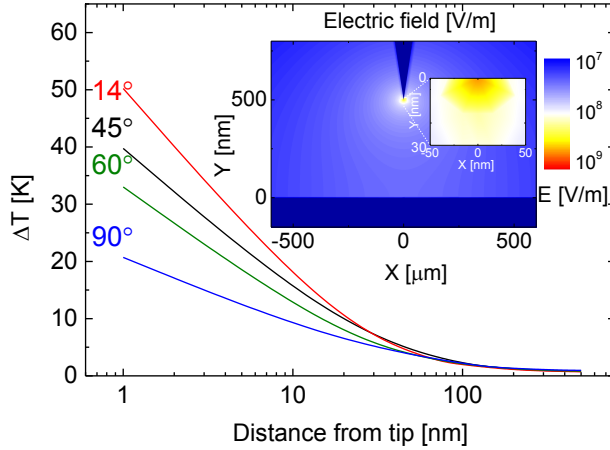


Figure 6-9: Electric field distribution (insert only for 14° tip) and resulting change of temperature as function of distance from the tip to the flat electrode for different angles of the tip electrode.

For the evaluation of the temperature distribution in the device, we consider an electronic heating of the SrTiO<sub>3</sub> between the electrodes and a cooling provided by the substrate. All other effects are negligible. On the one hand the thermal energy induced by a current in small volume V is:

$$Q_{in} = I^2 R t = c m \Delta T \quad (6-3)$$

where  $I$  is the current flowing through V, R and m are resistance and mass of V, c is the specific heat of SrTiO<sub>3</sub>, t is the duration of current pulse, and  $\Delta T$  is the resulting change in temperature. On the other hand, the heat flow through an area  $a^2$  at the interface between the film and the substrate is:

$$Q_{out} = k a^2 \frac{T_{surface} - T_{substrate}}{h} t \quad (6-4)$$

where  $k$  is the thermal conductivity and  $h$  represents the thickness of the film. Inserting reasonable values for our SrTiO<sub>3</sub> films, e.g.  $c = 30$  cal/mol·K,[136] and  $k = 6$  W/(m K),[137] we can evaluate the time  $\tau$  after which the temperature in the SrTiO<sub>3</sub> film is stable (here other effects like the plasticity, i.e. migration of oxygen vacancies, are not considered). Assuming  $Q_{in} = Q_{out}$  in the stable state, we obtain a value  $\tau \leq 5$   $\mu$ s for our SrTiO<sub>3</sub> films of  $h < 100$  nm. This means after an extremely short time of only a few nanoseconds, a state temperature distribution is obtained during electroformation or pulse experiments in our SrTiO<sub>3</sub> film. With this knowledge and the assumption that the substrate represents a large heat sink at a constant temperature (i.e. room temperature), we can even obtain the temperature distribution in the first microseconds of a current pulse using eq. (6-1) and (6-2)

Figure 6-9 shows the change of temperature in the in-plane direction pointing from the tip of the sharp electrode to the flat electrode. Generally the temperature increase peaks at the tip and reduces strongly with the distance to the tip. With increasing sharpness of the tip the  $\Delta T$  increases.

One of the major mechanism in the electroforming process is the migration of oxygen vacancy. This migration is caused by the local temperature and electric field. In the regular lattice of the ionic SrTiO<sub>3</sub>, oxygen vacancies are positively charged. Under a large enough dc electric field, the oxygen vacancies tend to move towards the cathode. At the same time, a high electric field leads to an elevated temperature and, thus, allows migration or enhance the migration speed of oxygen vacancies.[138] However, once a conductance channel is completed, the electric field becomes homogeneous and further migration is stopped. Usually, the drift velocity of the oxygen vacancies is described by the Mott-Gurney equation:[127]

$$v = df \exp\left(-\frac{E_A}{kT}\right) \sinh\left(\frac{zd}{2kT} E\right) \quad (6-5)$$

where  $d$  is the hopping distance,  $f$  is the attempt frequency,  $E_A$  is the activation energy,  $z$  is the charge of the ion, and  $E$  is the electric field. Inserting reasonable values, e.g.  $d = 4$  Å for SrTiO<sub>3</sub>,  $z = 2$  for double positively charged oxygen vacancies, an attempt frequency  $f = 6.67 \times 10^{12}$  Hz, [127] and activation energy of oxygen vacancy of 0.9 eV and 0.7 eV for unstrained and tensile strained SrTiO<sub>3</sub>[106], we can simulated the velocity of oxygen vacancy in unstrained and strained SrTiO<sub>3</sub> as function of electric field and temperature. The resulting 2-D plots of the drift velocities for strained and unstrained SrTiO<sub>3</sub> are shown in Figure 6-10.

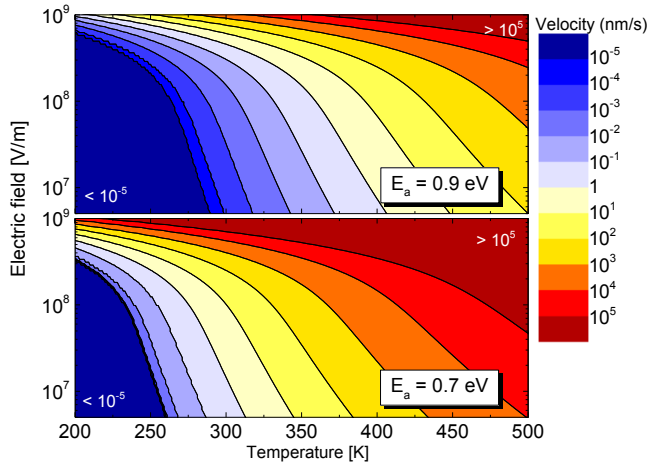


Figure 6-10: 2-D maps of the drift velocity of oxygen vacancy using eq. (6-5) with 0.9 and 0.7 eV activation energy for unstrained and tensile strained SrTiO<sub>3</sub>.

This figure provides a number of interesting information. First, the oxygen vacancy mobility is generally higher in strained SrTiO<sub>3</sub> compared to unstrained SrTiO<sub>3</sub>. From our FDTD simulation (see e.g. insert of Figure 6-9) we know, that the electric field between the two electrodes ranges between 10<sup>7</sup> and few of 10<sup>8</sup> V/m. Already at room temperature, the velocity of oxygen vacancy is of the order of 1 to 10 nm/s for strained SrTiO<sub>3</sub>, which is 100 times faster than for unstrained SrTiO<sub>3</sub>. Second, considering the temperature enhancement in the very beginning of the electroforming process that we discussed before the geometry of the tip electrode plays an important role. Using a sharp tip, the temperature can easily be enhanced by several tens of K, e.g. 50 K for our 14° tip (see Figure 6-9). Due to this temperature increase at the tip, the velocity of oxygen vacancy migration is further enhanced. These simulation results reveal that the combination of strained SrTiO<sub>3</sub> and an optimized electrode design (sharp tip and a flat electrode) lead to a high mobility of the oxygen vacancies. However, too large mobility can be detrimental on even destructive for the device. This can be demonstrated by enhancing either the temperature of the device or the electric field during the experiment.

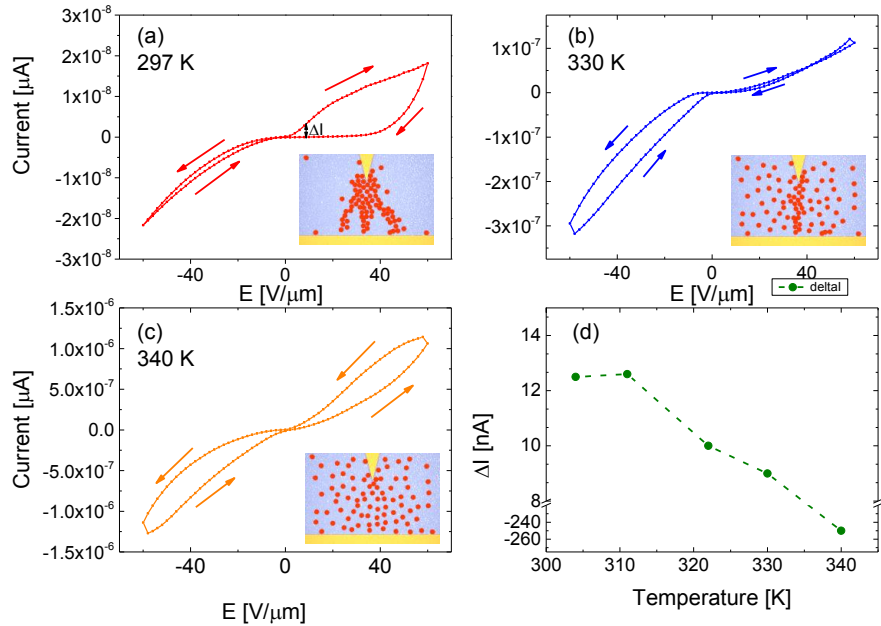


Figure 6-11: (a-c) I-V characteristics of a tip-flat structure on 90 nm tensile strained SrTiO<sub>3</sub> film measured from room temperature up to 340 K. (d) The difference of the read current in the ON state and OFF state.

Figure 6-11 shows a series of IVCs taken at different temperatures. Starting after electroformation at room temperature (Figure 6-11(a)) one obtains a perfect memristor behavior which has already been discussed in detail in Figure 6-5. By increasing the temperature to 330 K (Figure 6-11(b)) the conductivity increases and the hysteresis in the positive voltage regime vanishes, i.e. the difference of the read signal in the ON state and OFF state reduces (see also Figure 6-11(d)). The device is not a perfect memristor anymore. A further enhancement of the temperature by only 10 K to 340 K (Figure 6-11(c)), leads to a strongly enhanced conductivity and an inversion of the hysteresis in the positive voltage regime, i.e. now the IVC is symmetric and does not operate as a memristor anymore. The enhancement of the operating temperature from room temperature to 340 K completely changes the behavior of the device. The expected change in the distribution of oxygen vacancies is sketched in Figure 6-11.

Finally, applying a too large electric field leads to a destruction of the device. Figure 6-12 shows a typical result of such an action. As a result of a too large electric field, an extremely high temperature is obtained at the tip of the sharp electrode. Since in this experiment the electric field

was applied for a long time, the channels in the SrTiO<sub>3</sub> film modified and finally even the Pt-electrodes were completely (sharp electrode) or partially (flat electrode) removed. Since Pt melts at ~2000 K, this indicates that locally extremely high temperatures can be reached. The SEM image does not only show the destruction of the Pt/Ti electrodes. It also shows that the SrTiO<sub>3</sub> layer is modified between the electrodes. The shape of the modified SrTiO<sub>3</sub> forms a triangular area with a tip at the tip of the sharp electrode. This indicates the geometric arrangement of the current channels formed by the oxygen vacancies. A cross-sectional analysis of the elements measured across this area demonstrates that in the area of modified SrTiO<sub>3</sub>, oxygen and Sr is removed (see Figure 6-12).

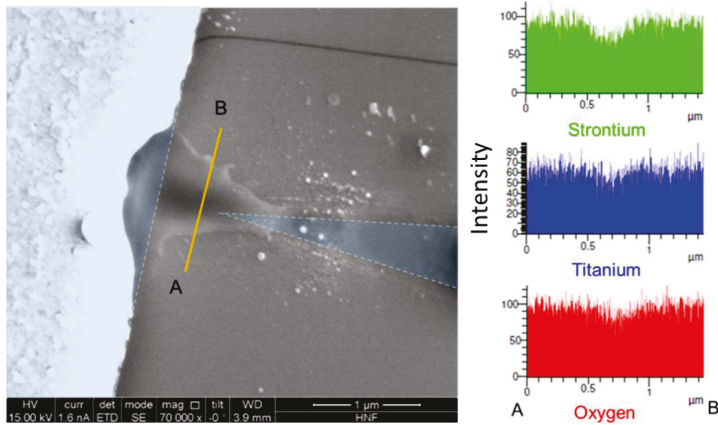


Figure 6-12: SEM picture of a flat-tip structure after the device is hard breakdown. The flat electrode in the left is melt down in 1  $\mu\text{m}$  and the tip electrode in the right is melt away more than 2  $\mu\text{m}$  from the original tip. Between the tip and flat electrode there is a triangle shallow area. The yellow bar from A to B mark the EDX measurement region. The results reveals in the shallow region the Sr, Ti, and O are less than other film region. The loss of Strontium is more pronounced than Ti and O. This non-stoichiometry region provides an un-switchable conductance channel. The hard breakdown structure indicates the temperature distribution is corresponded to the calculated electric field distribution. And the temperature between the two electrodes could reach to more than 2000 K on the surface to melt the SrTiO<sub>3</sub>.

### 6.3 Summary

In this chapter the electric transport properties in strained SrTiO<sub>3</sub> thin film are examined in detail and the possible application in memristor and artificial synapsis devices is demonstrated. In summary of this section:

- (i) Tensile strain causes a shift of the ferroelectric-paraelectric phase transition to room temperature in our SrTiO<sub>3</sub> thin films.

- (ii) Tensile strain enhances the conductivity in SrTiO<sub>3</sub> films, e.g. the conductivity along the in-plane direction is about 0.1 S/m in films at room temperature, while the unstrained SrTiO<sub>3</sub> is an insulator.
- (iii) Tensile strain increases the mobility of the oxygen vacancies in SrTiO<sub>3</sub> film, e.g. already at room temperature, the velocity of oxygen vacancy is of the order of 1 to 10 nm/s for 1.2% strained SrTiO<sub>3</sub> under the electric field of several 10<sup>8</sup> V/m.
- (iv) An additional Ti layer at the electrode/oxides interface reduces the contact barrier and, thus, provides a large electric field in the film which modified the distribution of oxygen vacancies.
- (v) Using an adequate electrode design, the electric field gradient and thus temperature distribution can be affected and a memristor behavior including plasticity (neuromorphic behavior) can be obtained.

## 7. Conclusions

Functional oxides are important for a number of applications in modern electronic industry due to their variety of properties which include their ferroelectric, piezoelectric, and memristive properties. Generally these materials show extraordinary features in the vicinity of their phase transition, which unfortunately is normally far away from room temperature. Thus it is of interest and necessary to modify the phase transition temperature towards operating temperature (typically room temperature) and analyze the resulting modification of the electronic properties.

In this dissertation, the impact of biaxial strain on the electronic properties of epitaxially grown oxide thin films are studied. Perovskites thin films of the systems  $(\text{Ba,Sr})\text{TiO}_3$  and  $\text{K}_{0.7}\text{Na}_{0.3}\text{NbO}_3$  are deposited on various scandites substrates, i.e. (110) oriented  $\text{DyScO}_3$ ,  $\text{TbScO}_3$ ,  $\text{GdScO}_3$ , and  $\text{SmScO}_3$ . The films are strained due to the clamp effect and the difference of the crystalline lattice of film and substrate. The resulting strain in the films range from -1.7% (compressive strain) to 1.7% (tensile strain). We demonstrated that the biaxial strain strongly shifts the phase transition temperature and thus modifies the dielectric, piezoelectric, and electric transport properties of the oxides.

The major results are:

- (i) Strain affects the dielectric properties of the oxide films:
  - The structural characterization via XRD (especially RSM) demonstrates the epitaxial growth for both systems BSTO and KNNO with a nominal strain up to  $\pm 1.7\%$ . Cracks are observed in films with a thickness above a critical thickness of approx. 100 nm, and result in a degradation of the electronic properties.
  - The strain leads to a shift of ferroelectric phase transition. Using the Curie-Weiss temperature  $T_C$  extracted from temperature-dependent measurements of the dielectric response,  $T_C$  can be enhanced from  $\sim 30$  K (unstrained  $\text{SrTiO}_3$ ) to  $\sim 300$  K with the tensile strain of  $\sim 1.2\%$  in tensile strained  $\text{SrTiO}_3$  films. In the compressively strained  $\text{K}_{0.7}\text{Na}_{0.3}\text{NbO}_3$  films the ferroelectric phase transition can be reduced from  $\sim 693$  K ( $T_C$  of unstrained  $\text{K}_{0.7}\text{Na}_{0.3}\text{NbO}_3$ ) to room temperature using a strain of  $\sim -0.9\%$ .
  - Including considerations of the elastic, electrostrictive, and defect properties of the film, the impact of strain on the Curie-Weiss temperature of ferroelectric films can be understood and predicted using a modified Landau thermodynamic theory including especially strain relaxation due to defect formation in the films. This model might be a useful tool for any engineering of ferroelectric thin films for various applications.
  - The dielectric constant exhibits a maximum at the phase transition temperature. In case of  $\text{SrTiO}_3$  the permittivity is enhanced from 300 (unstrained  $\text{SrTiO}_3$ ) to  $\sim 8000$  for tensile strained  $\text{SrTiO}_3$  (1.2% strain). However this value also depends on the homogeneity of the sample, especially on the strain relaxation and, thus, thickness of the film.

- (ii) Strain also affects the piezoelectric properties of the oxide films:
- SAW devices are used to demonstrate the impact of strain on the piezoelectric properties of the films. The propagation of SAW is demonstrated for KNNO films. Similar to the anisotropic dielectric properties induced by biaxial strain, the SAW response, i.e. its strength and velocity, also depends on the in-plane direction of the propagation of the waves.
  - The velocity of SAW can be evaluated either via the beating frequency or the maximum in the  $\Delta S_{21}$  spectrum. Both results agree well with each other and yield reasonable values of  $\sim 3.36$  km/s for our  $K_{0.7}Na_{0.3}NbO_3$  films. The velocity depends slightly on the temperature.
  - The strength of the SAW signal correlates to the phase transition of the films. It is largest slightly below  $T_C$  and vanishes at  $T_C$ .
- (iii) Finally, strain affects the conductance of the oxide films:
- Tensile strain enhances the electron mobility in  $SrTiO_3$  films. For instance, at room temperature the conductivity along the in-plane direction is about 0.1 S/m in films with 1.2 % strain, while the unstrained (defect-free)  $SrTiO_3$  is an insulator.
  - Tensile strain increases also the mobility of the oxygen vacancies in  $SrTiO_3$  film. In our devices and for electric fields between  $10^7$  and several  $10^8$  V/m, the velocity of oxygen vacancy should be of the order of 1 to 10 nm/s for 1.2% tensile strained  $SrTiO_3$  at room temperature, which is 100 times faster than the velocity measured for unstrained  $SrTiO_3$ .
  - An additional Ti layer at the electrode/oxide interface reduces the contact barrier (probably due to the formation of additional oxygen vacancies) and, thus, provides larger electric fields in the film resulting in a large density of oxygen vacancies.
  - Using an adequate electrode design which affects the electric field, and thus temperature distribution in the film, resistance switching behavior is demonstrated in our epitaxial  $SrTiO_3$  thin film, which shows memristor behavior and even a plasticity. The latter has been used for the simulation of biological synapses (i.e. artificial synapsis).

In conclusion, elastic strain provides a tremendous tool to engineer the dielectricity, piezoelectricity, and conductance of oxide materials, which might be exploited for the benefit of the performance of a large number of electronic devices. For instance, SAW mediated transductions based on strained oxide films with high piezoelectricity might be used as highly sensitive sensors in many applications. Artificial synaptic devices might show advantages in energy-efficient neuromorphic computation compared to the conventional computational systems based on von Neumann architectures. It furthermore emulates the computation performed by the biological synapse. This might inspire people to perform biological computing processes, e.g. short-term and long-term memory with nanoscale electrodes arrays. All these examples indicate a brilliant future for strain engineering of functional oxides.

## Reference

1. Desai, S.B., S.R. Madhupathy, A.B. Sachid, J.P. Llinas, Q. Wang, G.H. Ahn, G. Pitner, M.J. Kim, J. Bokor, and C. Hu, *MoS<sub>2</sub> transistors with 1-nanometer gate lengths*. Science, 2016. **354**(6308): p. 99-102.
2. Ribes, G., J. Mitard, M. Denais, S. Bruyere, F. Monsieur, C. Parthasarathy, E. Vincent, and G. Ghibaudo, *Review on high-k dielectrics reliability issues*. IEEE Transactions on Device and materials Reliability, 2005. **5**(1): p. 5-19.
3. Wilk, G.D., R.M. Wallace, and J.M. Anthony, *High- $\kappa$  gate dielectrics: Current status and materials properties considerations*. Journal of Applied Physics, 2001. **89**(10): p. 5243-5275.
4. Wilk, G.D., R.M. Wallace, and J. Anthony, *High- $\kappa$  gate dielectrics: Current status and materials properties considerations*. Journal of applied physics, 2001. **89**(10): p. 5243-5275.
5. Peltzel, J., T. Ostapchuk, I. Gregora, I. Rychetský, S. Hoffmann-Eifert, A. Pronin, Y. Yuzyuk, B. Gorshunov, S. Kamba, and V. Bovtun, *Dielectric, infrared, and Raman response of undoped SrTiO<sub>3</sub> ceramics: evidence of polar grain boundaries*. Physical Review B, 2001. **64**(18): p. 184111.
6. Vendik, O.G. and L.T. Ter-Martirosyan, *Influence of charged defects on the dielectric response of incipient ferroelectrics*. Journal of Applied Physics, 2000. **87**(3): p. 1435-1439.
7. Nomura, K., H. Ohta, K. Ueda, T. Kamiya, M. Hirano, and H. Hosono, *Thin-film transistor fabricated in single-crystalline transparent oxide semiconductor*. Science, 2003. **300**(5623): p. 1269-1272.
8. Fortunato, E., P. Barquinha, and R. Martins, *Oxide semiconductor thin - film transistors: a review of recent advances*. Advanced materials, 2012. **24**(22): p. 2945-2986.
9. Caspari, M.E. and W.J. Merz, *The Electromechanical Behavior of BaTiO<sub>3</sub> Single-Domain Crystals*. Physical Review, 1950. **80**(6): p. 1082-1089.
10. Beattie, A.G. and G.A. Samara, *Pressure Dependence of the Elastic Constants of SrTiO<sub>3</sub>*. Journal of Applied Physics, 1971. **42**(6): p. 2376-2381.
11. Ajaxon, I., A. Acciaioli, G. Lionello, M.P. Ginebra, C. Ohman-Magi, M. Baleani, and C. Persson, *Elastic properties and strain-to-crack-initiation of calcium phosphate bone cements: Revelations of a high-resolution measurement technique*. J Mech Behav Biomed Mater, 2017. **74**: p. 428-437.
12. Nguyen, L.D., A.S. Brown, M.A. Thompson, and L.M. Jelloian, *50-Nm Self-Aligned-Gate Pseudomorphic Alinas Gainas High Electron-Mobility Transistors*. Ieee Transactions on Electron Devices, 1992. **39**(9): p. 2007-2014.
13. Beach, R.S., J.A. Borchers, A. Matheny, R.W. Erwin, M.B. Salamon, B. Everitt, K. Pettit, J.J. Rhyne, and C.P. Flynn, *Enhanced Curie temperatures and magnetoelastic domains in Dy/Lu superlattices and films*. Phys Rev Lett, 1993. **70**(22): p. 3502-3505.
14. Sato, H. and M. Naito, *Increase in the superconducting transition temperature by anisotropic strain effect in (001) La<sub>1.85</sub>Sr<sub>0.15</sub>CuO<sub>4</sub> thin films on LaSrAlO<sub>4</sub> substrates*. Physica C: Superconductivity, 1997. **274**(3-4): p. 221-226.
15. Pertsev, N.A., A.K. Tagantsev, and N. Setter, *Phase transitions and strain-induced ferroelectricity in SrTiO<sub>3</sub> epitaxial thin films*. Physical Review B, 2000. **61**(2): p. R825-R829.
16. Budimir, M., D. Damjanovic, and N. Setter, *Piezoelectric anisotropy-phase transition relations in perovskite single crystals*. Journal of Applied Physics, 2003. **94**(10): p. 6753-6761.
17. Cardona, M., *Optical Properties and Band Structure of SrTiO<sub>3</sub> and BaTiO<sub>3</sub>*. Physical Review, 1965. **140**(2A): p. A651.
18. Waser, R., T. Baiatu, and K.H. Härdtl, *dc Electrical Degradation of Perovskite - Type Titanates: II, Single Crystals*. Journal of the American Ceramic Society, 1990. **73**(6): p. 1654-1662.
19. Lemanov, V.V., E.P. Smirnova, P.P. Syrnikov, and E.A. Tarakanov, *Phase transitions and glasslike behavior in Sr<sub>1-x</sub>Ba<sub>x</sub>TiO<sub>3</sub>*. Physical Review B, 1996. **54**(5): p. 3151-3157.
20. Vendik, O.G. and S.P. Zubko, *Ferroelectric phase transition and maximum dielectric permittivity of displacement type ferroelectrics (Ba<sub>x</sub>Sr<sub>1-x</sub>TiO<sub>3</sub>)*. Journal of Applied Physics, 2000. **88**(9): p. 5343-5350.

21. Li, J.F., K. Wang, F.Y. Zhu, L.Q. Cheng, and F.Z. Yao, *(K, Na) NbO<sub>3</sub> - Based Lead - Free Piezoceramics: Fundamental Aspects, Processing Technologies, and Remaining Challenges*. Journal of the American Ceramic Society, 2013. **96**(12): p. 3677-3696.
22. Darlington, C.N.W. and H.D. Megaw, *The low-temperature phase transition of sodium niobate and the structure of the low-temperature phase*, *N. Acta Crystallographica Section B Structural Crystallography and Crystal Chemistry*, 1973. **29**(10): p. 2171-2185.
23. Sellmann, J., *Impact of strain and composition on structural and piezo-/ferroelectric properties of epitaxial NaNbO<sub>3</sub> and K<sub>x</sub>Na<sub>1-x</sub>NbO<sub>3</sub> thin films and superlattices grown by PLD*, in *Technische Universität Berlin*. 2015, Technische Universität Berlin.
24. Guo, Y., K.-i. Kakimoto, and H. Ohsato, *Phase transitional behavior and piezoelectric properties of (Na<sub>0.5</sub>K<sub>0.5</sub>)NbO<sub>3</sub>-LiNbO<sub>3</sub> ceramics*. Applied Physics Letters, 2004. **85**(18): p. 4121-4123.
25. Liang, L.Y., Y.L. Li, L.Q. Chen, S.Y. Hu, and G.H. Lu, *Thermodynamics and ferroelectric properties of KNbO<sub>3</sub>*. Journal of Applied Physics, 2009. **106**(10): p. 104118.
26. Wu, L., J.L. Zhang, C.L. Wang, and J.C. Li, *Influence of compositional ratio K/Na on physical properties in (K<sub>x</sub>Na<sub>1-x</sub>)NbO<sub>3</sub> ceramics*. Journal of Applied Physics, 2008. **103**(8): p. 084116.
27. Vailionis, A., H. Boschker, W. Siemons, E.P. Houwman, D.H.A. Blank, G. Rijnders, and G. Koster, *Misfit strain accommodation in epitaxial ABO<sub>3</sub> perovskites: Lattice rotations and lattice modulations*. Physical Review B, 2011. **83**(6).
28. Wang, K. and J.-F. Li, *Analysis of crystallographic evolution in (Na,K)NbO<sub>3</sub>-based lead-free piezoceramics by x-ray diffraction*. Applied Physics Letters, 2007. **91**(26): p. 262902.
29. Ahtee, M. and A. Hewat, *Structural phase transitions in sodium-potassium niobate solid solutions by neutron powder diffraction*. Acta Crystallographica Section A: Crystal Physics, Diffraction, Theoretical and General Crystallography, 1978. **34**(2): p. 309-317.
30. Glazer, A.M., *The classification of tilted octahedra in perovskites*. Acta Crystallographica Section B Structural Crystallography and Crystal Chemistry, 1972. **28**(11): p. 3384-3392.
31. Kadanoff, L.P., W. GÖTze, D. Hamblen, R. Hecht, E.A.S. Lewis, V.V. Palciauskas, M. Rayl, J. Swift, D. Aspnès, and J. Kane, *Static Phenomena Near Critical Points: Theory and Experiment*. Reviews of Modern Physics, 1967. **39**(2): p. 395-431.
32. Kittel, C., *Introduction to solid state physics*. 2005: Wiley.
33. Dai, Y., J. Schubert, E. Hollmann, G. Mussler, and R. Wördenweber, *Engineering of the Curie temperature of epitaxial Sr<sub>1-x</sub>Ba<sub>x</sub>TiO<sub>3</sub> films via strain*. Journal of Applied Physics, 2016. **120**(11): p. 114101.
34. Alldredge, L.M.B., W. Chang, S.W. Kirchoefer, and J.M. Pond, *Phase transitions and the temperature dependence of the dielectric properties in tetragonally strained barium strontium titanate films*. Applied Physics Letters, 2009. **94**(5): p. 052904.
35. Bock, J.A., S. Lee, S. Trolier-McKinstry, and C.A. Randall, *Metallic-like to nonmetallic transitions in a variety of heavily oxygen deficient ferroelectrics*. Applied Physics Letters, 2015. **107**(9): p. 092902.
36. Tiwari, A., C. Jin, and J. Narayan, *Strain-induced tuning of metal-insulator transition in NdNiO<sub>3</sub>*. Applied Physics Letters, 2002. **80**(21): p. 4039-4041.
37. Jiang, L., W. Seok Choi, H. Jeon, T. Egami, and H. Nyung Lee, *Strongly coupled phase transition in ferroelectric/correlated electron oxide heterostructures*. Applied Physics Letters, 2012. **101**(4): p. 042902.
38. Goldschmidt, V.M., *Die Gesetze der Krystallochemie*. Die Naturwissenschaften, 1926. **14**(21): p. 477-485.
39. Randall, C., A. Bhalla, T. Shrout, and L. Cross, *Classification and consequences of complex lead perovskite ferroelectrics with regard to B-site cation order*. Journal of Materials Research, 1990. **5**(4): p. 829-834.
40. Tsur, Y., T.D. Dunbar, and C.A. Randall, *Crystal and defect chemistry of rare earth cations in BaTiO<sub>3</sub>*. Journal of Electroceramics, 2001. **7**(1): p. 25-34.

41. Guzhva, M., V. Lemanov, P. Markovin, and W. Kleemann, *Critical concentrations in Ba-doped incipient ferroelectric SrTiO<sub>3</sub>*. *Physics of the Solid State*, 1997. **39**(4): p. 618-624.
42. Griffith, A.A., *The Phenomena of Rupture and Flow in Solids*. Philosophical Transactions of the Royal Society A: Mathematical, Physical and Engineering Sciences, 1921. **221**(582-593): p. 163-198.
43. Frank, F.C. and J.H. van der Merwe, *One-Dimensional Dislocations. II. Misfitting Monolayers and Oriented Overgrowth*. *Proceedings of the Royal Society A: Mathematical, Physical and Engineering Sciences*, 1949. **198**(1053): p. 216-225.
44. Kawasugi, Y., H.M. Yamamoto, M. Hosoda, N. Tajima, T. Fukunaga, K. Tsukagoshi, and R. Kato, *Strain-induced superconductor/insulator transition and field effect in a thin single crystal of molecular conductor*. *Applied Physics Letters*, 2008. **92**(24): p. 243508.
45. Chu, M., Y. Sun, U. Aghoram, and S.E. Thompson, *Strain: A Solution for Higher Carrier Mobility in Nanoscale MOSFETs*. *Annual Review of Materials Research*, 2009. **39**(1): p. 203-229.
46. Trithaveesak, O., J. Schubert, and C. Buchal, *Ferroelectric properties of epitaxial BaTiO<sub>3</sub> thin films and heterostructures on different substrates*. *Journal of Applied Physics*, 2005. **98**(11): p. 114101.
47. Kubicek, M., Z. Cai, W. Ma, B. Yildiz, H. Hutter, and J.r. Fleig, *Tensile Lattice Strain Accelerates Oxygen Surface Exchange and Diffusion in La<sub>1-x</sub>Sr<sub>x</sub>CoO<sub>3-δ</sub> Thin Films*. *ACS nano*, 2013. **7**(4): p. 3276-3286.
48. Petrie, J.R., C. Mitra, H. Jeen, W.S. Choi, T.L. Meyer, F.A. Reboredo, J.W. Freeland, G. Eres, and H.N. Lee, *Strain Control of Oxygen Vacancies in Epitaxial Strontium Cobaltite Films*. *Advanced Functional Materials*, 2016. **26**(10): p. 1564-1570.
49. Schlom, D.G., L.-Q. Chen, C.J. Fennie, V. Gopalan, D.A. Muller, X. Pan, R. Ramesh, and R. Uecker, *Elastic strain engineering of ferroic oxides*. *MRS Bulletin*, 2014. **39**(02): p. 118-130.
50. Sheng, G., Y.L. Li, J.X. Zhang, S. Choudhury, Q.X. Jia, V. Gopalan, D.G. Schlom, Z.K. Liu, and L.Q. Chen, *Phase transitions and domain stabilities in biaxially strained (001) SrTiO<sub>3</sub> epitaxial thin films*. *Journal of Applied Physics*, 2010. **108**(8): p. 084113.
51. Sirohi, J. and I. Chopra, *Fundamental understanding of piezoelectric strain sensors*. *Journal of intelligent material systems and structures*, 2000. **11**(4): p. 246-257.
52. Jaffe, B., *Piezoelectric Ceramics*. 2012: Elsevier Science.
53. Crandles, D., B. Nicholas, C. Dreher, C. Homes, A. McConnell, B. Clayman, W. Gong, and J. Greedan, *Optical properties of highly reduced SrTiO<sub>3-x</sub>*. *Physical Review B*, 1999. **59**(20): p. 12842.
54. Kim, Y., A.S. Disa, T.E. Babakol, X. Fang, and J.D. Brock, *Strain and oxygen vacancy ordering in SrTiO<sub>3</sub>: Diffuse x-ray scattering studies*. *Physical Review B*, 2015. **92**(6).
55. Yang, J.J., M.D. Pickett, X. Li, D.A. Ohlberg, D.R. Stewart, and R.S. Williams, *Memristive switching mechanism for metal/oxide/metal nanodevices*. *Nat Nanotechnol*, 2008. **3**(7): p. 429-33.
56. Joshua Yang, J., F. Miao, M.D. Pickett, D.A. Ohlberg, D.R. Stewart, C.N. Lau, and R.S. Williams, *The mechanism of electroforming of metal oxide memristive switches*. *Nanotechnology*, 2009. **20**(21): p. 215201.
57. Waser, R., R. Dittmann, G. Staikov, and K. Szot, *Redox-Based Resistive Switching Memories - Nanoionic Mechanisms, Prospects, and Challenges*. *Advanced Materials*, 2009. **21**(25-26): p. 2632-2663.
58. Willmott, P. and J. Huber, *Pulsed laser vaporization and deposition*. *Reviews of Modern Physics*, 2000. **72**(1): p. 315.
59. Duk, A., *Relationships Between Strain, Ferro- and Piezoelectric Properties in Functional Oxide Thin Films*. 2013.
60. Vendik, O., S. Zubko, and M. Nikol'skii, *Modeling and calculation of the capacitance of a planar capacitor containing a ferroelectric thin film*. *Technical Physics*, 1999. **44**(4): p. 349-355.
61. Yang, C.S., D.S. Shang, Y.S. Chai, L.Q. Yan, B.G. Shen, and Y. Sun, *Electrochemical-reaction-induced synaptic plasticity in MoO<sub>x</sub>-based solid state electrochemical cells*. *Phys Chem Chem Phys*, 2017. **19**(6): p. 4190-4198.

62. Kim, S., C. Du, P. Sheridan, W. Ma, S. Choi, and W.D. Lu, *Experimental demonstration of a second-order memristor and its ability to biorealistically implement synaptic plasticity*. Nano Lett, 2015. **15**(3): p. 2203-11.
63. Smith, M.B., K. Page, T. Siegrist, P.L. Redmond, E.C. Walter, R. Seshadri, L.E. Brus, and M.L. Steigerwald, *Crystal structure and the paraelectric-to-ferroelectric phase transition of nanoscale BaTiO<sub>3</sub>*. Journal of the American Chemical Society, 2008. **130**(22): p. 6955-6963.
64. Glazer, A. and S. Mabud, *Powder profile refinement of lead zirconate titanate at several temperatures. II. Pure PbTiO<sub>3</sub>*. Acta Crystallographica Section B: Structural Crystallography and Crystal Chemistry, 1978. **34**(4): p. 1065-1070.
65. Shirane, G., R. Newnham, and R. Pepinsky, *Dielectric Properties and Phase Transitions of NaNbO<sub>3</sub> and (Na, K)NbO<sub>3</sub>*. Physical Review, 1954. **96**(3): p. 581.
66. Haeni, J., P. Irvin, W. Chang, R. Uecker, P. Reiche, Y. Li, S. Choudhury, W. Tian, M. Hawley, and B. Craigo, *Room-temperature ferroelectricity in strained SrTiO<sub>3</sub>*. Nature, 2004. **430**(7001): p. 758-761.
67. Wördenweber, R., E. Hollmann, R. Kutzner, and J. Schubert, *Induced ferroelectricity in strained epitaxial SrTiO<sub>3</sub> films on various substrates*. Journal of applied physics, 2007. **102**(4): p. 4119.
68. Wördenweber, R., J. Schubert, T. Ehlig, and E. Hollmann, *Relaxor ferro- and paraelectricity in anisotropically strained SrTiO<sub>3</sub> films*. Journal of applied physics, 2013. **113**(16): p. 164103.
69. Wördenweber, R., J. Schwarzkopf, E. Hollmann, A. Duk, B. Cai, and M. Schmidbauer, *Impact of compressive in-plane strain on the ferroelectric properties of epitaxial NaNbO<sub>3</sub> films on (110) NdGaO<sub>3</sub>*. Applied physics letters, 2013. **103**(13): p. 132908.
70. Cai, B., J. Schwarzkopf, E. Hollmann, M. Schmidbauer, M. Abdel-Hamed, and R. Wördenweber, *Anisotropic ferroelectric properties of anisotropically strained epitaxial NaNbO<sub>3</sub> films*. Journal of applied physics, 2014. **115**(22): p. 224103.
71. Ihlefeld, J.F., C. Folkman, S. Baek, G. Brennecke, M. George, J. Carroll III, and C. Eom, *Effect of domain structure on dielectric nonlinearity in epitaxial BiFeO<sub>3</sub> films*. Applied Physics Letters, 2010. **97**(26): p. 262904.
72. Melville, A., T. Mairoser, A. Schmehl, T. Birol, T. Heeg, B. Holländer, J. Schubert, C. Fennie, and D. Schlom, *Effect of film thickness and biaxial strain on the curie temperature of EuO*. Applied Physics Letters, 2013. **102**(6): p. 062404.
73. Regnery, S., R. Thomas, P. Ehrhart, and R. Waser, *SrTa<sub>2</sub>O<sub>6</sub> thin films for high-K dielectric applications grown by chemical vapor deposition on different substrates*. Journal of applied physics, 2005. **97**(7): p. 073521.
74. Infortuna, A., P. Murali, M. Cantoni, and N. Setter, *Epitaxial growth of (SrBa)Nb<sub>2</sub>O<sub>6</sub> thin films on SrTiO<sub>3</sub> single crystal substrate*. Journal of applied physics, 2006. **100**(10): p. 104110.
75. Das, R.R., P. Bhattacharya, and R.S. Katiyar, *Enhanced ferroelectric properties in laser-ablated SrBi<sub>2</sub>Nb<sub>2</sub>O<sub>9</sub> thin films on platinized silicon substrate*. Applied physics letters, 2002. **81**(9): p. 1672-1674.
76. Bao, D., S.K. Lee, X. Zhu, M. Alexe, and D. Hesse, *Growth, structure, and properties of all-epitaxial ferroelectric (Bi,La)<sub>4</sub>Ti<sub>3</sub>O<sub>12</sub>/Pb(Zr<sub>0.4</sub>Ti<sub>0.6</sub>)O<sub>3</sub>/(Bi, La)<sub>4</sub>Ti<sub>3</sub>O<sub>12</sub> trilayered thin films on SrRuO<sub>3</sub>-covered SrTiO<sub>3</sub> (011) substrates*. Applied Physics Letters, 2005. **86**(8): p. 82906-83100.
77. Wong-Ng, W., Z. Yang, J. Kaduk, L. Cook, S. Diwanji, and C. Lucas, *Interactions of Ba<sub>2</sub>YCu<sub>3</sub>O<sub>6+x</sub> with SrTiO<sub>3</sub> substrate*. Physica C: Superconductivity, 2011. **471**(7): p. 250-257.
78. Liu, R., Y. Cheng, J. Chen, R. Liu, J. Wang, J. Tsai, and M. Hsu, *Crystal and electronic structures of (Ba, Sr)TiO<sub>3</sub>*. Materials Letters, 1998. **37**(4): p. 285-289.
79. Christen, H.M., E.D. Specht, S.S. Silliman, and K.S. Harshavardhan, *Ferroelectric and antiferroelectric coupling in superlattices of paraelectric perovskites at room temperature*. Physical Review B, 2003. **68**(2).
80. Zhang, L., W. Zhong, Y. Wang, and P. Zhang, *The cell volume effect in barium strontium titanate*. Solid state communications, 1997. **104**(5): p. 263-266.

81. Tinte, S., M.G. Stachiotti, S.R. Phillpot, M. Sepliarsky, D. Wolf, and R.L. Migoni, *Ferroelectric properties of  $Ba_xSr_{1-x}TiO_3$  solid solutions obtained by molecular dynamics simulation*. Journal of Physics: Condensed Matter, 2004. **16**(20): p. 3495-3506.
82. Hilton, A. and B. Ricketts, *Dielectric properties of ceramics*. Journal of Physics D: Applied Physics, 1996. **29**(5): p. 1321.
83. Hoffmann, S. and R. Waser, *Curie-Weiss law of  $(Ba_{1-x}Sr_x)TiO_3$  thin films prepared by chemical solution deposition*. Le Journal de Physique IV, 1998. **08**(PR9): p. Pr9-221-Pr9-224.
84. Dul'kin, E., J. Zhai, and M. Roth, *Relaxor-ferroelectric crossover seen via characteristic temperatures of  $Ba_xSr_{1-x}TiO_3$  ferroelectrics detected by acoustic emission*. physica status solidi (b), 2015. **252**(9): p. 2079-2083.
85. Rupprecht, G. and R.O. Bell, *Microwave Losses in Strontium Titanate above the Phase Transition*. Physical Review, 1962. **125**(6): p. 1915-1920.
86. Jackson, W. and W. Reddish, *High Permittivity Crystalline Aggregates*. Nature, 1945. **156**(3972): p. 717-717.
87. Kvasov, A. and A.K. Tagantsev, *Positive effective  $Q_{12}$  electrostrictive coefficient in perovskites*. Journal of Applied Physics, 2012. **112**(9): p. 094106.
88. Kityk, A., W. Schranz, P. Sondergeld, D. Havlik, E. Salje, and J. Scott, *Low-frequency superelasticity and nonlinear elastic behavior of  $SrTiO_3$  crystals*. Physical Review B, 2000. **61**(2): p. 946.
89. Wang, J., F. Meng, X. Ma, M. Xu, and L. Chen, *Lattice, elastic, polarization, and electrostrictive properties of  $BaTiO_3$  from first-principles*. Journal of Applied Physics, 2010. **108**(3): p. 034107.
90. Hollmann, E., J. Schubert, R. Kutzner, and R. Wördenweber, *Stress generated modifications of epitaxial ferroelectric  $SrTiO_3$  films on sapphire*. Journal of applied physics, 2009. **105**(11): p. 114104.
91. Wördenweber, R., T. Grellmann, K. Greben, J. Schubert, R. Kutzner, and E. Hollmann, *Stress Generated Modifications of Structural and Morphologic Properties of Epitaxial  $SrTiO_3$  Films on Sapphire*. Ferroelectrics, 2012. **430**(1): p. 57-64.
92. Van der Merwe, J., *Crystal Interfaces. Part I. Semi - Infinite Crystals*. Journal of Applied Physics, 1963. **34**(1): p. 117-122.
93. Matthews, J. and A. Blakeslee, *Defects in epitaxial multilayers: I. Misfit dislocations*. Journal of Crystal Growth, 1974. **27**: p. 118-125.
94. Matthews, J., D. Jackson, and A. Chambers, *Effect of coherency strain and misfit dislocations on the mode of growth of thin films*. Thin Solid Films, 1975. **26**(1): p. 129-134.
95. Uecker, R., B. Velickov, D. Klimm, R. Bertram, M. Bernhagen, M. Rabe, M. Albrecht, R. Fornari, and D.G. Schlom, *Properties of rare-earth scandate single crystals ( $Re=Nd-Dy$ )*. Journal of Crystal Growth, 2008. **310**(10): p. 2649-2658.
96. Speck, J.S. and W. Pompe, *Domain configurations due to multiple misfit relaxation mechanisms in epitaxial ferroelectric thin films. I. Theory*. Journal of Applied Physics, 1994. **76**(1): p. 466-476.
97. Ban, Z.G. and S.P. Alpay, *Phase diagrams and dielectric response of epitaxial barium strontium titanate films: A theoretical analysis*. Journal of Applied Physics, 2002. **91**(11): p. 9288-9296.
98. Tarsa, E.J., E.A. Hachfeld, F.T. Quinlan, J.S. Speck, and M. Eddy, *Growth - related stress and surface morphology in homoepitaxial  $SrTiO_3$  films*. Applied Physics Letters, 1996. **68**(4): p. 490-492.
99. Yamanaka, T., N. Hirai, and Y. Komatsu, *Structure change of  $Ca_{1-x}Sr_xTiO_3$  perovskite with composition and pressure*. American Mineralogist, 2002. **87**(8-9): p. 1183-1189.
100. Cai, B., *Manipulating the structural and electronic properties of epitaxial  $NaNbO_3$  films via strain and stoichiometry*. 2016, Universität zu Köln.
101. Liang, L., Y. Li, L.-Q. Chen, S.Y. Hu, and G.-H. Lu, *Thermodynamics and ferroelectric properties of  $KNbO_3$* . Journal of Applied Physics, 2009. **106**(10): p. 104118.

102. Hewat, A., *Soft modes and the structure, spontaneous polarization and Curie constants of perovskite ferroelectrics: tetragonal potassium niobate*. Journal of Physics C: Solid State Physics, 1973. **6**(6): p. 1074.
103. Wang, Q.J., C. Pflügl, W.F. Andress, D. Ham, F. Capasso, and M. Yamanishi, *Gigahertz surface acoustic wave generation on ZnO thin films deposited by radio frequency magnetron sputtering on III-V semiconductor substrates*. Journal of Vacuum Science & Technology B: Microelectronics and Nanometer Structures, 2008. **26**(6): p. 1848-1851.
104. Tseng, C.-C., *Frequency response of an interdigital transducer for excitation of surface elastic waves*. IEEE Transactions on Electron Devices, 1968. **15**(8): p. 586-594.
105. Janotti, A., D. Steiauf, and C. Van de Walle, *Strain effects on the electronic structure of SrTiO<sub>3</sub>: Toward high electron mobilities*. Physical Review B, 2011. **84**(20): p. 201304.
106. Al-Hamadany, R., J.P. Goss, P.R. Briddon, S.A. Mojarad, A.G. O'Neill, and M.J. Rayson, *Impact of tensile strain on the oxygen vacancy migration in SrTiO<sub>3</sub>: Density functional theory calculations*. Journal of Applied Physics, 2013. **113**(22): p. 224108.
107. Al-Hamadany, R., J.P. Goss, P.R. Briddon, S.A. Mojarad, M. Al-Hadidi, A.G. O'Neill, and M.J. Rayson, *Oxygen vacancy migration in compressively strained SrTiO<sub>3</sub>*. Journal of Applied Physics, 2013. **113**(2): p. 024108.
108. Liu, Z., D.P. Leusink, X. Wang, W. Lü, K. Gopinadhan, A. Annadi, Y. Zhao, X. Huang, S. Zeng, and Z. Huang, *Metal-Insulator Transition in SrTiO<sub>3-x</sub> Thin Films Induced by Frozen-Out Carriers*. Physical review letters, 2011. **107**(14): p. 146802.
109. Silva, A.R. and G.M. Dalpian, *Oxygen vacancies at the surface of SrTiO<sub>3</sub> thin films*. Journal of Applied Physics, 2014. **115**(3): p. 033710.
110. Choi, S.Y., S.D. Kim, M. Choi, H.S. Lee, J. Ryu, N. Shibata, T. Mizoguchi, E. Tochigi, T. Yamamoto, S.J. Kang, and Y. Ikuhara, *Assessment of Strain-Generated Oxygen Vacancies Using SrTiO<sub>3</sub> Bicrystals*. Nano Lett, 2015. **15**(6): p. 4129-34.
111. Jo, S.H., T. Chang, I. Ebong, B.B. Bhadviya, P. Mazumder, and W. Lu, *Nanoscale memristor device as synapse in neuromorphic systems*. Nano letters, 2010. **10**(4): p. 1297-1301.
112. Yang, Y., P. Gao, S. Gaba, T. Chang, X. Pan, and W. Lu, *Observation of conducting filament growth in nanoscale resistive memories*. Nat Commun, 2012. **3**: p. 732.
113. Driscoll, T., H.-T. Kim, B.-G. Chae, M. Di Ventra, and D. Basov, *Phase-transition driven memristive system*. Applied physics letters, 2009. **95**(4): p. 043503.
114. Chanthbouala, A., V. Garcia, R.O. Cherifi, K. Bouzouane, S. Fusil, X. Moya, S. Xavier, H. Yamada, C. Deranlot, N.D. Mathur, M. Bibes, A. Barthelémy, and J. Grollier, *A ferroelectric memristor*. Nat Mater, 2012. **11**(10): p. 860-4.
115. Kim, D., H. Lu, S. Ryu, C.-W. Bark, C.-B. Eom, E. Tsymbal, and A. Gruverman, *Ferroelectric tunnel memristor*. Nano letters, 2012. **12**(11): p. 5697-5702.
116. Kumar, S., Z. Wang, X. Huang, N. Kumari, N. Davila, J.P. Strachan, D. Vine, A.D. Kilcoyne, Y. Nishi, and R.S. Williams, *Conduction Channel Formation and Dissolution Due to Oxygen Thermophoresis/Diffusion in Hafnium Oxide Memristors*. ACS nano, 2016. **10**(12): p. 11205-11210.
117. Kim, K.M., D.S. Jeong, and C.S. Hwang, *Nanofilamentary resistive switching in binary oxide system; a review on the present status and outlook*. Nanotechnology, 2011. **22**(25): p. 254002.
118. Shuai, Y., S. Zhou, D. Bürger, M. Helm, and H. Schmidt, *Nonvolatile bipolar resistive switching in Au/BiFeO<sub>3</sub>/Pt*. Journal of Applied Physics, 2011. **109**(12): p. 124117.
119. Janousch, M., G.I. Meijer, U. Staub, B. Delley, S.F. Karg, and B.P. Andreasson, *Role of oxygen vacancies in Cr - doped SrTiO<sub>3</sub> for resistance - change memory*. Advanced Materials, 2007. **19**(17): p. 2232-2235.
120. Ohly, C., S. Hoffmann-Eifert, X. Guo, J. Schubert, and R. Waser, *Electrical Conductivity of Epitaxial SrTiO<sub>3</sub> Thin Films as a Function of Oxygen Partial Pressure and Temperature*. Journal of the American Ceramic Society, 2006. **89**(9): p. 2845-2852.

121. Szot, K., W. Speier, G. Bihlmayer, and R. Waser, *Switching the electrical resistance of individual dislocations in single-crystalline SrTiO<sub>3</sub>*. Nat Mater, 2006. **5**(4): p. 312-20.
122. Albrecht, W., J. Moers, and B. Hermanns, *HNF - Helmholtz Nano Facility*. Journal of large-scale research facilities JLSRF, 2017. **3**(A112).
123. Mikheev, E., B.D. Hoskins, D.B. Strukov, and S. Stemmer, *Resistive switching and its suppression in Pt/Nb:SrTiO<sub>3</sub> junctions*. Nat Commun, 2014. **5**: p. 3990.
124. Abe, K. and S. Komatsu, *Epitaxial growth of SrTiO<sub>3</sub> films on Pt electrodes and their electrical properties*. Japanese journal of applied physics, 1992. **31**(9S): p. 2985.
125. Shen, J., H. Lee, R. Valenti, and H.O. Jeschke, *Ab initio study of the two-dimensional metallic state at the surface of SrTiO<sub>3</sub>: Importance of oxygen vacancies*. Physical Review B, 2012. **86**(19).
126. Kubicek, M., R. Schmitt, F. Messerschmitt, and J.L. Rupp, *Uncovering two competing switching mechanisms for epitaxial and ultrathin strontium titanate-based resistive switching bits*. ACS nano, 2015. **9**(11): p. 10737-10748.
127. Starschich, S., S. Menzel, and U. Böttger, *Evidence for oxygen vacancies movement during wake-up in ferroelectric hafnium oxide*. Applied Physics Letters, 2016. **108**(3): p. 032903.
128. Kan, D. and Y. Shimakawa, *Transient behavior in Pt/Nb-doped SrTiO<sub>3</sub> Schottky junctions*. Applied Physics Letters, 2013. **103**(14): p. 142910.
129. Miao, F., J. Joshua Yang, J. Borghetti, G. Medeiros-Ribeiro, and R. Stanley Williams, *Observation of two resistance switching modes in TiO<sub>2</sub> memristive devices electroformed at low current*. Nanotechnology, 2011. **22**(25): p. 254007.
130. Kao, K.C., *Dielectric phenomena in solids*. 2004: Academic press.
131. Ambwani, P., P. Xu, G. Haugstad, J.S. Jeong, R. Deng, K.A. Mkhoyan, B. Jalan, and C. Leighton, *Defects, stoichiometry, and electronic transport in SrTiO<sub>3-δ</sub> epilayers: A high pressure oxygen sputter deposition study*. Journal of Applied Physics, 2016. **120**(5): p. 055704.
132. Sangwan, V.K., D. Jariwala, I.S. Kim, K.S. Chen, T.J. Marks, L.J. Lauhon, and M.C. Hersam, *Gate-tunable memristive phenomena mediated by grain boundaries in single-layer MoS<sub>2</sub>*. Nat Nanotechnol, 2015. **10**(5): p. 403-6.
133. Ngai, K.L. and A.K. Rizos, *Parameterless explanation of the non-arrhenius conductivity in glassy fast ionic conductors*. Physical Review Letters, 1996. **76**(8): p. 1296-1299.
134. Eichel, R.-A., *Structural and dynamic properties of oxygen vacancies in perovskite oxides—analysis of defect chemistry by modern multi-frequency and pulsed EPR techniques*. Physical Chemistry Chemical Physics, 2011. **13**(2): p. 368-384.
135. Karban, P., F. Mach, P. Kús, D. Pánek, and I. Doležal, *Numerical solution of coupled problems using code Agros2D*. Computing, 2013. **95**(1): p. 381-408.
136. Hatta, I., Y. Shiroishi, K.A. Müller, and W. Berlinger, *Critical behavior of the heat capacity in SrTiO<sub>3</sub>*. PHYSICAL REVIEW B, 1977.
137. Breckenfeld, E., R. Wilson, J. Karthik, A.R. Damodaran, D.G. Cahill, and L.W. Martin, *Effect of Growth Induced (Non)Stoichiometry on the Structure, Dielectric Response, and Thermal Conductivity of SrTiO<sub>3</sub> Thin Films*. Chemistry of Materials, 2012. **24**(2): p. 331-337.
138. Waser, R., T. Baiatu, and K.-H. Härdtl, *dc Electrical Degradation of Perovskite-Type Titanates: I, Ceramics*. Journal of the American Ceramic Society, 1990. **73**(6): p. 1645-1653.

# Appendices

## A. Sample list

Table A-1: List of sample discussed in this dissertation.

Sample name	Film and thickness (nm)	Substrate	Reference lattice parameters (Å)			Experimental lattice parameters (Å)			Resulting nominal strain (%)			T <sub>c</sub> (K)	
			a	c		a	b	c	a	b	c	a-axis	b-axis
7150	SrTiO <sub>3</sub>	105 DyScO <sub>3</sub>										299	271
9877	Ba <sub>0.25</sub> Sr <sub>0.75</sub> TiO <sub>3</sub>	70 DyScO <sub>3</sub>											
9878	SrTiO <sub>3</sub>	79 DyScO <sub>3</sub>											
10009	Ba <sub>0.25</sub> Sr <sub>0.75</sub> TiO <sub>3</sub>	47 Si											
10010	Ba <sub>0.25</sub> Sr <sub>0.75</sub> TiO <sub>3</sub>	84 DyScO <sub>3</sub>											
10011	Ba <sub>0.25</sub> Sr <sub>0.75</sub> TiO <sub>3</sub>	76 DyScO <sub>3</sub>											
10769	SrTiO <sub>3</sub>	23 DyScO <sub>3</sub>										290	246
10770	SrTiO <sub>3</sub>	20 DyScO <sub>3</sub>	3.904	3.904	3.904	3.953	3.946	3.880	1.24	1.06	-0.61		
10771	SrTiO <sub>3</sub>	46 DyScO <sub>3</sub>										284	243
10772	SrTiO <sub>3</sub>	40 DyScO <sub>3</sub>	3.904	3.904	3.904	3.952	3.946	3.882	1.22	1.06	-0.56		
10773	SrTiO <sub>3</sub>	60 DyScO <sub>3</sub>	3.904	3.904	3.904	3.952	3.946	3.882	1.22	1.08	-0.57	302	253
10774	SrTiO <sub>3</sub>	92 DyScO <sub>3</sub>										294	271
11150	BaTiO <sub>3</sub>	40 DyScO <sub>3</sub>	3.992	4.036	3.947	3.947	3.950	4.160	-1.12	-1.05	3.07		
11157	Ba <sub>0.125</sub> Sr <sub>0.875</sub> TiO <sub>3</sub>	40 DyScO <sub>3</sub>	3.939	3.939	3.951	3.945	3.939	3.939	0.84	0.61	-0.38	280	234
11158	Ba <sub>0.375</sub> Sr <sub>0.625</sub> TiO <sub>3</sub>	40 DyScO <sub>3</sub>	3.916	3.916	3.949	3.949	3.940	3.901	0.31	0.15	0.00	238	196
11266	BaTiO <sub>3</sub>	40 TbScO <sub>3</sub>	3.992	4.036	3.969	3.969	3.958	4.140	-0.57	-0.85	2.58		
11267	BaTiO <sub>3</sub>	40 GdScO <sub>3</sub>	3.992	4.036	3.975	3.975	3.967	4.140	-0.42	-0.64	2.56		
11268	SrTiO <sub>3</sub>	40 TbScO <sub>3</sub>	3.904	3.904	3.965	3.965	3.963	3.877	1.55	1.50	-0.70	312	298
11269	SrTiO <sub>3</sub>	40 GdScO <sub>3</sub>	3.904	3.904	3.967	3.967	3.972	3.875	1.60	1.73	-0.74	348	344
11686	SrTiO <sub>3</sub>	8.5 DyScO <sub>3</sub>										150	59
11688	SrTiO <sub>3</sub>	5 DyScO <sub>3</sub>											
11689	SrTiO <sub>3</sub>	150 DyScO <sub>3</sub>	3.904	3.904	3.951	3.948	3.906	1.21	1.12	0.05	0.05	141	106
11691	SrTiO <sub>3</sub>	200 DyScO <sub>3</sub>										173	159
11916	SrTiO <sub>3</sub>	90 TbScO <sub>3</sub>	3.904	3.904	3.959	3.962	3.882	1.40	1.49	-0.57	-0.57	325	309
11917	SrTiO <sub>3</sub>	50 TbScO <sub>3</sub>										350	341
11918	SrTiO <sub>3</sub>	10 TbScO <sub>3</sub>	3.904	3.904	3.960	3.960	3.959	3.880	1.43	1.41	-0.61	336	
11919	SrTiO <sub>3</sub>	90 DyScO <sub>3</sub>	3.904	3.904	3.953	3.946	3.884	1.25	1.08	-0.51			
11920	SrTiO <sub>3</sub>	50 DyScO <sub>3</sub>											

Sample name	Film and thickness (nm)	Substrate	Reference lattice parameters (Å)			Experimental lattice parameters (Å)			Resulting nominal strain (%)			T <sub>c</sub> (K)	
			a	c		a	b	c	a	b	c	a-axis	b-axis
11921	SrTiO <sub>3</sub>	10 DyScO <sub>3</sub>	3.904	3.904	3.904	3.954	3.945	3.886	1.27	1.06	-0.47	299	220
11923	SrTiO <sub>3</sub>	225 GdScO <sub>3</sub>											
11924	SrTiO <sub>3</sub>	50 GdScO <sub>3</sub>										390	342
11925	SrTiO <sub>3</sub>	10 GdScO <sub>3</sub>	3.904	3.904	3.904	3.969	3.972	3.874	1.66	1.75	-0.77	398	341
11926	SrTiO <sub>3</sub>	90 SrTiO <sub>3</sub>											
11927	SrTiO <sub>3</sub>	50 SrTiO <sub>3</sub>											
11928	SrTiO <sub>3</sub>	10 SrTiO <sub>3</sub>											
11959	SrTiO <sub>3</sub>	90 Si											
11960	SrTiO <sub>3</sub>	90 GdScO <sub>3</sub>	3.904	3.904	3.904	3.965	3.971	3.877	1.55	1.72	-0.68		
12187	SrTiO <sub>3</sub>	90 DyScO <sub>3</sub>											
12188	SrTiO <sub>3</sub>	60 DyScO <sub>3</sub>											
12189	SrTiO <sub>3</sub>	60 DyScO <sub>3</sub>											
12190	SrTiO <sub>3</sub>	40 DyScO <sub>3</sub>											
11157_Si	B <sub>0.125</sub> Sr <sub>0.875</sub> TiO <sub>3</sub>	40 Si											
11158_Si	B <sub>0.075</sub> Sr <sub>0.925</sub> TiO <sub>3</sub>	40 Si											
41_013_TSO	K <sub>0.7</sub> Na <sub>0.3</sub> NbO <sub>3</sub>	47 TbScO <sub>3</sub>	3.970(3.994)	4.018(3.994)	0.3959	0.3960			-0.28(-0.87)	-1.46(-0.85)		401	416
47_008_DSO	K <sub>0.7</sub> Na <sub>0.3</sub> NbO <sub>3</sub>	27 DyScO <sub>3</sub>	4.018(3.994)	3.970(3.994)	0.3952	0.3946	0.4072		-1.67(-1.05)	-0.61(-1.20)		191	
47_008_GSO	K <sub>0.7</sub> Na <sub>0.3</sub> NbO <sub>3</sub>	27 GdScO <sub>3</sub>	3.970(3.994)	4.018(3.994)	0.3966	0.3970	0.4044		-0.10(-0.70)	-1.21(-0.60)		344	298
47_008_SmSO	K <sub>0.7</sub> Na <sub>0.3</sub> NbO <sub>3</sub>	31 SmScO <sub>3</sub>	3.970(3.994)	4.018(3.994)	0.3983	0.3991	0.4017		0.33(-0.27)	-0.68(-0.07)			
47_008_TSO	K <sub>0.7</sub> Na <sub>0.3</sub> NbO <sub>3</sub>	29 TbScO <sub>3</sub>	3.970(3.994)	4.018(3.994)	0.3959	0.3960	0.4057		-0.28(-0.87)	-1.46(-0.85)		310	326
DSOref2	/	/											
DSOref1	/	/											
GSOref	/	/											
SAW01	/	/											
SAW02	/	/											
SAW03	/	/											
SAW04	/	/											
SAW05	/	/											
STOref-1	/	/											
STOref-2	/	/											
TSOref	/	/											

## B. RSM results

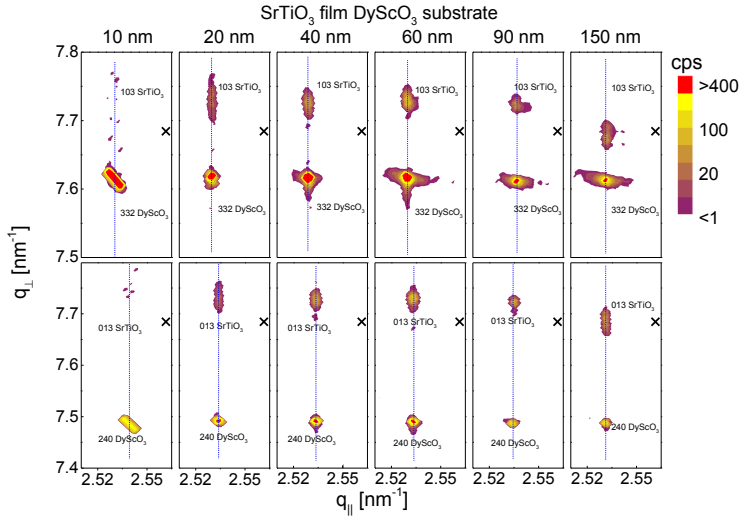


Figure B-1: RSM of the XRD in the vicinity of the (332) (upper row) and the (240) (lower row) Bragg reflections of the substrates for SrTiO<sub>3</sub> film with thickness ranging from 10 nm to 150 nm grown on DyScO<sub>3</sub> substrates. The crosses mark the corresponding position of the reflection of unstrained SrTiO<sub>3</sub>.

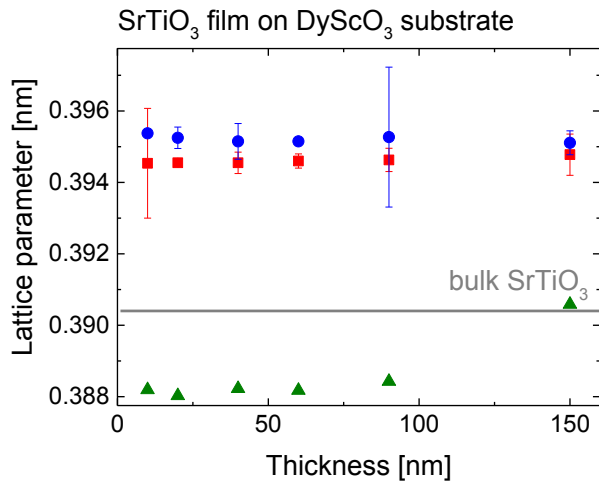


Figure B-2: Lattice parameters as a function of film thickness for SrTiO<sub>3</sub> films grown on DyScO<sub>3</sub> substrates. The blue rounds is the parameters of [001] direction, red squares refer to [110] direction and the green triangles indicate the out-of-plane lattice parameters. The error-bars are calculated from the measurements of the original position and the rotation of 180 degrees of the substrates. The straight line below indicates the unit cell volume of unstrained bulk SrTiO<sub>3</sub>.

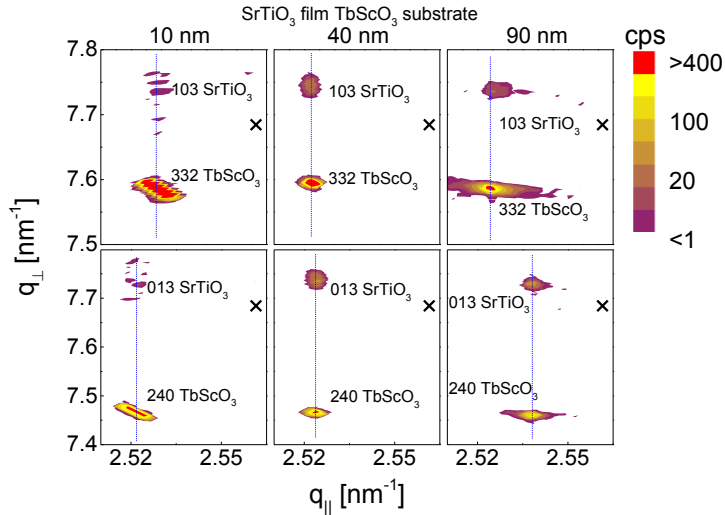


Figure B-3: RSM of the XRD in the vicinity of the (332) (up row) and the (240) (down row) Bragg reflections of the substrates for SrTiO<sub>3</sub> film with thickness ranging from 10 nm to 90 nm grown on TbScO<sub>3</sub> substrates. The crosses mark the corresponding position of the reflection of unstrained SrTiO<sub>3</sub>.

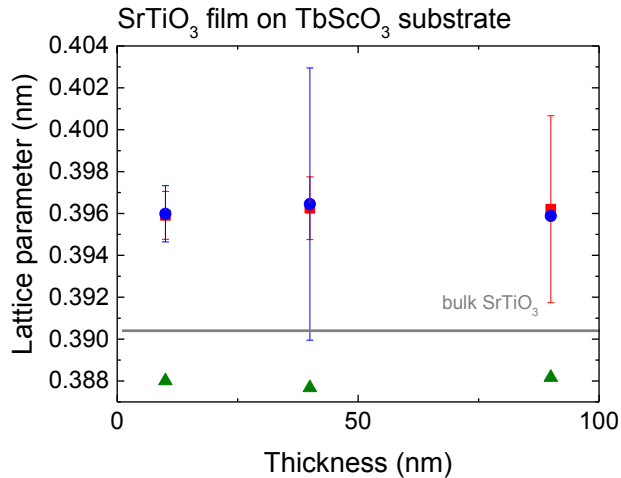


Figure B-4: Lattice parameters as function of film thickness for SrTiO<sub>3</sub> films grown on TbScO<sub>3</sub> substrates. The blue rounds is the parameters of [001] direction, red squares refer to [110] direction and the green triangles indicate the out-of-plane lattice parameters. The error-bars are calculated from the measurements of the original position and the rotation of 180 degrees of the substrates. The straight line below indicates the unit cell volume of unstrained bulk SrTiO<sub>3</sub>.

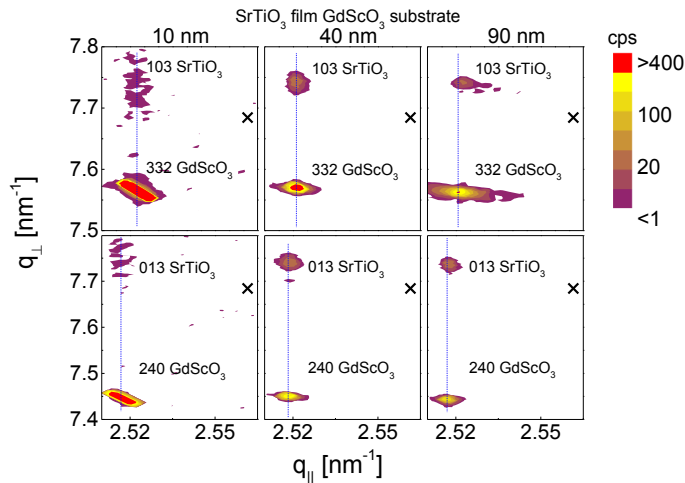


Figure B-5: RSM of the XRD in the vicinity of the (332) (up row) and the (240) (down row) Bragg reflections of the substrates for SrTiO<sub>3</sub> film with thickness ranging from 10 nm to 90 nm grown on GdScO<sub>3</sub> substrates. The crosses mark the corresponding position of the reflection of unstrained SrTiO<sub>3</sub>.

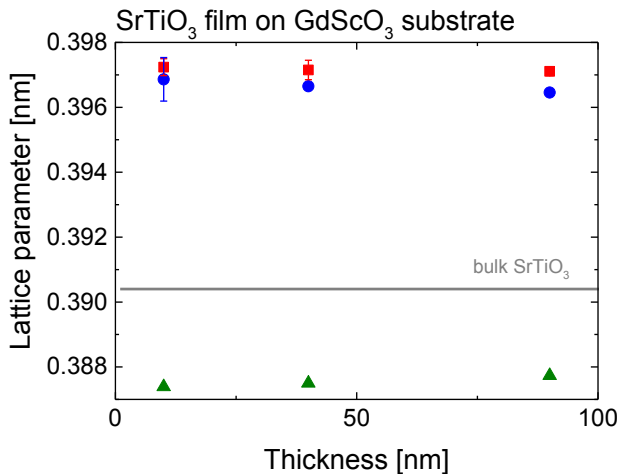


Figure B-6: Lattice parameters as a function of film thickness for SrTiO<sub>3</sub> films grown on GdScO<sub>3</sub> substrates. The blue rounds is the parameters of [001] direction, red squares refer to [110] direction and the green triangles indicate the out-of-plane lattice parameters. The error-bars are calculated from the measurements of the original position and the rotation of 180 degrees of the substrates. The straight line below indicates the unit cell volume of unstrained bulk SrTiO<sub>3</sub>.

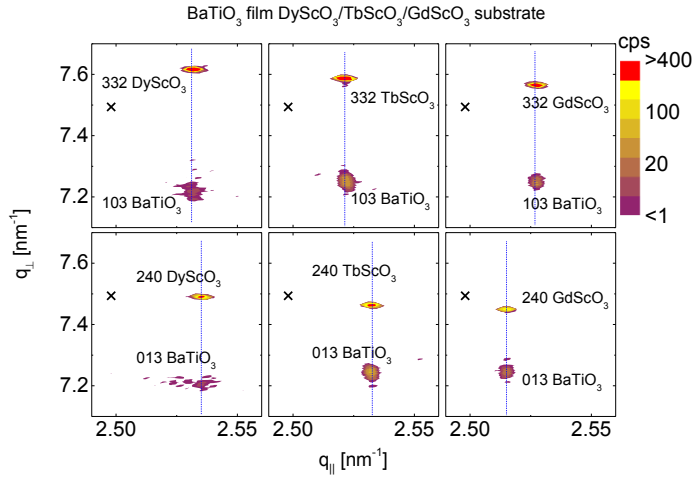


Figure B-7: RSM of the XRD in the vicinity of the (332) (up row) and the (240) (down row) Bragg reflections of the substrates for BaTiO<sub>3</sub> film with thickness of 40 nm grown on DyScO<sub>3</sub>, TbScO<sub>3</sub>, and GdScO<sub>3</sub> substrates. The crosses mark the corresponding position of the reflection of unstrained BaTiO<sub>3</sub>.

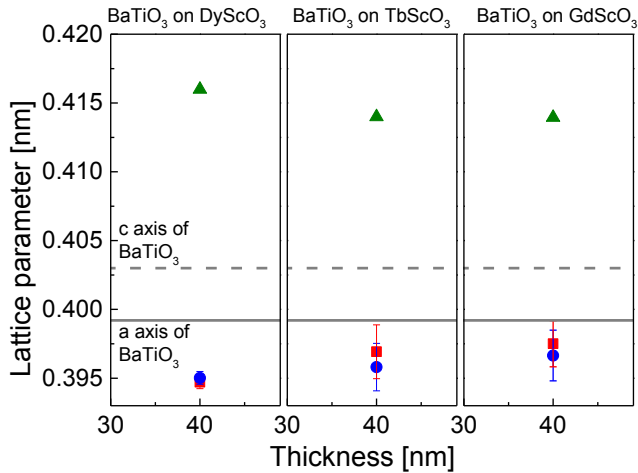


Figure B-8: Lattice parameters of BaTiO<sub>3</sub> films grown on DyScO<sub>3</sub>, TbScO<sub>3</sub>, and GdScO<sub>3</sub> substrates. The blue rounds is the parameters of [001] direction, red squares refer to [110] direction and the green triangles indicate the out-of-plane lattice parameters. The error-bars are calculated from the measurements of the original position and the rotation of 180 degrees of the substrates. The straight line and dashed line indicate the lattice parameters a and c axis of unstrained bulk BaTiO<sub>3</sub>, respectively.

### C. Curie-Weiss temperature

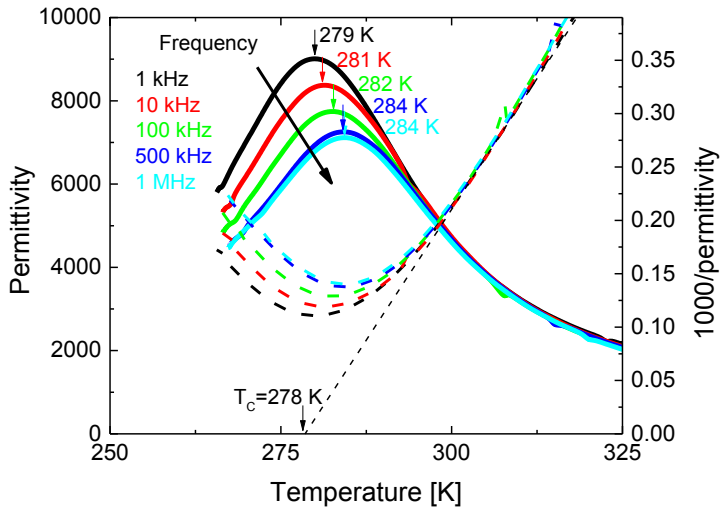


Figure C-1: Temperature dependence of the dielectric permittivity for sample 10772 ( $\text{SrTiO}_3$  40nm/ $\text{DyScO}_3$ , large tensile strain direction) measured at frequency from 1 kHz to 1 MHz. The dashed lines show Curie-Weiss fits (plot of the inverse permittivity (right scale) vs. temperature), and the linear extrapolation provides the Curie-Weiss temperature  $T_C$ . The arrows mark the temperature of maximum permittivity. Which is often used as an indication for the phase-transition temperature.

Figure C-1 shows an example of the difference between the Curie-Weiss temperature  $T_C$  and the temperature of maximum permittivity which is often taken for the phase transition temperature. The Curie-Weiss temperature  $T_C$  is independent of the frequency whereas the temperature of maximum permittivity varies with the frequencies. As a consequence, it is difficult to determine an exact transition temperature from the maximum permittivity, whereas  $T_C$  is useful in this case to characterize the phase transition temperature, because

- i) it is more or less identical for different measurements and,
- ii) the difference between  $T_C$  and the transition temperature is typically less than a few K.

This is the reason why  $T_C$  is used in this work to characterize the phase transition.

## Acknowledgements

This dissertation is a summary of my PhD work in Institute of Complex Systems (ICS-8) in Forschungszentrum Jülich.

First and foremost, I would like to thank my supervisor, Prof. Dr. Roger Wördenweber for the continuous support of my PhD study and related research. He is an example of a good scientist and mentor for me. His office is always open for discussions. He encouraged me to pursue this interesting project and taught me the art of research in how to handle the project processes, how to organize a great team, and how to cooperate with colleagues. He provided me with a highly free research atmosphere, plenty of tremendous wise advice on my work, and the nice daily coffee time with a sense of humor.

I would also like to thank Prof. Dr. Andreas Offenhäusser for creating a convenient research atmosphere in the multicultural environment and supporting my work. I would like to show my gratitude to Dr. Eugen Hollmann for many helpful scientific discussions and teaching me the X-ray diffraction technique, RBS measurements, thin film sputtering, sample preparation processes, and, the most important, an optimistic attitude towards life. My sincere thanks also goes to Rolf Kutzner who is always helpful in solving our technical problems. I am very thankful to Dr. Jürgen Schubert who provided me with all the tensile strained films nicely and timely, so that I can play this strain game. I appreciate Dr. Dirk Mayer who suggested and helped me in the AFM measurement. I acknowledge Dr. Stefan Trelenkamp for the discussions on the designs of electrode pattern and help in the E-beam writing lithography. I am grateful to Elmar Neumann who helped me in analyzing with SEM. I am very thankful to Dr. Gregor Mussler for the XRD analysis.

Special thanks is given to our collaborating group at IKZ, Berlin. I want to show my appreciation to Dr. Jutta Schwarzkopf for providing me with the compressive strained thin films and further helpful discussions. I would also like to show my thanks to Dr. Jan Sellmann for discussions on PLD deposition, Dorothee Braun for discussions on theoretical prediction of phase transition, and Leonard von Helden for the piezoresponse force microscopy test. The regular group meetings allowed us to have fruitful collaborations and to know more about the interesting places in Berlin and Jülich.

I sincerely appreciate my colleagues in my group. We have an outstanding atmosphere during the work and after work. Dr. Thomas Grellmann taught me the “Kölle alaaf” in Carnival. Dr. Kyyrlo Greben was an ideal opponent on my way to the chess master. Dr. Biya Cai shared useful living tips with me. Alexandr Markov taught me some useful Russian words. Junmiao Wang shared the office with me, and Nikolaus Wolf taught me to open a bottle of beer with a lighter.

Most importantly, I want to show my gratitude and love to my family. My parents always stand with me, encouraged me and supported me in my steps in science. I also want to show my love to Hang Zeng, who showed enormous patience for supporting my work, listening to me and encouraging me.

Last but not least, I would like to express my thanks to China Scholarship Council for the financial support during my whole PhD work.

## Statutory declaration in lieu of an oath

I hereby declare in lieu of an oath that I have completed the present Ph. D thesis entitled “*Tailoring the Electronic Properties of Epitaxial Oxide Films via Strain for SAW and Neuromorphic Applications*” independently and without illegitimate assistance from third parties. I have use no other than the specified sources and aids. In case that the thesis is additionally submitted in an electronic format, I declare that the written and electronic versions are fully identical. The thesis has not been submitted to any examination body in this, or similar, form. The thesis is supervised by Prof. Dr. Roger Wördenweber.

## Lebenslauf

Name(Familiename): Dai  
Vorname: Yang  
Geschlecht: männlich  
Geburtsdatum: 23.2.1988  
Geburtsort: Shaanxi, China  
Staatsangehörigkeit: Chinesisch  
Wohnhaft in: Schirmerstr.9 52428 Jülich  
Tel: +49-15902251807  
Email: [daiyang23@gmail.com](mailto:daiyang23@gmail.com)



### Schulausbildung:

09/1993-07/2002 Er Yin Zi Xiao (Grundschule und Mittelschule), Xianyang, Shaanxi, China  
09/2002-07/2005 Shi Yan Zhong Xue (Oberschule), Xianyang, Shaanxi, China

### Hochschulausbildung:

09/2005-07/2009 Bachelor Arbeit an der Xi'an Jiaotong Universität, Xi'an, Shaanxi, China  
09/2009-07/2013 Master Arbeit an der Xi'an Jiaotong Universität, Xi'an, Shaanxi, China  
10/2013-11/2017 Anfertigung der vorliegenden Dissertation bei  
Prof. Dr. Roger Wördenweber am Institute of Complex Systems (ICS-8),  
Forschungszentrum Jülich und Universität zu Köln, Deutschland

### Publikation

**Yang Dai**, Jürgen Schubert, Stefan Trelenkamp, Gregor Mussler, and Roger Wördenweber, Synaptic-like transport properties in biaxial Tensile Strained SrTiO<sub>3</sub> Films, Prepared to Phys. Rev. B. (2017)

**Yang Dai**, Jürgen Schubert, Eugen Hollmann, Gregor Mussler, and Roger Wördenweber, Engineering of the Curie Temperature of Epitaxial  $\text{Sr}_{1-x}\text{Ba}_x\text{TiO}_3$  Films via Strain, *Journal of Applied Physics*, 120, 114101 (2016)

**Yang Dai**, Jürgen Schubert, Eugen Hollmann, and Roger Wördenweber, Electric Field Induced Relaxor Behavior in Anisotropically Strained  $\text{SrTiO}_3$  Films, *Physica B: Condensed Matter*, Volume 485, 15 March 2016, Pages 78-83

Bo Jiao, Yue Yu, **Yang Dai**, Xun Hou, and Zhaoxin Wu, Improvement of light extraction in organic light-emitting diodes using a corrugated microcavity, *Optics Express* Vol. 23, Issue 4, pp. 4055-4064 (2015)

Hua Dong, Zhaoxin Wu, Yucui Gao, Ahmed El-Shafei, Bo Jiao, **Yang Dai**, and Xun Hou, Nanostructure-based counter electrode for dye-sensitized solar cells by assembly of silver nanoparticles, *Organic Electronics* Volume 15, Issue 7, July 2014, Pages 1641-1649

Bo Jiao, Zhaoxin Wu, **Yang Dai**, Dongdong Wang and Xun Hou, Sodium borohydride as an n-type dopant in tris(8-hydroxyquinoline) aluminium thin film, *Journal of Physics D Applied Physics* 42(20):205108 · October 2009

Yu Luo, Li Wang, Yucheng Ding, Huifen Wei, Xiuqing Hao, Dongdong Wang, **Yang Dai**, Jinfeng Shi, Direct fabrication of microlens arrays with high numerical aperture by ink-jetting on nanotextured surface, *Applied Surface Science*, Volume 279, 15 August 2013, Pages 36-40

Zhaoxin Wu, **Yang Dai**, Bo JIAO, Xun Hou, Light-emitting devices and methods for making and using the same, US Patent. US 20160254492 A1. 2016

## **Konferenz**

Poster presentation (First Poster Award), International conference on “Nano confined superconductors and their application” in Garmisch-Partenkirchen, September 3-7, 2016

Oral presentation, International Summerschool on Bioelectronics, Kleinwalsertal, Austria, Juni, 19-26, 2016

Poster presentation, International School of Oxide Electronics 2015, Cargèse, France, Oktober, 12-24, 2015

Poster presentation, Deutsche Physikalische Gesellschaft (DPG) Spring Meeting of the Condensed Matter Division, Berlin, Germany, März, 15-20, 2015

Oral presentation, international Workshop Bioelectronics, Kleinwalsertal, Austria, September, 7-13, 2014



Band / Volume 155

**Graphene Devices for Extracellular Measurements**

D. Kireev (2017), ix, 169 pp

ISBN: 978-3-95806-265-8

Band / Volume 156

**Nanoscale 3D structures towards improved cell-chip coupling on microelectrode arrays**

S. D. Weidlich (2017), II, 154 pp

ISBN: 978-3-95806-278-8

Band / Volume 157

**Interface phenomena in  $\text{La}_{1/3}\text{Sr}_{2/3}\text{FeO}_3$  /  $\text{La}_{2/3}\text{Sr}_{1/3}\text{MnO}_3$  heterostructures and a quest for p-electron magnetism**

M. Waschke (2017), ix, 205 pp

ISBN: 978-3-95806-281-8

Band / Volume 158

**Physics of Life**

Lecture Notes of the 49<sup>th</sup> IFF Spring School 2018

26 February – 09 March 2018, Jülich, Germany

ed. by G. Gompfer, J. Dhont, J. Elgeti, C. Fahlke, D. Fedosov,

S. Förster, P. Lettinga, A. Offenhäusser (2018), ca 1000 pp

ISBN: 978-3-95806-286-3

Band / Volume 159

**Identifizierung von Bindungsdeterminanten von Tat-Vorläuferproteinen an den TatBCRezeptorkomplex während der Tat-abhängigen Proteintranslokation in *Escherichia coli***

A. Ulfing (2018), 186 pp

ISBN: 978-3-95806-290-0

Band / Volume 160

***Corynebacterium glutamicum* – a novel platform for the production of plant polyphenols**

N. Kallscheuer (2018), X, 98 pp

ISBN: 978-3-95806-291-7

Band / Volume 161

**Neurons on 3D polymer nanostructures**

A. Belu (2018), vii, 135 pp

ISBN: 978-3-95806-296-2

Band / Volume 162

**Tailoring and Characterisation of Bioelectronic Interfaces**

A. Markov (2018), 75 pp

ISBN: 978-3-95806-298-6

Band / Volume 163

**Epitaxy of group IV Si-Ge-Sn alloys for advanced heterostructure light emitters**

N. von den Driesch (2018), viii, 149 pp

ISBN: 978-3-95806-300-6

Band / Volume 164

**Impact and Regulatory Control of the CGP3 Prophage in *Corynebacterium glutamicum***

E. Pfeifer (2018), IV, 206 pp

ISBN: 978-3-95806-301-3

Band / Volume 165

**Establishment of Bacterial Microcompartments in the Industrial Production Strain *Corynebacterium glutamicum***

I. Huber (2018), X, 114, XI-XXXIV pp

ISBN: 978-3-95806-302-0

Band / Volume 166

**Current-Induced Magnetization Dynamics in Ferromagnetic Nanowires**

M. I. Khan (2018), vi, 138 pp

ISBN: 978-3-95806-308-2

Band / Volume 167

**Management of Electrophysiological Data & Metadata**

Making complex experiments accessible to yourself and others

L. Zehl (2018), 182 pp

ISBN: 978-3-95806-311-2

Band / Volume 168

**Investigation of GeSn as Novel Group IV Semiconductor for Electronic Applications**

C. Schulte-Braucks (2018), xx, 165, XII pp

ISBN: 978-3-95806-312-9

Band / Volume 169

**Tailoring the Electronic Properties of Epitaxial Oxide Films via Strain for SAW and Neuromorphic Applications**

Y. Dai (2018), VI, 133 pp

ISBN: 978-3-95806-319-8

Weitere **Schriften des Verlags im Forschungszentrum Jülich** unter  
<http://www.zb1.fz-juelich.de/verlagextern1/index.asp>



Schlüsseltechnologien / Key Technologies

Band / Volume 169

ISBN 978-3-95806-319-8